



Founded 1894

SAIMM

JOURNAL OF THE SOUTHERN AFRICAN INSTITUTE OF MINING AND METALLURGY

VOLUME 114 NO. 02 FEBRUARY 2014



All papers featured in this edition were presented at
PRECIOUS METALS 2013
The Precious Metals Development Network
held on 14–16 October 2013



science
& technology

Department:
Science and Technology
REPUBLIC OF SOUTH AFRICA

CSIR
our future through science





For almost a century, Mintek has been at the forefront of minerals and metallurgical research and development...



TODAY THIS CENTRE OF TECHNOLOGICAL EXCELLENCE, with its teams of highly trained and experienced scientists, engineers, researchers, and specialists, continues to build South Africa's resources and capacity by providing advanced technology for the more effective extraction, utilisation and beneficiation of our mineral wealth.



Mintek supplies new technology, process development to pilot-plant scale, and mineralogical and analytical services, to the gold, platinum, base and ferrous metals, uranium and industrial minerals sectors.



Internationally recognised products and services:

- Advanced process control software to optimise operating efficiencies and reduce costs of milling, flotation, smelting, and leach circuits;
- Technologies for the heap bio-assisted leaching of base metals and uranium, and DC arc smelting of ferroalloys and platinum; and
- Auditing, measurement, and optimising of cyanide usage on gold plants.



Our expertise lies in:

- Integrated piloting facilities for process development including comminution; flotation; physical separation; leaching and pressure leaching; smelting; and metal recovery and purification;
- Analytical services;
- Certified reference materials;
- Mineralogical investigations;
- Novel and advanced materials; and
- Mineral economic studies.



Facilities: Our well-equipped facilities include:

- world class laboratory and piloting facilities for process development;
- optimisation, scale-up, and data acquisition in support of feasibility studies in the areas of minerals processing, pyrometallurgy and hydrometallurgy; backed up by
- the latest instrumental techniques for mineral characterisation and chemical analysis.

Your partner in unlocking mineral wealth.

ISO 9001 ■■■■
QUALITY
MANAGEMENT SYSTEM

ISO 17025 ■■■■
TESTING AND CALIBRATION
LABORATORY

ISO 14001 ■■■■
ENVIRONMENTAL
MANAGEMENT SYSTEM

OHSAS 18001 ■■■■
OCCUPATIONAL HEALTH AND
SAFETY MANAGEMENT SYSTEM

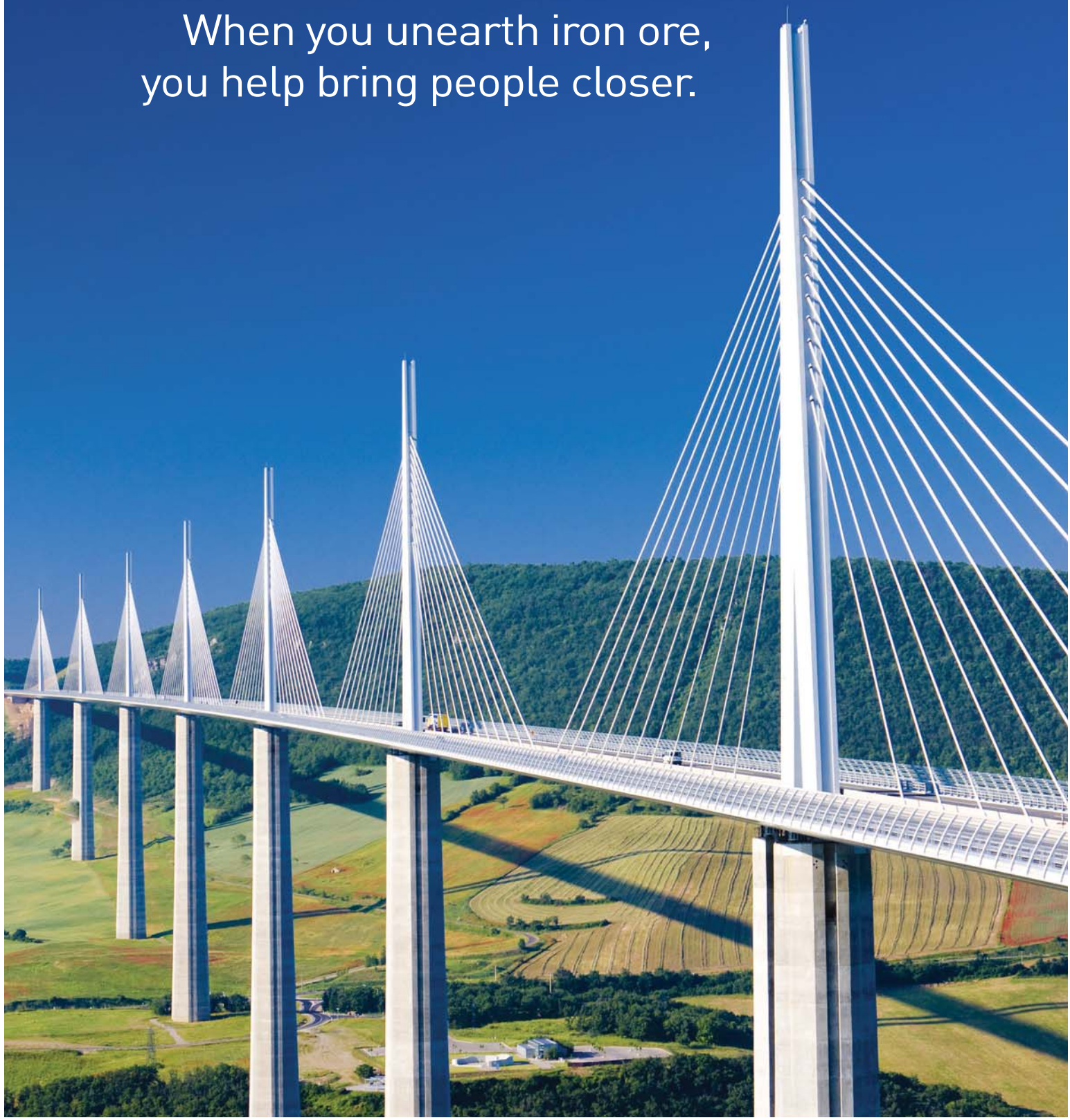
200 Malibongwe Drive, Randburg, South Africa.
Private Bag X3015, Randburg 2125, South Africa.
Phone: +27 (011) 709 4111
Fax: +27 (011) 709 4326
E-mail: info@mintek.co.za
http:// www.mintek.co.za



MINTEK
A global leader in mineral and
metallurgical innovation

Wealth Unearthed

When you unearth iron ore,
you help bring people closer.



This is the kind of wealth AEL Mining Services is proud to help you unearth.
Advancing, constantly evolving and defining the future of explosives in the mining industry.

Tel: +27 11 606 0000
email: company.email@aelms.com
web: www.aelminingservices.com



Mining Services

OFFICE BEARERS AND COUNCIL FOR THE 2013/2014 SESSION

Honorary President

Mark Cutifani
President, Chamber of Mines of South Africa

Honorary Vice-Presidents

Susan Shabangu
Minister of Mineral Resources, South Africa
Rob Davies
Minister of Trade and Industry, South Africa
Derek Hanekom
Minister of Science and Technology, South Africa

President

M. Dworzanowski

President Elect

J.L. Porter

Vice-Presidents

R.T. Jones
C. Musingwini

Immediate Past President

G.L. Smith

Honorary Treasurer

J.L. Porter

Ordinary Members on Council

H. Bartlett	S. Ndlovu
N.G.C. Blackham	G. Njowa
V.G. Duke	S. Rupprecht
M.F. Handley	A.G. Smith
W. Joughin	M.H. Solomon
A.S. Macfarlane	D. Tudor
D.D. Munro	D.J. van Niekerk

Past Presidents Serving on Council

N.A. Barcza	R.P. Mohring
R.D. Beck	J.C. Ngoma
J.A. Cruise	R.G.B. Pickering
J.R. Dixon	S.J. Ramokgopa
F.M.G. Egerton	M.H. Rogers
A.M. Garbers-Craig	J.N. van der Merwe
G.V.R. Landman	W.H. van Niekerk

Branch Chairmen

DRC	S. Maleba
Johannesburg	I. Ashmole
Namibia	G. Ockhuizen
Pretoria	N. Naude
Western Cape	T. Ojumu
Zambia	H. Zimba
Zimbabwe	S.A. Gaihai
Zululand	C. Mienie

Corresponding Members of Council

Australia:	I.J. Corrans, R.J. Dippenaar, A. Croll, C. Workman-Davies
Austria:	H. Wagner
Botswana:	S.D. Williams
Brazil:	F.M.C. da Cruz Vieira
China:	R. Oppermann
United Kingdom:	J.J.L. Cilliers, N.A. Barcza, H. Potgieter
USA:	J-M.M. Rendu, P.C. Pistorius
Zambia:	J.A. van Huissteen

PAST PRESIDENTS

*Deceased

* W. Bettel (1894–1895)	* L.A. Bushell (1954–1955)
* A.F. Crosse (1895–1896)	* H. Britten (1955–1956)
* W.R. Feldtmann (1896–1897)	* Wm. Bleloch (1956–1957)
* C. Butters (1897–1898)	* H. Simon (1957–1958)
* J. Loevy (1898–1899)	* M. Barcza (1958–1959)
* J.R. Williams (1899–1903)	* R.J. Adamson (1959–1960)
* S.H. Pearce (1903–1904)	* W.S. Findlay (1960–1961)
* W.A. Caldecott (1904–1905)	* D.G. Maxwell (1961–1962)
* W. Cullen (1905–1906)	* J. de V. Lambrechts (1962–1963)
* E.H. Johnson (1906–1907)	* J.F. Reid (1963–1964)
* J. Yates (1907–1908)	* D.M. Jamieson (1964–1965)
* R.G. Bevington (1908–1909)	* H.E. Cross (1965–1966)
* A. McA. Johnston (1909–1910)	* D. Gordon Jones (1966–1967)
* J. Moir (1910–1911)	* P. Lambooy (1967–1968)
* C.B. Saner (1911–1912)	* R.C.J. Goode (1968–1969)
* W.R. Dowling (1912–1913)	* J.K.E. Douglas (1969–1970)
* A. Richardson (1913–1914)	* V.C. Robinson (1970–1971)
* G.H. Stanley (1914–1915)	* D.D. Howat (1971–1972)
* J.E. Thomas (1915–1916)	* J.P. Hugo (1972–1973)
* J.A. Wilkinson (1916–1917)	* P.W.J. van Rensburg (1973–1974)
* G. Hildick-Smith (1917–1918)	* R.P. Plewman (1974–1975)
* H.S. Meyer (1918–1919)	* R.E. Robinson (1975–1976)
* J. Gray (1919–1920)	* M.D.G. Salamon (1976–1977)
* J. Chilton (1920–1921)	* P.A. Von Wielligh (1977–1978)
* F. Wartenweiler (1921–1922)	* M.G. Atmore (1978–1979)
* G.A. Watermeyer (1922–1923)	* D.A. Viljoen (1979–1980)
* F.W. Watson (1923–1924)	* P.R. Jochens (1980–1981)
* C.J. Gray (1924–1925)	* G.Y. Nisbet (1981–1982)
* H.A. White (1925–1926)	* A.N. Brown (1982–1983)
* H.R. Adam (1926–1927)	* R.P. King (1983–1984)
* Sir Robert Kotze (1927–1928)	* J.D. Austin (1984–1985)
* J.A. Woodburn (1928–1929)	* H.E. James (1985–1986)
* H. Pirow (1929–1930)	* H. Wagner (1986–1987)
* J. Henderson (1930–1931)	* B.C. Albers (1987–1988)
* A. King (1931–1932)	* C.E. Fivaz (1988–1989)
* V. Nimmo-Dewar (1932–1933)	* O.K.H. Steffen (1989–1990)
* P.N. Lategan (1933–1934)	* H.G. Mosenthal (1990–1991)
* E.C. Ranson (1934–1935)	* R.D. Beck (1991–1992)
* R.A. Flugge-De-Smidt (1935–1936)	* J.P. Hoffman (1992–1993)
* T.K. Prentice (1936–1937)	* H. Scott-Russell (1993–1994)
* R.S.G. Stokes (1937–1938)	* J.A. Cruise (1994–1995)
* P.E. Hall (1938–1939)	* D.A.J. Ross-Watt (1995–1996)
* E.H.A. Joseph (1939–1940)	* N.A. Barcza (1996–1997)
* J.H. Dobson (1940–1941)	* R.P. Mohring (1997–1998)
* Theo Meyer (1941–1942)	* J.R. Dixon (1998–1999)
* John V. Muller (1942–1943)	* M.H. Rogers (1999–2000)
* C. Biccard Jeppe (1943–1944)	* L.A. Cramer (2000–2001)
* P.J. Louis Bok (1944–1945)	* A.A.B. Douglas (2001–2002)
* J.T. McIntyre (1945–1946)	* S.J. Ramokgopa (2002–2003)
* M. Falcon (1946–1947)	* T.R. Stacey (2003–2004)
* A. Clemens (1947–1948)	* F.M.G. Egerton (2004–2005)
* F.G. Hill (1948–1949)	* W.H. van Niekerk (2005–2006)
* O.A.E. Jackson (1949–1950)	* R.P.H. Willis (2006–2007)
* W.E. Gooday (1950–1951)	* R.G.B. Pickering (2007–2008)
* C.J. Irving (1951–1952)	* A.M. Garbers-Craig (2008–2009)
* D.D. Stitt (1952–1953)	* J.C. Ngoma (2009–2010)
* M.C.G. Meyer (1953–1954)	* G.V.R. Landman (2010–2011)
	* J.N. van der Merwe (2011–2012)

Honorary Legal Advisers

Van Hulsteyns Attorneys

Auditors

Messrs R.H. Kitching

Secretaries

The Southern African Institute of Mining and Metallurgy
Fifth Floor, Chamber of Mines Building
5 Hollard Street, Johannesburg 2001
P.O. Box 61127, Marshalltown 2107
Telephone (011) 834-1273/7
Fax (011) 838-5923 or (011) 833-8156
E-mail: journal@saimm.co.za

Editorial Board

R.D. Beck
J. Beukes
P. den Hoed
M. Dworzanowski
M.F. Handley
R.T. Jones
W.C. Joughin
J.A. Luckmann
C. Musingwini
R.E. Robinson
T.R. Stacey

Editorial Consultant

D. Tudor

Typeset and Published by

The Southern African Institute of Mining and Metallurgy
P.O. Box 61127
Marshalltown 2107
Telephone (011) 834-1273/7
Fax (011) 838-5923
E-mail: journal@saimm.co.za

Printed by

Camera Press, Johannesburg

Advertising Representative

Barbara Spence
Avenue Advertising
Telephone (011) 463-7940
E-mail: barbara@avenue.co.za
The Secretariat
The Southern African
Institute of Mining and
Metallurgy
ISSN 2225-6253



THE INSTITUTE, AS A BODY, IS NOT RESPONSIBLE FOR THE STATEMENTS AND OPINIONS ADVANCED IN ANY OF ITS PUBLICATIONS.

Copyright© 1978 by The Southern African Institute of Mining and Metallurgy. All rights reserved. Multiple copying of the contents of this publication or parts thereof without permission is in breach of copyright, but permission is hereby given for the copying of titles and abstracts of papers and names of authors. Permission to copy illustrations and short extracts from the text of individual contributions is usually given upon written application to the Institute, provided that the source (and where appropriate, the copyright) is acknowledged. Apart from any fair dealing for the purposes of review or criticism under *The Copyright Act no. 98, 1978, Section 12*, of the Republic of South Africa, a single copy of an article may be supplied by a library for the purposes of research or private study. No part of this publication may be reproduced, stored in a retrieval system, or transmitted in any form or by any means without the prior permission of the publishers. *Multiple copying of the contents of the publication without permission is always illegal.*

U.S. Copyright Law applicable to users in the U.S.A.

The appearance of the statement of copyright at the bottom of the first page of an article appearing in this journal indicates that the copyright holder consents to the making of copies of the article for personal or internal use. This consent is given on condition that the copier pays the stated fee for each copy of a paper beyond that permitted by Section 107 or 108 of the U.S. Copyright Law. The fee is to be paid through the Copyright Clearance Center, Inc., Operations Center, P.O. Box 765, Schenectady, New York 12301, U.S.A. This consent does not extend to other kinds of copying, such as copying for general distribution, for advertising or promotional purposes, for creating new collective works, or for resale.

JOURNAL OF THE SOUTHERN AFRICAN INSTITUTE OF MINING AND METALLURGY



Volume 114

FEBRUARY 2014

No. 2

Contents

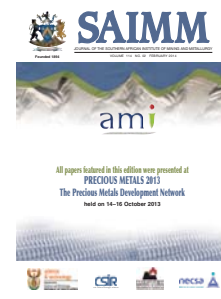
Journal Comment—Precious Metals Conference 2013 by G. Patrick	iv
President's Corner by M. Dworzanowski	v

Precious Metals Conference 2013

Aspects of coloured precious metal intermetallic compounds by E. van der Lingen	137
Structural and electrical characteristics of printed silver and palladium nanoparticle networks by C.B. van den Berg, M. Topic, B. Magunje, D.T. Britton, and M. Harting	145
Investigating the chromium-platinum coated system by N. Hanief, C.I. Lang, and M. Topic	151
Technical and economic aspects of promotion of cobalt-based Fischer-Tropsch catalysts by noble metals—a review by M. de Beer, A. Kunene, D. Nabaho, M. Claeys, and E. van Steen	157
Formation of amorphous Ti-50 at.% Pt by solid-state reactions during mechanical alloying by M.L. Mahlatji, S. Chikosha, H.K. Chikwanda, W.E. Stumpf, and C.W. Siyasiya	167
Ion exchange technology for the efficient recovery of precious metals from waste and low-grade streams by V. Yahorava and M. Kotze	173
Synthesis and crystal structure of tetrakis(1,3-diphenyl-1,3-propanedionato) zirconium(IV) by M. Steyn, H.G. Visser, and A. Roodt	183

International Advisory Board

R. Dimitrakopoulos, *McGill University, Canada*
D. Dreisinger, *University of British Columbia, Canada*
E. Esterhuizen, *NIOSH Research Organization, USA*
H. Mitri, *McGill University, Canada*
M.J. Nicol, *Murdoch University, Australia*
H. Potgieter, *Manchester Metropolitan University, United Kingdom*
E. Topal, *Curtin University, Australia*



Journal Comment

Precious Metals 2013

South Africa has a rich resource in precious metals and other minerals and metals and has certainly used this to its benefit in the creation of great wealth and the provision of a substantial number of jobs for its citizens and those of neighbouring states. The question, though, is can more benefit be derived from this mineral wealth?

In a classic resource-based economy the wealth is limited, firstly by the resource itself and secondly by the rate at which it can be extracted from the ground. South Africa has by no means a resource-based only economy, as shown by the indicators that mining now contributes approximately 9 per cent directly to GDP and about a further 10 per cent indirectly. There is undoubtedly more to the local economy than mining alone; however, South Africa's exports continue to be dominated by unwrought precious metals and other metals and ores, and one always gets a sense of an opportunity missed here. Surely the greater value of minerals and metals lies in their utilization in the manufacturing of the myriad products that have come to dominate our modern lives, i.e. in their downstream value addition or beneficiation.

Possession of all this mineral wealth does not translate directly into a competitive advantage that is immediately capitalized on in downstream industry, and clearly other factors are at play in limiting this growth. What these are is, of course, the subject of much debate, but at least two probable factors are knowledge and skills. Knowledge and intellectual property and the ownership thereof are decidedly important in any transition from our emerging economy to a so-called knowledge-based economy that supports advanced manufacturing.

The Advance Metals Initiative (AMI) is a programme jointly established by the Department of Science and Technology (DST) and the science councils Mintek, the CSIR, and NECSA. Its fundamental goal is R&D-led downstream industrialization of advanced products based on metals important in the local context. The AMI is implemented in four R&D networks, namely precious metals (PMDN) and ferrous and base metals (FMDN), both at Mintek; new metals (NMDN) at NECSA; and light metals (LMDN) at the CSIR. These networks are tasked with innovating and developing technologies and products across the advanced metals value chain in platinum group metals and gold, iron and alloying base metals, zirconium, hafnium, tantalum, and niobium, and aluminium and titanium respectively.

Favoured outcomes of the knowledge gained in R&D in the AMI are commercialization in new industries, local manufacture of products currently imported, and enhancing the competitiveness of existing local industry. Since it is not thought that the onus lies strictly with either government or private industry to achieve greater levels of beneficiation in South Africa, linkages between the AMI and industry are strongly sought. In addition, to support the R&D conducted at the science councils, partnerships with several universities have been established and currently some 80 postgraduate students are sponsored across the four networks. This, it is believed, not only significantly enhances the pool of high-level skilled people needed to achieve the immediate goals of the AMI but also provides the sustained innovation that will be required to sustain any new commercial developments that emanate from the AMI.

This issue of the *SAIMM Journal* brings together a selection of the papers presented at the AMI-sponsored Precious Metals 2013 Conference held in Cape Town during October 2013. The conference, organized around the theme of precious metals in catalysis, chemicals, advanced alloys, and nanotechnology, was in part aimed at showcasing the R&D conducted mainly, but not exclusively, in the PMDN. Each year at the AMI conference students from all the networks can present on their research, and this year the conference included several papers highlighting the work being done in developing new chemistries for the separation of niobium, hafnium, tantalum, and zirconium.

Although one may hope that the R&D reported on is near commercialization, it is an unfortunate reality that the development of new knowledge and intellectual property with commercial potential is a long process, and most of the work presented is necessarily in the very early stages of development. Nonetheless, the papers should give an indication of the high level of research being conducted at various centres around South Africa and the promise held for new materials and processes in precious metals. The path to a knowledge-based economy is arduous, but if you don't start somewhere this goal can never be achieved, and as such the efforts of the AMI are worthy of high commendation.

G. Patrick



Within the Southern African Institute of Mining and Metallurgy, metallurgy is generally taken to refer to extractive metallurgy as this sphere of metallurgy represents those processes used for the beneficiation of run-of-mine ore. However, I believe that many SAIMM members do not realize that the metallurgy part also represents physical metallurgy. Physical metallurgy is the transformation of metal products into alloys and/or semi-fabricated products. The metal products resulting from the application of extractive metallurgy proceed to physical metallurgy processes. These can start with the production of alloys such as stainless steel, brass, and bronze, followed by semi-fabrication processes. Alternatively, the metal products are taken straight to semi-fabrication, usually via melting. Semi-fabrication processes cover the production of plate, rod, wire, pipe, and other intermediate products via casting, drawing, forging, rolling, and annealing.

The applications of physical metallurgy processes in South Africa are far more extensive than people realize. The most obvious is steel production as practised by Arcelor Mittal, Highveld Steel & Vanadium, and Scaw Metals, and stainless steel production by Columbus. The feedstocks to these production centres are all derived locally. On a smaller scale, but still an important contributor to the South African economy, are physical metallurgy processes associated with magnesium, aluminium, titanium, vanadium, chromium, manganese, cobalt, nickel, copper, zinc, cadmium, tin, tungsten, and lead. The application and development of physical metallurgy processes are critical to manufacturing. In particular, the fast-paced development of technology in consumer products such as computers, cellphones, tablets, and televisions is heavily dependent on physical metallurgy. While mining and extractive metallurgy provide the metals required for technology development, it is physical metallurgy that develops the processes that allow the utilization of the metals in technology-based appliances.

A considerable amount of physical metallurgy research is undertaken in South Africa, mainly through the CSIR, Mintek, and the universities. Government is a sponsor of this research through the Department of Science and Technology. The research is not only around developing new materials and new uses for existing materials, but also around improving physical metallurgy processes such as melting, casting, annealing, and forging. South Africa already produces a significant number of speciality metals on which this research is based. Quite soon South Africa will be producing rare earth element products, which are particularly critical for technology development.

Another important aspect of physical metallurgy is corrosion and corrosion protection. This affects our daily lives – rusting steel, peeling paint from metal surfaces, and stained/weathered metals, particularly copper, brass, and silver. Physical metallurgy explains the mechanisms of corrosion and allows the implementation of solutions to corrosion problems. The life of painted surfaces can be extended by the correct surface preparation, which differs for different metals. Steel can be protected by hot dip galvanizing, and aluminium by anodising. A number of different metal surfaces can be protected using different forms of electroplating. The selection of the right materials for different corrosive environments, which is particularly critical in the mining industry and which relates to mining environments as well as metallurgical environments, is also essential.

I hope that this President's Corner will succeed in highlighting the importance of physical metallurgy, and that our physical metallurgist members realize that their Institute does understand and acknowledge their contribution to the mining industry and the economy as a whole

M. Dworzanowski
President, SAIMM

SUSTAINABLE

use of Earth's natural resources

As the global leader in minerals and metals processing technology, Outotec has developed over decades several breakthrough technologies. The company also offers innovative solutions for the chemical industry, industrial water treatment and the utilization of alternative energy sources.

www.outotec.com



Outotec



Aspects of coloured precious metal intermetallic compounds

by E. van der Lingen*

Synopsis

This paper provides a review on coloured gold, platinum, and palladium intermetallic compounds, and discusses the models that were developed to obtain these materials. These compounds have a crystal structure of high symmetry, such as the CaF_2 or CsCl structures, ensuring distinct electron band structures. Various examples of coloured gold, platinum, and palladium intermetallic compounds are provided. More in-depth discussion is provided on the purple gold (AuAl_2) and yellow platinum-aluminium (PtAl_2) compounds with CaF_2 structure, as well as the purplish-pink palladium-indium (PdIn) compound with CsCl structure.

Precious metal intermetallic compounds are used in jewellery and provide a new dimension to design. Some of these compounds have also found use as barrier coatings on turbine blades for jet engines, and more recently, research has been conducted into their potential use as catalysts, electro-catalysts, sensors, capacitors, and for decorative coatings.

Keywords

colour, gold, platinum, palladium, intermetallic compounds, CaF_2 structure, CsCl structure, AuAl_2 , PtAl_2 , PdIn .

Introduction

Intermetallic compounds are compounds consisting of two or more metals in which the numbers of the atoms of the different metals are at, or near, a simple ratio e.g. PtAl_2 . In most cases, intermetallic compounds solidify at a fixed temperature and composition, and have thus a narrow domain of existence. The crystal structure of an intermetallic compound is normally different from those of the individual metals from which it is composed.

Fundamental properties of intermetallic compounds are usually high brittleness with associated low toughness, high hardness, good wear resistance, and good corrosion resistance.

Only about 100 compounds among the 30 000 substances in Pearson's Handbook on Crystallographic Data for Intermetallic Phases (Villars and Calvert, 1991) are coloured. Well-known coloured intermetallic compounds are: golden-yellow Cu_5Sn ; blue NiAl ; yellow CoAl ; yellow CoGa ; blue AuGa_2 ; blue AuIn_2 ; red PdIn ; purple AuAl_2 ; blue-grey NiSi_2 ; and dark blue CoSi_2 .

Colour formation in intermetallic compounds

The formation of colour in metals is based on metallic bonding between different metals. The strong *metallic bonds* consist of positively charged metal atoms in fixed positions, surrounded by delocalized electrons. Colour results from the electrons in the lower energy levels being excited to higher levels. However, colour in metals can also be formed by intermetallic compounds where strong *covalent bonds* replace the metallic bonds.

Some models have been developed indicating the requirements for obtaining coloured intermetallic compounds. Brief descriptions of these models are provided here, and if more in-depth scientific support to these models/concepts is needed, the reader can consult the referenced papers. The three models are:

- (i) Pettifor's structure maps
- (ii) Hume-Rothery electron concentration
- (iii) Valence electron concentration.

Pettifor's structure maps

According to Steinemann (Steinemann, 1990; Steinemann *et al.*, 1997; 2002), coloured intermetallic compounds possess a pseudo-bandgap, which is an energy range with only a few available quantum states, represented by a valley in the density of states curve. These intense localized bands are found approximately 1.5 to 3 eV below the Fermi level. The following three requirements have been identified by Steinemann in order to obtain coloured intermetallic compounds:

* Department of Engineering and Technology Management, Graduate School of Technology Management, University of Pretoria, South Africa.

© The Southern African Institute of Mining and Metallurgy, 2014. ISSN 2225-6253. This paper was first presented at the, Precious Metals 2013 Conference, 14–16 October 2013, Protea Hotel, President, Cape Town, South Africa.

Aspects of coloured precious metal intermetallic compounds

- (1) The crystal structure of the compound is of high symmetry that has strong features of the band structure, i.e. sharp peaks and valleys in the density of states
- (2) Hybrid *d-sp* bonds for strong covalent hybridization
- (3) A late transition element or precious metal shifts the Fermi energy appropriately close to the pseudogap.

Steinemann *et al.* (2002) described how it is possible to establish a relationship between colour and crystal structure in intermetallic compounds by making use of Pettifor's structure maps (Pettifor, 1985; 1986; Pettifor and Podlouchy, 1985). Pettifor's structure maps plot crystal structures of binary compounds A_xB_y of any stoichiometry to a two-dimensional map of some 'coordinates' for elements A and B. Figure 1 shows structure maps for compounds of stoichiometries AB and AB_2 , which could be candidates for coloured intermetallic compounds. The regions marked with dashed lines reveal potential candidates for binary coloured intermetallic compounds. Interestingly, only two crystal structures (Figure 2) dominate these regions, namely bcc-based B2 (Pearson symbol *cP2*) or CsCl-structure for composition AB, and fcc-based C1 (Pearson symbol *cF12*) or CaF_2 -structure for composition AB_2 . This again confirms the three requirements stipulated above that coloured intermetallic compounds need to have a crystal structure of highest symmetry, ensuring a sufficiently simple electronic structure for distinct absorption bands of high intensity. According to this approach, only the following potential coloured binary gold, palladium, and platinum intermetallic compounds can result:

- CsCl structure: PdIn, PdBe, PdMg
- CaF_2 structure: PdAl₂, PtSn₂, PtGa₂, PtAl₂, PtIn₂, AuGa₂, AuAl₂, AuIn₂.

Element B is of Groups 13 and 14 in the Periodic Table, with the exception of PdMg. Furthermore, PtAl (tetragonal structure) also exhibits colour according to Figure 1 (Steinemann *et al.*, 1997). Interestingly, PtGa and PdGa, which have a B1 structure, but do not exhibit colour, are omitted due to a missing pseudogap. PtMg also does not reveal colour as its B20 structure, although cubic, is of lower symmetry. PtGa₂ and PtIn₂ are stable only at temperatures above 153°C and 674°C, respectively (Steinemann, 1990).

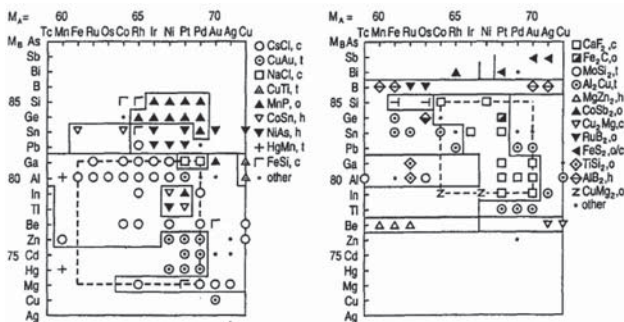


Figure 1—Regions of high-symmetry structure in the AB (a) and AB_2 (b) Pettifor maps. Mendeleev numbers and prototypes (c is cubic, t is tetragonal, o is orthorhombic, h is hexagonal) are shown. Limits for expected coloured intermetallic compounds are shown by the dashed line (Steinemann *et al.*, 1997)

Hume-Rothery electron concentration

An electron-to-atom ratio is stipulated for the Hume-Rothery phases, where the electron concentration (*e/a*) is defined as the sum of the valence electrons per atom of the compound:

$$e/a = 1/100 - \sum a_i v_i$$

where

a_i is the concentration in at.%

v_i is the number of valence electrons of element *i*.

The number of valence electrons for platinum and palladium is 0 according to Ekman's rule, and valence electron numbers are 1, 2, and 3 respectively for Groups 1, 2, and 13 (Al, Ga, In) (Steinemann *et al.*, 2002). Table I gives the specific values for the elements and compounds.

Accordingly, the CsCl structure is stable when *e/a* is approximately 1.1 to 1.7, for example PdIn. Furthermore, the CaF_2 structure is stable if *e/a* is approximately 2.0 to 2.67 as in the case of PtAl₂, PtGa₂, and PtIn₂.

The valence electron concentration

An extension of the Hume-Rothery electron concentration model is the upper limit on the valence electron concentration according to Schlemper and Thomas (1994), which applies to the Zintl phases, for more complex ternary and quaternary compounds. The high number of valence electrons of the precious metals determines the appropriate location of the Fermi level inside the pseudogap, providing absorption bands for creating colour. Eberz (1983) indicated that only intermetallic compounds with valence electron numbers equal to or smaller than about 7 will exhibit colour. Some examples are provided in Table II for various Au, Pd, and Pt compounds (Eberz, 1983).

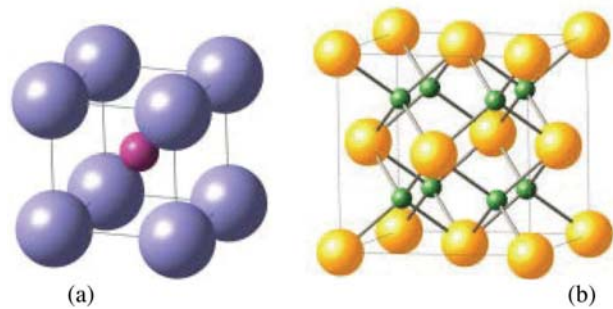


Figure 2—Crystal structures: (a) CsCl structure, and (b) CaF_2 structure

Table I

Number of valence electrons for specific elements and the electron-to-atom ratio of platinum and palladium compounds

Element, i	v
Pd, Pt	0
Al, Ga, In	3
Compound	e/a
PdIn	1.5
PtAl ₂ , PtGa ₂ , PtIn ₂	2

Aspects of coloured precious metal intermetallic compounds

Table II

Some Au-, Pd- and Pt-based ternary intermetallic compounds of the Zintl-type (derivates of the AB₂ structure). The total number of valence electrons, N_{val} is also indicated (Eberz, 1983)

Compound	Colour	N _{val}
Gold compounds		
AuLi ₂ Ga	Green-yellow	6
AuLi ₂ In	Green-yellow	6
AuMgSn	Red-violet	7
AuLi ₂ Pb	Violet	7
AuLi _{0.5} Ga ₂	Blue	7.5
AuMgSb	Grey	8
Palladium compounds		
Pd ₂ LiGe	Brown-yellow	5
PdLi ₂ Al	Rose	5
PdLi ₂ In	Brown-yellow	5
PdLi ₂ Sn	Yellow	6
PdMgSn	Brown-yellow	6
PdLi ₂ Sb	Brass-yellow	7
PdMgSb	Violet	7
Platinum compounds		
PtLi ₂ Al	Bright-yellow	5
PtLi ₂ In	Brass-yellow	5
PtLi ₂ Sn	Yellow	6
PtMgSn	Reddish-brown	6
PtLiAl ₂	Copper-red	7
PtLiGa ₂	Brown-pink	7
PtMgSb	Violet	7

Drews *et al.* (1986) have published interesting results on the optical properties and structures of a number of ternary and quaternary compounds containing platinum or palladium. These compounds are of type Li_xMg_yPS, where P is palladium or platinum and S is tin (Sn) or antimony (Sb). Sometimes x=0, in which case one has a ternary compound. The reflection spectra of all these compounds are similar, indicating colours ranging from yellow to purple, e.g. LiMgPdSn (violet); LiMgPtSn (bright red); LiMgPtSb (violet) etc. By varying the relative amounts of Li and Mg in Li_{2-x}Mg_xPdSn (where x can vary from 0 to 1), Drews *et al.* found that the lattice parameter increased by 1.5% with a colour change from yellow to copper-red and then to red-violet. Figure 3 shows the amount of light reflected as a function of colour (wavelength) for three different intermetallic compounds. The valley in the reflection curve near the green portion of the spectrum leads to stronger reflection at the blue and red ends of the spectrum, resulting in a pink or purple colour. The sharp rise in reflectivity in the blue part of the spectrum is most likely due to increased absorption, resulting from a hybrid resonance between d-electrons of a noble metal and conduction electrons.

Applications

Jewellery

The three main colours of caratage gold alloys, namely yellow, red, and white, are well known. The less-known colours of gold include blue, purple, and black. A review of

coloured gold alloys was published by Cretu and Van der Lingen (1999, 2000). Coloured gold alloys can be produced by three metallurgical routes:

- (i) Alloying with elements such as copper, which results in a more reddish colour; or silver, giving a more white-greenish colour.
- (ii) Coloured oxide layer formation by alloying with an oxidizing element, such as iron, and exposing the alloy to an oxidizing heat treatment.
- (iii) Intermetallic compounds, which are addressed in the present review.

The most popular coloured intermetallic gold compound is purple AuAl₂, which is formed at a composition of 79 wt% Au and 21 wt% Al. This material can be hallmarked as 18 carat gold, which requires at least 75 wt% gold. Due to the brittleness of intermetallic compounds, jewellers have used the colourful compound as inlays, gemstones, and in bi-metal castings (Figure 4). The melting point of AuAl₂ is 1060°C.

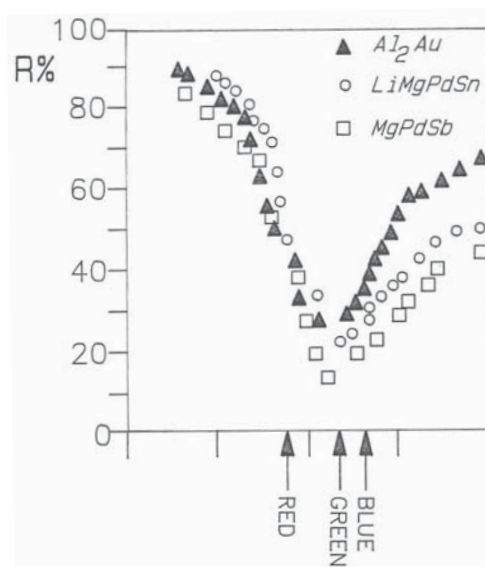


Figure 3—Reflection curves for three intermetallic compounds with the CaF₂ structure (Drews *et al.*, 1986)



Figure 4—Bi-metal castings of micro-alloyed AuGa₂ blue gold (left) and micro-alloyed AuAl₂ purple gold (right) with 95 wt% palladium (Fischer-Bühner *et al.*, 2010)

Aspects of coloured precious metal intermetallic compounds

Two other intermetallic compounds that are known to produce colours in gold alloys, as also revealed by Pettifor's structure maps, are AuIn_2 and AuGa_2 . The gold-indium intermetallic compound AuIn_2 has a clear blue colour and forms at 46 wt%Au, and AuGa_2 at 58.5 wt%Au has a slight bluish hue. The latter compound can be hallmarked as 14 carat gold. The reflectivity falls in the middle of the visible spectrum and rises again towards the violet end, giving distinctive colours in each case (Vishnubhatla and Jan, 1967). Figure 5 shows the reflectivity as a function of the energy of the incident light for AuAl_2 , AuIn_2 , and AuGa_2 (Saeger and Rodies, 1977).

The inherent brittleness of the coloured gold intermetallic compounds can be improved by micro-alloying additions (<2 wt%), such as additional aluminium, palladium, copper, or silver (Wongpreedee, 2006).

Platinum intermetallic compounds

Unlike gold, platinum and palladium have a strong white lustre and act as bleaching agents, making them very difficult to colour by conventional alloying as in the case of gold. Both coloured gold and platinum intermetallic compounds have the CaF_2 structure with alloying elements $X = \text{Al, In, and Ga}$. Klotz (2010) found that interesting colour effects can be achieved by an exchange of gold with platinum while keeping a constant atomic ratio of $(\text{Au,Pt})X_2$. For blue gold, increasing platinum content changes the blue AuIn_2 colour towards apricot PtIn_2 .

Mintek in South Africa has found that two distinct colours, namely orange and pink, result by adding different amounts of copper to the PtAl_2 compound (Hurly, 1991; Hurly and Wedepohl, 1993). The optimum compositions for the colours are shown in Table III.

Figure 6 shows the measured CIELab colour co-ordinates (only positive a^* and b^* values) for the three samples in Table III, as well as unalloyed platinum, gold, silver, and some standard gold alloys. The a^* co-ordinate is a measure of the intensity of the red and green colours of the sample: an increasingly positive a^* indicates more red in the sample, and

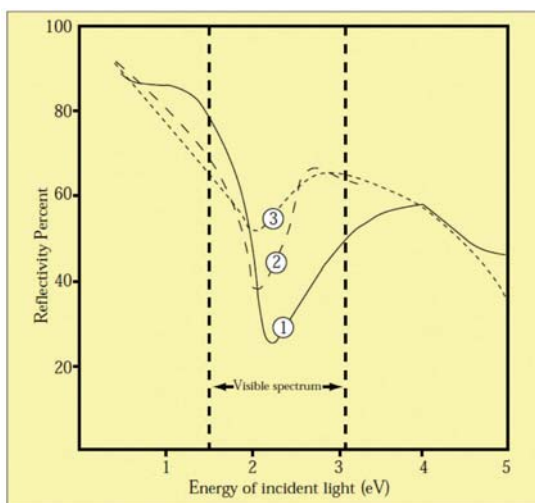


Figure 5—Reflectivity as a function of the energy of the incident light for the intermetallic compounds: (1) AuAl_2 , (2) AuIn_2 , (3) AuGa_2 (Saeger and Rodies, 1977)

increasingly negative a^* values indicate more green.

Similarly, b^* measures yellow and blue: increasingly positive b^* indicates more yellow, and increasingly negative b^* more blue (ASTM-E308-01, 2001).

Figure 7 shows percentage reflectivity as a function of wavelength for PtAl_2 and other samples containing varying amounts of copper. An increase in the copper content results in a change of colour from the characteristic brass-yellow of PtAl_2 through orange to pink. The sample containing 25% copper has a minimum in the green region of the spectrum (about 500 nm), and the higher reflectivities at the blue and particularly red ends of the spectrum combine to give the characteristic pink colour.

Hurly and Wedepohl (1993) found from X-ray diffraction studies of PtAl_2 with various copper additions that all the samples (up to 25 wt% Cu) had the basic fluorite structure

Table III

Composition of three distinct colours for platinum, aluminium and copper compounds

Colour	Platinum, wt%	Aluminium, wt%	Copper, wt%
Yellow	77	23	
Orange	69.3	20.7	10
Pink	61.6	18.4	20

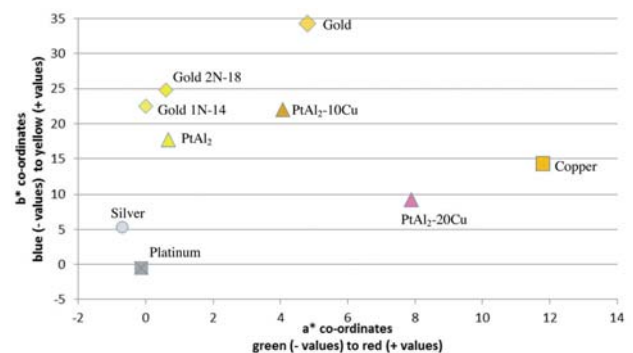


Figure 6—The a^* , b^* co-ordinates of PtAlCu samples, as well as those of pure Pt, Au, Cu and some Au alloys (adapted from Cretu and Van der Lingen, 2000 and Hurly and Wedepohl, 1993)

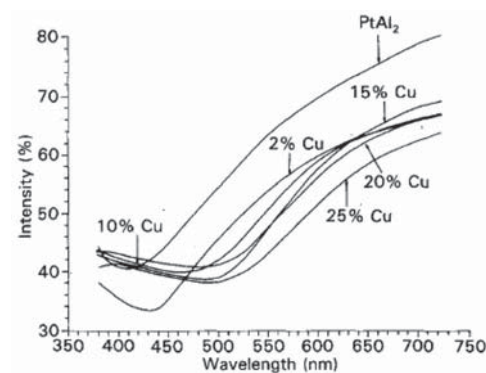


Figure 7—Reflectivity curves for PtAl_2 and PtAl_2 with Cu (Hurly and Wedepohl, 1993)

Aspects of coloured precious metal intermetallic compounds

(CaF₂) of PtAl₂. The lattice parameter increased with copper content as the colour changed. For PtAl₂ with 25wt% copper, the lattice parameter is about 0.8% greater than that of pure PtAl₂.

As with purple gold, coloured platinum intermetallic compounds lend themselves to be treated like gemstones and can be faceted by using standard gem cutting equipment and techniques. Figure 8 shows a jewellery item with faceted pink-platinum compounds, also known as Platigem®.

Palladium intermetallic compounds

According to the binary In-Pd phase diagram (Massalski *et al.*, 1986), five In-Pd intermetallic compounds exist, namely In₃Pd, In₃Pd₂, InPd, InPd₂, and InPd₃. The In-Pd intermetallic compound with composition 50 at.% (48 wt%) palladium and 50 at.% (52 wt%) indium has a purplish-pink colour. Jan and Vishnubhatla (1967) investigated optical properties and Harris *et al.* (1968) investigated structures of palladium-indium alloys. Figure 9 shows results of optical measurements for gold and PdIn. More than 95% of incident light is reflected by gold in the infrared and longer wavelength range of visible light. At energies higher than 1.9 eV, the reflectivity falls off rapidly with diminishing wavelength. The yellow colour of gold results from its strong absorption of light above energies of about 2.3 eV. The metal reveals the complementary colour of the absorbed frequencies. With PdIn, the absorption occurs at lower energies, and the colour of the compound then appears as purplish pink, also confirmed by Nomerovannaya *et al.* (1979). The absorption above about 2.2 eV is associated with a large loss function and interband transitions of hybridized states around the Fermi energy (Cho, 1970). The corresponding CIELab values for PdIn are L* = 70, a* = +12', b* = +6.

Schaffer and Ingersoll (1989) and Steinemann (1990) have investigated the effect of different alloying elements on the PdIn system. A summary of the results is compiled in Table IV.

Coatings

PtAl₂

Platinum-modified aluminide coatings have been used for several decades as diffusion barrier coatings in aircraft and industrial gas turbines (Pomeroy, 2005). These coatings provide improved resistance to both high-temperature oxidation and hot corrosion. Hot corrosion occurs in gas

turbines due to the presence of contaminants such as NaCl, Na₂SO₄, and V₂O₅ in the gases, which form molten deposits that damage the turbine blades (Rajendran, 2012).

The platinum-modified nickel aluminide coatings can exist in two forms depending on how they were formed. Figure 10 shows the two forms, where (a) indicates the two-phase PtAl₂ + (Ni-Pt-Al), and (b) a single-phase (Ni-Pt-Al) coating. Platinum is initially deposited onto the nickel-based superalloy by electroplating, then heat-treated under a protective atmosphere. The heat treatment conditions influence the formation of a single- or two-phase microstructure. Subsequent aluminizing results in the platinum-modified NiAl coating. Figure 11 indicates a depth profile of the platinum-modified NiAl coating in Figure 10 (a).



Figure 8—Photograph of Platigems (faceted pink PtAl₂+Cu) in a jewellery piece (Mintek)

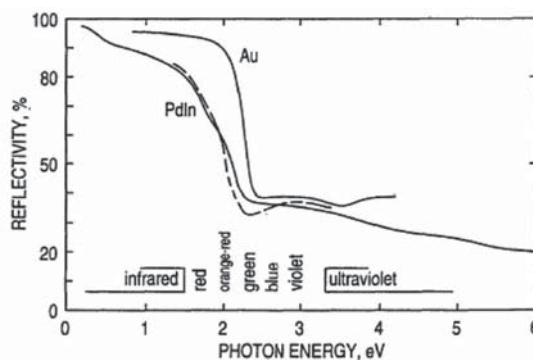


Figure 9—Reflectivity of gold and intermetallic compound PdIn (Jan and Vishnubhatla, 1967)

Table IV	
Anticipated effect of alloying elements on various properties of Pd-In intermetallic compounds	
Elements	Anticipated effect
Au (up to 10 wt%) Mo, Nb, W, Cr (up to 10 wt%) Ta, Ti, Re (up to 6 wt%) Pt, Rh, Ru, Ir (up to 20 wt%) Zn, Sn, Ga, Ge, Al, Si, B (up to 5 wt%) Sc, Y, La and other rare earths (up to 3 wt%)	Increases corrosion resistance, hardness, brittleness Decreases thermal expansion and increase strength Increases strength and grain refining Decreases thermal expansion coefficient, increase in corrosion resistance, grain refining Protects alloy from oxidation during melting and reduce the melting point of the alloy Reduces oxidation of alloys – important for bonding with porcelain (dental alloys)

Aspects of coloured precious metal intermetallic compounds

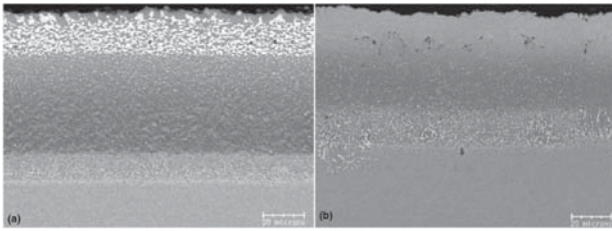


Figure 10—Microstructures of Pt-modified aluminide coatings on nickel-based superalloy. (a) Two-phase PtAl₂ + (Ni-Pt-Al), and (b) single-phase (Ni-Pt-Al) coating (Pomeroy, 2005)

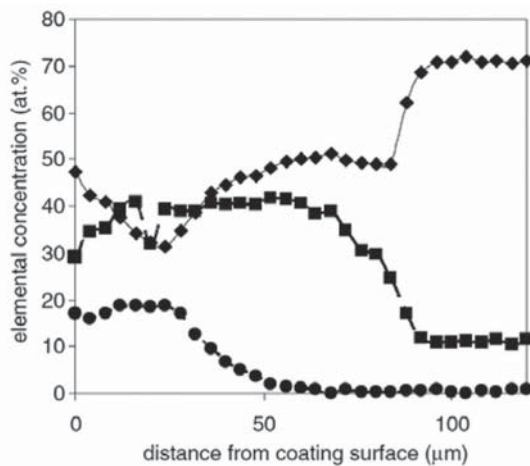


Figure 11—Depth profile for Ni (◆), Pt (●), and Al (■) for the cross-section shown in Figure 10 (a) (Pomeroy, 2005)

The advantages that platinum offers in barrier diffusion coatings can be summarized as follows (Rajendran, 2012 and references therein). Platinum:

- Improves the high-temperature oxidation resistance by delaying transformation of β -NiAl into γ -Ni₃Al in aluminides. The life of the diffusion coating is depleted when all β -NiAl has transformed into γ -Ni₃Al.
- Acts as a catalyst promoting the reaction between aluminium and oxygen.
- Improves the adhesion between the coating and substrate.
- Suppresses deleterious spinel formation.
- Retards the diffusion of certain refractory elements to the coating-Al₂O₃ interface, providing improved isothermal oxidation resistance.

An excellent review by Das (2013) provides information on the importance of the platinum and aluminium contents for the microstructure and oxidation performance of the modified platinum-aluminide bond coatings.

AuAl₂, AuIn₂, and AuGa₂

Supansomboon *et al.* (2008) prepared AuAl₂ coatings by vacuum deposition onto heated substrates. The coloured coatings varied in colour from dark silver to light purple, whereas the transmission colours of these coatings varied from light to dark greenish-brown. The colour observed by the human eye was dependent on the texture of the substrate, and the crystallized microstructure and the coating

thickness affected the transmission colours. The potential use of AuAl₂ as a spectrally selective coating on architectural glass was explored, but the compound was found to be inferior to gold in terms of selective attenuation of the infrared radiation. Furrer *et al.* (2013) found that the light purple colour of AuAl₂ coatings is due to point defects in the film resulting from the deposition method. The intense purple colour can be obtained by heat treating the coating at 350°C.

Supansomboon (2013) produced AuAl₂ and PtAl₂ coatings by a co-sputtering technique, and similar X-ray diffraction patterns were obtained to those of the bulk AuAl₂ and PtAl₂ samples. Figure 12 shows the CIE Lab colour measurements, in both reflectance and transmittance mode, for AuAl₂ and PtAl₂ coatings of different thicknesses. Potential uses include decorative applications and jewellery.

Studies by Keast *et al.* (2013) indicated that PtAl₂ and AuAl₂ coatings have dielectric functions suitable for sustaining localized plasmon resonances, as verified with EELS and reflectivity measurements. The results suggested that the PtAl₂ compound is a better candidate for the development of strong localized surface plasmon resonances compared to AuAl₂.

In a project funded by the European Commission on surface engineering of the colour effect for gold alloys, Klotz (2010) found that the electroplating/annealing process was very successful for producing AuIn₂ layers, whereas surface cladding worked well for both AuGa₂ and AuIn₂, and liquid metal dip-coating for AuGa₂ (Figure 13).

PdIn

Wang *et al.* (1990) developed a thermally stable, low-resistance PdIn ohmic contact to *n*-GaAs. A layer of

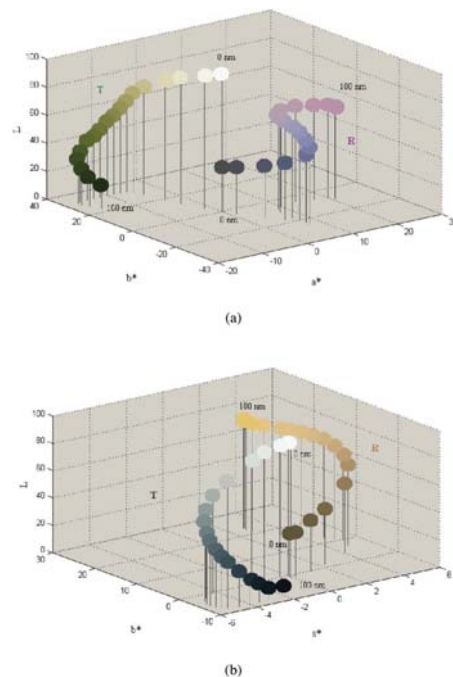


Figure 12—Distribution of chromaticity indices, a* and b* for coloured intermetallic compound films of different thickness, in reflectance and transmittance modes (a) AuAl₂ and (b) PtAl₂ (Supansomboon *et al.*, 2013)

Aspects of coloured precious metal intermetallic compounds



Figure 13—Gold dip-coated with blue AuGa₂ (Klotz, 2010)

In_{0.4}Ga_{0.6}As approximately 5 nm in thickness covered the interface between the single-phase intermetallic PdIn layer and the GaAs substrate. Specific contact resistivities and contact resistances of approximately $1 \times 10^{-6} \Omega \text{ cm}^2$ and 0.14 $\Omega \text{ mm}$ respectively, were obtained.

Catalysis, sensors, and capacitors

Mesoporous, also known as nanoporous, gold and platinum can be prepared by de-alloying AuAl₂ and PtAl₂ in a manner analogous to that used in the preparation of Raney nickel catalysts (Van der Lingen *et al.*, 2001). The aluminium is then dissolved from the AuAl₂ precursor by means of NaOH to produce a highly porous gold structure, (Figure 14). Van der Lingen *et al.* (2003) produced heterogeneous catalysts by incorporating transition metal oxide(s) with the porous gold. Furthermore, promoter elements could also be melted with AuAl₂ to improve catalytic activity. These catalysts were tested for CO oxidation activity.

Patrick *et al.* (2003) studied mesoporous gold catalysts prepared by de-alloying of AuAl₂ for the selective catalytic reduction of NO_x by propene under lean-burn conditions for potential autocatalyst applications. It was found that relatively low additions of platinum group metals (1 at.%) caused shifts to lower temperature regions of activity, with the largest shift obtained for rhodium, most likely due to a strong synergistic interaction between rhodium and gold.

Cortie and Van der Lingen (2003) investigated the potential of mesoporous gold for ultra-capacitors, and preliminary work revealed a perceived capacitance of about 15–28 mF as demonstrated for a sample containing 2 g of gold when connected as a cathode. No storage of energy was observed when the gold was connected as the anode. Further work in this field by Mortari *et al.* (2007) on de-alloyed gold indicated that the electrodes showed near-ideal capacitor behaviour under both cyclic voltammetry and potential-step conditions. They proposed that the mesoporous gold electrodes could offer a convenient way to sensitively and accurately amplify the capacitance signal of an electrochemical sensor.

A significant number of papers have been published recently on nanoporous gold, but the precursor material is 30 wt% gold and 70 wt% silver. A similar de-alloyed structure is obtained for the gold-silver system as for the AuAl₂ system. Potential applications for the nanoporous gold includes: catalysis for oxygen-assisted coupling reactions (Stowers *et al.*, 2013); CO oxidation (Röhe *et al.*, 2013); and electro-

catalysis/fuel cells (Jin *et al.*, 2013); electrochemical immunoassays and sensors (Sun *et al.*, 2013; Zhu *et al.*, 2013; Li *et al.*, 2013).

Rameshan (2012) studied the formation and thermochemical and catalytic properties of Pd-In near-surface intermetallic phases and correlated the findings to those from the PdZn and PdGa systems. The multilayer PdIn intermetallic phase yielded a highly CO₂-selective catalyst for methanol steam reforming, although it was not very active in the temperature range 493–623 K. However, in an In-diluted PdIn intermetallic phase, which correlated with the PdZn system, CO₂ formation was largely suppressed and CO formation enhanced via full methanol dehydrogenation.

Conclusions

Coloured precious metal intermetallic compounds display a range of colours varying from yellow to violet, depending on the specific composition. These coloured compounds have CaF₂ or CsCl crystal structures. The most well-known precious metal intermetallic compounds with CaF₂ structure are purple AuAl₂ and yellow PtAl₂. Copper additions to PtAl₂ can further result in a colour variation from yellow to orange to pink. In jewellery applications these compounds can be used as gemstones, coatings, or inlays in combination with yellow carat gold or white platinum jewellery alloys. The PdIn compound with CsCl crystal structure has a distinct purplish-pink colour, and studies on the effect of different alloying elements on various properties have shown, for example, that additions of up to 20 wt% of other precious metals (Pt, Rh, Ru, Ir) can decrease the thermal expansion coefficient and act as grain refining elements.

Coloured precious metal intermetallic compounds are also used as turbine blade coating material where resistance to high-temperature oxidation and hot corrosion attack is required. The use of coloured precious metal intermetallic compounds as decorative coatings on glass supports is still in the development phase and no commercial products are yet available. De-alloying of precious metal intermetallic compounds can result in mesoporous, also known as nanoporous, materials. These materials have relatively high surface areas, which lend them to further development as catalysts, electro-catalysts, sensors, and capacitors.

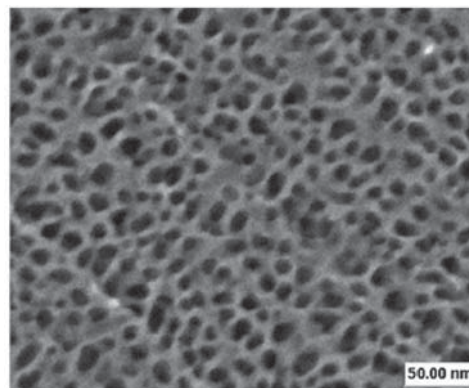


Figure 14—HRSEM image of de-alloyed AuAl₂ surface (Van der Lingen *et al.*, 2003)

Aspects of coloured precious metal intermetallic compounds

Precious metal intermetallic compounds are used in various applications. Although they are inherently brittle, which could restrict their use, this limitation is overcome by using the compounds in powder form, coatings, and inlays with bi-metallic castings.

References

- ASTM: E308-01. 2001. Standard Practice for Computing the Colors of Objects by using the CIE System. *American Society for Testing and Materials* (ASTM).
- CHO, S.J. 1970. Energy bands in β' -PdIn. *Physica Status Solidi*, vol. 41, no. 1. pp. 179–189.
- CORTIE, M.B. and VAN DER LINGEN, E. 2003. Properties and potential applications of meso-porous gold. *Gold 2003. New Industrial Applications for Gold*. World Gold Council and Canadian Institute of Mining, Metallurgy and Petroleum: Vancouver, Canada
- CRETU, C. and VAN DER LINGEN, E. 1999. Coloured gold alloys. *Gold Bulletin*, vol. 34, no. 2. pp. 115–124.
- CRETU, C. and VAN DER LINGEN, E. 2000. Coloured gold alloys. *Gold Technology*, vol. 30. pp. 31–40.
- DAS, D.K. 2013. Microstructure and high temperature oxidation behavior of Pt-modified aluminide bond coats on Ni-base superalloys. *Progress in Materials Science*, vol. 58. pp. 151–182.
- DREWS, J., EBERZ, U., and SCHUSTER, H.-U. 1986. Optische Untersuchungen an farbigen Intermetallischen Phasen. *Journal of the Less-Common Metals*, vol. 116. pp. 271–278.
- EBERZ, U. 1983. *Fabrikation und quaternäre intermetallische Phasen mit Platinmetallen – Zintl – Phasen*. PhD dissertation, University of Cologne.
- FISCHER-BUHNER, J., BASSO, A., and POLIERO, M. 2010. Metallurgy and processing of coloured gold intermetallics – Part II: Investment casting and related alloy design. *Gold Bulletin*, vol. 43, no. 1. pp. 11–20.
- FURRER, A., SEITA, M., and SPOLENAK, R. 2013. The effects of defects in purple AuAl₂ thin films. *Acta Materialia*, vol. 61. pp. 2874–2883.
- HARRIS, I.R., NORMAN, M., and BRYANT, A.W. 1968. A study of some palladium-indium, platinum-indium and platinum-tin alloys. *Journal of the Less-Common Metals*, vol. 16, no. 4. pp. 427–440.
- HURLY, J. and WEDEPOHL, P.T. 1993. Optical properties of coloured platinum intermetallic compounds. *Journal of Materials Science*, vol. 28. pp. 5648–5653.
- HURLY, J. 1991. Intermetallic Compounds. US Patent 5,045,280, Sep. 3 1991
- JAN, J.-P. and VISHNUBHATLA, S.S. 1967. Optical properties of the beta-phase alloys AuZn, GaZn and PdIn. *Canadian Journal of Physics*, vol. 45, no. 8. pp. 2505–2511.
- JIN, W., LIU, J., WANG, Y., YAO, Y., GU, J., and ZOU, Z. 2013. Direct NaBH₄-H₂O₂ fuel cell based on nanoporous gold leaf. *International Journal of Hydrogen Energy*, vol. 38, no. 25. pp. 10992–10997.
- KEAST, V.J., ZWAN, B., SUPANSOMBOON, S., CORTIE, M.B., and PERSSON, P.O.A. 2013. AuAl₂ and PtAl₂ as potential plasmonic materials. *Journal of Alloys and Compounds*, vol. 577. pp. 581–586.
- KLOTZ, E.U. 2010. Metallurgy and processing of coloured gold intermetallics – Part I: Properties and surface processing. *Gold Bulletin*, vol. 43, no. 1. pp. 4–10.
- LI, M., ZHANG, M., GE, S., YAN, M., YU, J., HUANG, J., and LIU, S. 2013. Ultrasensitive electrochemiluminescence immunosensor based on nanoporous gold electrode and Ru-AuNPs/graphene as signal labels. *Sensors and Actuators B: Chemical*, vol. 181. pp. 50–56.
- MASSALSKI, T., MURRAY, J., LAWRENCE, B., and HUGH, B. (eds.) 1986. *Binary Alloy Phase Diagrams*. American Society of Metals, Metals Park, Ohio.
- MORTARI, A., MAAROO, A., MARTIN, D., and CORTIE, M.B. 2007. Mesoporous gold electrodes for sensors based on electrochemical double layer capacitance. *Sensors and Actuators B: Chemical*, vol. 123, no. 1. pp. 262–268.
- NOMEROVANNAYA, L.V., KIRILLOVA, M.M., SAVITSKI, E.M., POLYSKOVA, V.P., GORINA, N.B., and KERONOVSKI, N.L. 1979. The origin of the colour of PdIn intermetallic compound. *Soviet Physics Doklady*, vol. 24, no. 5. pp. 379–382.
- PATRICK, G., VAN DER LINGEN, E., SCHWARZER, H., and ROBERTS, S.J. 2003. Development of gold-sponge catalysts for lean-burn DeNO_x. *Gold 2003. New Industrial Applications for Gold*. World Gold Council and Canadian Institute of Mining, Metallurgy and Petroleum, Vancouver, Canada
- PETTIFOR, D.G. and PODLOUCHY, R. 1985. A microscopic theory of the structural stability of Pd bonded AB compounds. *Physics Review Letters*, vol. 53, no. 2. pp. 1080–1083.
- PETTIFOR, D.G. 1986. New alloys from the quantum engineer. *New Scientist*, vol. 110, no. 1510. pp. 48–53.
- PETTIFOR, D.G. 1985. *Intermetallic Compounds – Principles*, vol. 1. Westbrook, J.H. and Fleischer, R.L. John Wiley & Sons, UK. pp. 419–438.
- POMEROY, M.J. 2005. Coatings for gas turbine materials and long term stability issues. *Materials and Design*, vol. 26. pp. 223–231.
- RAJENDRAN, R. 2012. Gas turbine coatings – an overview. *Engineering Failure Analysis*, vol. 26. pp. 355–369.
- RAMESHAN, C., LORENZ, H., MAYR, L., PENNER, S., ZEMLYANOV, D., ARRIGO, R., HAEVECKER, M., BLUME, R., KNOP-GERICKE, A., SCHLÖGL, R., and KLÖTZER, B. 2012. CO₂-selective methanol steam reforming on In-doped Pd studied by ambient-pressure X-ray photoelectron spectroscopy. *Journal of Catalysis*, vol. 295, no. 2–3. pp. 186–194.
- RÖHE, S., FRANK, K., SCHAEFER, A., WITTSTOCK, A., ZIELASEK, V., ROSENAUER, A., and BÄUMER, M. 2013. CO oxidation on nanoporous gold: A combined TPD and XPS study of active catalysts. *Surface Science*, vol. 609. pp. 106–112.
- SAEGER, K.E. and RODIES, J. 1977. The colour of gold and its alloys. *Gold Bulletin*, vol. 10, no. 1. pp. 10–14.
- SCHAEFER, S. P. and INGERSOLL, C.E. 1989. Gold coloured palladium indium alloys. US Patent 4,804,517. 14 Feb, 1989.
- SCHLEMPER, K. and THOMAS, L.K. 1994. Optical properties and electronic structure of the intermetallic phases NiAl, CoAl, and FeAl. *Physics Review B*, vol. 50, no. 24. pp. 17802–17810.
- STEINEMANN, S.G., ANONGBA, P.N.B., and PODLOUCKY, R. 1997. Color in Pettifor's structure maps: Intermetallic compounds for a new use. *Journal of Phase Equilibria*, vol. 18, no. 6. pp. 655–662.
- STEINEMANN, S.G. 1990. Intermetallic compound, method for producing the compound, and use of the compound. US Patent 4,911,762. Mar. 27 1990
- STEINEMANN, S.G., WOLF, W., and PODLOUCKY, R. 2002. *Colour and Optical Properties*, vol. 3. Intermetallic Compounds – Principles and Practise. Westbrook, J.H. and Fleischer, R.L. (eds.). John Wiley & Sons, UK. pp. 231–244.
- STOWERS, K.J., MADIX, R.J., and FRIEND, C.M. 2013. From model studies on Au(111) to working conditions with unsupported nanoporous gold catalysts: Oxygen-assisted coupling reactions. *Journal of Catalysis*, vol. 308. pp. 131–141.
- SUN, G., LU, J., GE, S., SONG, X., YU, J., YAN, M., and HUANG, J. 2013. Ultrasensitive electrochemical immunoassay for carcinoembryonic antigen based on three-dimensional macroporous gold nanoparticles/graphene composite platform and multienzyme functionalized nanoporous silver label. *Analytica Chimica Acta*, vol. 775. pp. 85–92.
- SUPANSOMBOON, S., MAAROO, A., and CORTIE, M.B. 2008. Purple Glory: The optical properties and technology of AuAl₂ coatings. *Gold Bulletin*, vol. 41, no. 4. pp. 296–304.
- SUPANSOMBOON, S., DOWD, A., VAN DER LINGEN, E., and CORTIE, M.B. 2013. Coatings of coloured intermetallic compound for decorative and technological applications. *Materials Innovation in Surface Engineering (MISE) 2013 Conference*, Adelaide, Australia, 19–21 November 2013.
- VAN DER LINGEN, E., CORTIE, M.C., and GLANER, L. 2001. Catalyst and method of producing a catalyst. SA Patent Application no. 2001/5816.
- Van Der Lingen, E., Cortie, M.B., Schwarzer, H., Roberts, S.J., Patrick, G., and Compton, D. 2003. Gold catalysts prepared via intermetallic precursor. *Gold 2003. New Industrial Applications for Gold*. World Gold Council and Canadian Institute of Mining, Metallurgy and Petroleum, Vancouver, Canada
- VILLARS, P. and CALVERT, L.D. 1991. *Pearson's Handbook of Crystallographic Data for Intermetallic Phases*. ASM International, Materials Park, Ohio.
- VISHNUBHATLA, S.S. and JAN, J.P. 1967. Optical properties of the intermetallic compounds AuAl₂, AuGa₂ and AuIn₂. *Philosophical Magazine*, vol. 16, no. 39. pp. 45–50.
- WANG, L. C., WANG, X. Z., LAU, S. S., SANDS, T., CHAN, W. K., and KUECH, T. F. 1990. Stable and shallow PdIn ohmic contacts to n-GaAs. *Applied Physics Letters*, vol. 56, no. 21. pp. 2129–2131.
- WONGPREEDEE, K. 2006. Purple gold: past, present, and future to ductile intermetallics. *Gold 2006*, University of Limerick, Ireland. World Gold Council.
- ZHU, X.-T., ZHANG, L.-J., TAO, H., and DI, J.-W. 2013. synthesis of nanoporous gold electrode and its application in electrochemical sensor. *Chinese Journal of Analytical Chemistry*, vol. 41, no. 5. pp. 693–697. ◆

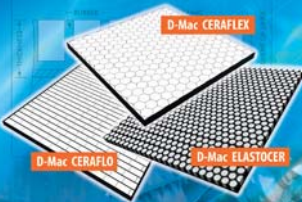
Currently
Servicing
More than
68 Countries
and growing



Tega offers value added consultancy services and solutions
in Mineral Beneficiation, Bulk Solids handling, Wear and
Abrasion customised to suit specific applications.

TOTAL : Solution™

With focus on core engineering applications in the Mining and Mineral
Processing Industry, Steel plants, Power, Port and Cement Industries.

 <p>Composite Steel Cladded Mill Liner Outperforming Steel</p> <p>More cost efficient Lining solution for AG/SAG/Ball Mills</p>	 <p>TEGA METLAST™ Hybrid Mill Lining System For Primary Grinding & AG/SAG Mills</p> <p>TEGA METLAST Hybrid Mill Lining System</p>	 <p>Hydrocyclone Next Generation Hydrocyclone 15" & 16" Hydrocyclone Long Cone Hydrocyclone Separate-Classify & Recover</p> <p>High Capacity cyclone for mill grinding circuit</p> <p>Stub Cyclone Isolate unwanted Renowned for better separation & High Capacity</p>	 <p>D-Mac Liner Hard with a Soft Touch</p> <p>D-Mac CERAFLEX D-Mac CERAFLO D-Mac ELASTOCEER</p> <p>Resistant to Impact and Wear year after year</p>
 <p>Screen Panels Screening - Biggest to the Smallest</p> <p>Dewatering Panel Flip Flo Panel Anti-dogging Panel Cross Tension Panel Panel Cord</p> <p>Widest range panels to screen run of mine to deliverables</p>	 <p>Trommel State-of-the-Art-Trommel</p> <p>Trommel with Polyurethane Decks Trommel with Rubber Decks</p> <p>Dynamically Balanced with FEA</p>	 <p>Spill-Ex Kill Spill through Seals</p> <p>Skirt Board Sealing System Universal Support System</p> <p>Leaders in technology for Belt Spillage Control & Improved Belt Life</p>	 <p>Slider Bed Fix It Forget It</p> <p>Diverse options with Superior Design and Better Results</p>

Tega Industries (South Africa) Pty Ltd

P.O Box 17260, Benoni West, 1503, South Africa,
Phone: (011) 421 - 9916/ 7, 421 - 6714, 421 - 6761,
Fax: (011) 845 1472,
Email: info@tegaindustries.co.za,
www.tegaindustries.com



WE'VE DUG DEEP TO GUARANTEE QUALITY THAT LASTS

For expert results, choose the highest quality hand tools with a lifetime guarantee. From spanners and wrenches to heavy duty toolsets, Gedore products are hot forged and precision crafted for absolute toughness – minimising injury and increasing productivity.



TOOLS FOR LIFE | MINING

Gedore manufactures and distributes hand tools suited to a variety of industries throughout the African continent. We offer a lifetime guarantee and dedicated after sales service for all of our products.



CALL: 0861-GEDORE FAX: 011 608 2953

EMAIL: sales@gedore.co.za WEB: www.gedore.co.za

Visit our website for a FREE copy of
our catalogue | www.gedore.co.za

Realising possibilities...



...from mine to market.



Resource
Evaluation



Mine
Planning



Mining & Mine
Development



Materials
Handling



Environment
& Approvals



Mineral
Processing



Tailings & Waste
Management



Smelting
& Refining



Transport
to Market



Non-Process
Infrastructure

WorleyParsons adds value through our full scope of services from pit to port including studies, mine planning, impact assessments, permitting and approvals, project management, construction management and global procurement.

43 countries :: **165** offices :: **38,700** people



WorleyParsons

resources & energy

www.worleyparsons.com



Structural and electrical characteristics of printed silver and palladium nanoparticle networks

by C.B. van den Berg*, M. Topic†, B. Magunje*, D.T. Britton*, and M. Harting*

Synopsis

In this study, silver and palladium nanoparticulate inks with different metal-binder ratios were screen-printed onto a paper substrate. The printed layers comprised the metal nanoparticles and an ethyl cellulose binder. The layers are not typical metal composites due to the low concentration of binder and high porosity. The electrical sheet resistivity of each particle concentration was measured, and the data fitted using the scaling law of percolation theory and the general effective media (GEM) equation. The percolation parameters, i.e. the percolation threshold and the critical exponent, for each system were determined from the fits and compared. The percolation threshold for the palladium layer (39.8 wt%) was lower than that found for the silver layer (44.9 wt%). The critical exponents determined for the palladium and silver layers were both lower than the universal value for three-dimensional percolation systems. Microscopy observations indicate that the difference in the percolation threshold for the two layers can be attributed to variations in their microstructure.

Keywords

printed electronics, nanotechnology, nanoparticulate inks, silver, palladium.

Introduction

Printed electronics technology has attracted interest over the last few years as an alternative to conventional methods for the fabrication of electronic devices. Printing techniques such as screen and inkjet printing and gravure printing have been used for fabricating electronic devices. These techniques are advantageous because they are relatively simple, promise low production costs, and can be adapted for large scale production. Another advantage is the wide variety of materials, such as paper, plastics, and ceramics, that can be used as substrates (Britton and Härting, 2006; Faddoul *et al.*, 2012). One of the major challenges is to formulate suitable inks for the different printing techniques. Functional electronics inks consist of nanoparticles (NP) dispersed in a liquid medium. Printing the inks involves the selective deposition of the functional materials onto a substrate followed by a curing stage which may involve a number of processing steps (Britton and Härting, 2006; Shim *et al.*, 2008). For this reason metallic NP

are of particular interest due to their forming conductive tracks. Conductivity through the printed layer depends on how densely the NP are packed in the printed layer after curing (Shim *et al.*, 2008). The final microstructure of the layer is also affected by the solvent and substrate used (Suvakov and Tadic, 2010). The basic requirement is therefore that the concentration of the NP must be above the percolation threshold for charge transport (Suvakov and Tadic, 2010). Conductivity through the material occurs through tunnelling or hopping of carriers and is influenced by factors such as the size and shape of the NP, composition, as well as the interparticle separation of the metal NP in the layer (Zabet-Khosousi and Dhirani, 2008; Sichel and Gittleman, 1982). In this study, silver (Ag) and palladium (Pd) nanoparticulate inks were produced with different metal-binder concentrations and deposited onto a substrate using screen printing. Percolation theory was used to determine the percolation threshold p_c and the critical exponent of the layers. The nanoparticle shape and packing structure in the printed layers were studied using scanning electron microscopy (SEM). Observations made about the microstructure of the Ag and Pd layers are related to the percolation parameters obtained from the fits.

Percolation theory

Many properties of composites and colloid systems (i.e. electrical, mechanical, thermal, and optical) are determined by the distribution of the disperse phase in a dispersion medium (Vysotsky and Roldughin, 1999). Percolation

* NanoSciences Innovation Centre, Department of Physics, University of Cape Town, Rondebosch, Cape Town, South Africa.

† Materials Research Department, Somerset West.

© The Southern African Institute of Mining and Metallurgy, 2014. ISSN 2225-6253. This paper was first presented at the, Precious Metals 2013 Conference, 14–16 October 2013, Protea Hotel, President, Cape Town, South Africa.

Structural and electrical characteristics of printed silver and palladium nanoparticle networks

theory has been used to understand changes in physical properties when transitioning from a disconnected to a connected structure in disordered systems (Nan, Shen, and Ma, 2010; Sahimi, 1994)

These physical properties include electrical resistivity and thermal conductivity of diphasic materials (McLachlan, 1990). Classical percolation theory deals with a lattice of 1, 2, 3, n -dimension that can be made up of a site or a bond which is randomly assigned with an occupation probability p (vacant, $1-p$) (McLachlan, Blaszkiewicz, and Newnham, 1990; Leuenberger, 1999). In bond percolation, the cluster size depends on the number of bonds that connect neighbouring particles. In site percolation, cluster formation is a function of the occupation probability of the lattice chosen (Leuenberger, 1999). Lattice percolation is dependent only on the dimensionality and not on the properties of the lattice. Since most materials are heterogeneous (i.e. more than one phase), a continuum percolation will occur (Nan, Shen, and Ma, 2010). In this model the occupation probability p is replaced with a volume fraction of objects with a particular shape (Kirkpatrick, 1973). If one considers a system comprising two different particles with conductivities σ_1 and σ_2 respectively, such that $\sigma_2 \ll \sigma_1$, at very low concentrations of the high conducting particles, the lattice is insulating. Small particle agglomerates begin to form as the concentration of the more conducting particles is increased. As the concentration of the conducting particles is further increased, single conducting clusters begin to form. At a critical concentration of the conducting particles p_c , known as the percolation threshold, conducting links are formed between single clusters, resulting in the formation of an infinite conducting cluster that spans the entire lattice. Therefore the conductivity of the system becomes finite. Above p_c , the infinite cluster will incorporate additional small single clusters resulting in the increase in conductivity of the system (McLachlan, Blaszkiewicz, M., and Newnham, 1990; Leuenberger, 1999; Roldughin and Vysotskii, 2000) that can be described by the fundamental power law of percolation theory:

$$\sigma = \sigma_0(p - p_c)^t \quad [1]$$

Here σ_0 is the proportionality constant, p the volume fraction, and t the critical exponent. The power law holds only for values of p above p_c (Kirkpatrick, 1973). The critical exponent t is said to be universal for 3D percolation systems, and dependent only on the spatial dimensions of the system. p_c is affected by geometric parameters i.e. particle shape, polydispersity, and orientation (Roldughin and Vysotskii,

2000).

The problem in percolation theory is it assumes that a binary system below p_c behaves as a perfect insulator ($\sigma_i = 0$). Above p_c the conductivity of the system becomes infinite ($\sigma_m = \infty$) (McLachlan, 1990). To overcome this problem a general effective media (GEM) equation [2] has been proposed that takes into account the finite values for σ_i and σ_m above and below p_c (McLachlan, Blaszkiewicz, M., and Newnham, 1990):

$$\frac{(1-p)(\rho_m^{1/t} - \rho_i^{1/t})}{(\rho_m^{1/t} - A\rho_i^{1/t})} + \frac{p(\rho_m^{1/t} - \rho_s^{1/t})}{(\rho_m^{1/t} - A\rho_s^{1/t})} = 0, \quad A = \frac{1-p_c}{p_c} \quad [2]$$

Here t is the critical exponent, p is the volume fraction of the conducting phase, p_c is the critical volume fraction, ρ_m is the resistivity of the system, and ρ_i and ρ_s are the resistivities of the phases with low and high conductivity respectively. The GEM equation is based on effective medium and percolation theories. The advantage of the GEM equation is that it has the same parameters (p_c and t) that are used in percolation theory (McLachlan, Blaszkiewicz, and Newnham, 1990; McLachlan, 1990).

Experimental procedure

Sample preparation

The palladium (Pd) NP were supplied by MK_{NANO} and the silver (Ag) NP containing PVP dispersant was supplied by Sigma-Aldrich, Steinheim, Germany. Inks were prepared using ethyl cellulose (ETHOCELTM, Dow Chemical Company) as binder and Butyl CELLOSOLVETM acetate (Dow) as the solvent. Nanoparticulate inks were prepared with different metal-binder ratios as shown in Table I. The nanoparticulate inks were printed using an ATMA AT-60PD semi-automatic flatbed screen printer (Suvakov and Tadic, 2010). Screens made from monofilament polyester fibre with a mesh count of 150 lines per centimetre (supplied by Register Screen (Pty) Ltd) were used for printing. The samples size was 1x1 cm with a thickness of approximately 15–20 μm . The thickness of the layers was determined using a Veeco NT9100 optical profiler operating in the vertical step interferometry (VSI) mode. Plain white 80 g/m² density paper, with no pre-treatment, was used as the substrate. The prints were allowed to cure for at least 48 hours under ambient conditions.

Morphological and electrical characterization

The shape, crystallinity, and size of the NP were observed

Table I

Composition of the nanoparticulate inks. p = weight fraction of the NP

	Component	Composition
Nanopowder:	Palladium Silver	$p = 0.4, 0.5, 0.6, 0.7$ $p = 0.4, 0.45, 0.5, 0.55, 0.6, 0.7$
Binder solution:	Butyl CELLOSOLVE TM ETHOCEL TM	0.93 0.07

* 1-p = weight fraction of the binder solution.

Structural and electrical characteristics of printed silver and palladium nanoparticle networks

with a JEOL JEM-2100 transmission electron microscope. The microstructure of the printed layer was investigated by SEM using a FEI Helios Nanolab 650 FIB-SEM operating in the single electron mode. Only the SEM feature was used for imaging the surface of the layers. The electrical properties of the printed metallic layers were measured using the LakeShore 7500 Series Hall Effect Measurement System. The sample was mounted onto the sample card and the probes placed at each corner. The quality of the contacts was assessed by measuring the I-V curves between pairs of contacts. The electrical sheet resistivity ρ_s was measured in the van der Pauw geometry, which uses four contacts in a square configuration. A sweeping current was applied and the voltage between contacts measured (LakeShore Cryotronics, n.d.). The ρ_s data was plotted as a function of the particle weight fraction instead of the volume fraction because the volume that the nanoparticle-binder mixture occupies is not easily quantified due to the high surface roughness of the paper substrate. All measurements were performed at ambient conditions.

Results and discussion

Morphology of the NP and printed layers

Transmission electron micrographs of the metal powders (Figure 1) detail their polydispersed nature. The size of the NP varied between 50–100 nm for Pd and 20–50 nm for Ag. The Ag NP were spherical or slightly elongated, whereas the Pd NP were multifaceted.

Figures 2 and 3 show the SEM micrographs of printed Pd and Ag layers for particle weight fractions of 0.4 and 0.7. The printed layers are not typical metal composites in the sense that they are not a dense material comprising a reinforcing phase (particles) embedded in a matrix phase (polymer, ceramic). Our layers consist of the metal NP, the polymer binder, and voids left after the solvent has evaporated. The voids represent regions that are insulating for an electron current passing through the layer. There is a change in the

microstructure above and below p_c for both metallic layers. At low particle concentrations the NP aggregate to form small defined clusters. As the concentration is increased, the clusters become larger as smaller neighbouring clusters are incorporated. At high particle concentrations an almost uniform layer is formed. It can also be observed that the clusters of the Pd and Ag NP are structurally different. At a low particle concentration of $p = 0.4$, the Ag NP aggregate to form a more compacted packing structure that fills the regions between the paper fibres (Figure 2A), resulting in ‘isolated silver clusters’ separated by the paper fibres. The Pd layer shows a high degree of porosity at both low and high particle concentrations (Figure 3). The Pd NP aggregate to form ‘chain-like’ structures that extend over the paper fibres. The observed differences in the microstructure could be due to the presence of the dispersant in the Ag ink, which is not present in the Pd ink. This may affect the clustering of the particles during ink production and the printing process. Furthermore, the distinguishing features in the shapes of the particles can result in differences in their surface energies, and thus a variation in the way they cluster.

The I-V characteristics of the printed layers show ohmic behaviour for all particle concentrations, except for $p = 0.4$ of the Ag layers, which displayed nonlinear behaviour (Figure 4). Above p_c the nanoparticle clusters aggregate to form a continuous particle network that extends throughout the layer. Therefore the conductivity of the layer is expected to approach that of the bulk metal. Below p_c the clusters become isolated, resulting in fewer conducting paths. As a

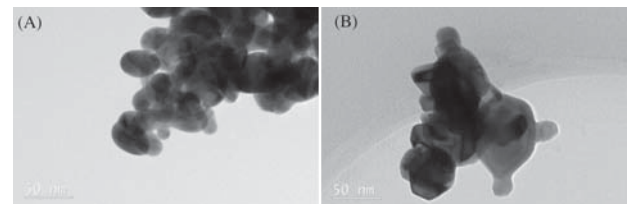


Figure 1—TEM images of (A) Ag NP, and (B) Pd NP

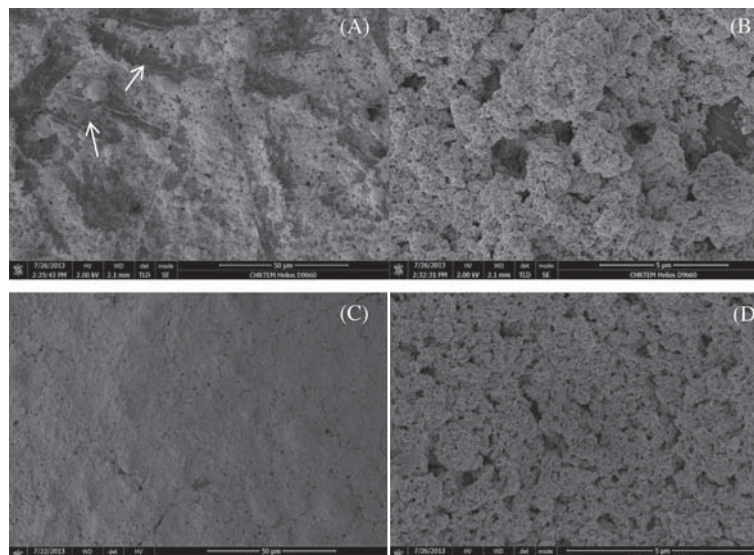


Figure 2—SEM micrographs of the printed Ag layers. (A, B) $p = 0.4$; (C, D) $p = 0.7$. Paper fibres indicated by arrows

Structural and electrical characteristics of printed silver and palladium nanoparticle networks

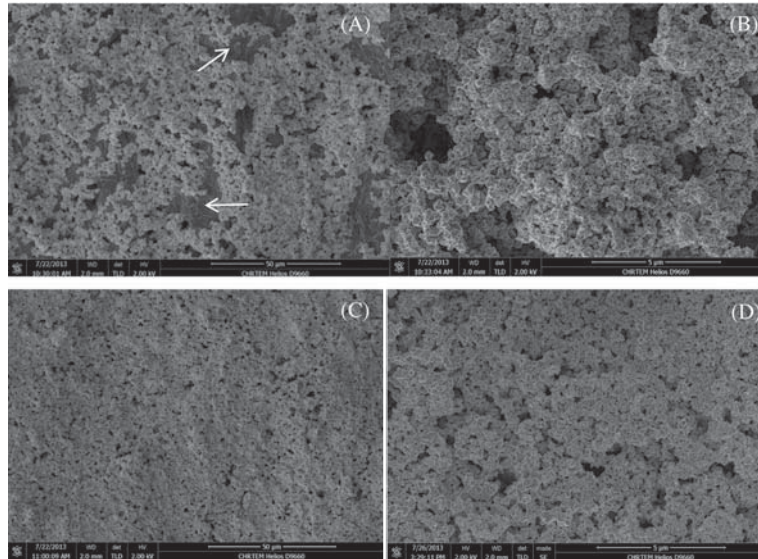


Figure 3—SEM micrographs of the printed Pd layers. (A, B) $p_c = 0.4$, (C, D) $p_c = 0.7$. Paper fibres indicated by arrows

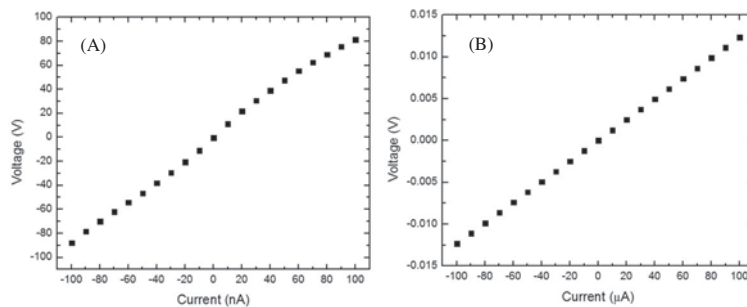


Figure 4—I-V curves for the Ag layer. (A) $p = 0.4$ and (B) $p = 0.7$

result, the conductivity of the layer deviates from the expected metallic behaviour (Zabet-Khosousi and Dhirani, 2008). Figure 5 shows the sheet resistivity ρ_s plotted as a function of the particle weight fraction. It is observed that the ρ_s increases as the particle concentration is decreased. The ρ_s of the Ag layer increases rapidly from 400 ohm/sqr to 200 ohm/sqr around a critical particle concentration of between 0.4-0.45 (Figure 5A). A smaller change in the ρ_s is observed in the Pd layers in the region of $p = 0.4-0.5$ (Figure 5B). The value of p_c will therefore lie somewhere in the concentration range. The percolation parameters, p_c and t , were determined from fitting the ρ_s data with Equations [1] and [2]. The results are shown in Table II. The GEM equation [2] gives a better fit to the Ag ρ_s data compared to the power law [1] which is valid only above p_c (Figure 5A,C). The percolation threshold for the Ag layer was determined to be at a weight fraction of approximately 0.45, which was in agreement with both fits. For the Ag layers, the critical exponent t determined from Equation [1] was lower than the value obtained from Equation [2]. The Pd ρ_s data fitted with Equation [1] indicated that p_c lies at a weight fraction of approximately 0.4 (Figure 5B). The GEM equation was unable to give a good fit to the Pd data. This is because of insufficient data points below p_c . The difference in p_c for the Pd and Ag layers can be attributed to the manner in which

the NP aggregate. Therefore this shows that p_c is largely affected by the microstructure of the layer. The values of the critical universal exponent t for the Pd and Ag layers are lower than the reported values (1.65–2.0) for a 3D percolation system (Sahimi, 1994).

Conclusions

In this study it has been shown that the sheet resistivity ρ_s of screen-printed nanoparticulate Ag and Pd layers is dependent on particle weight fraction. This behaviour can be described using the percolation power law and the GEM equation. The percolation parameters could be determined using these two equations. The value of p_c was found to be lower in the Pd layer than in the Ag layer. The variation of p_c in the two systems can be attributed to the differences in their microstructure. The values of t for the two systems were lower than those reported for a 3D percolation system.

Acknowledgments

Aspects of this work were supported by the Nano Power Africa Project funded by the US Agency for International Development (USAID) through the Higher Education for Development (HED) office. Additional funding to the UCT Nano Sciences Innovation Centre was provided by the US Air

Structural and electrical characteristics of printed silver and palladium nanoparticle networks

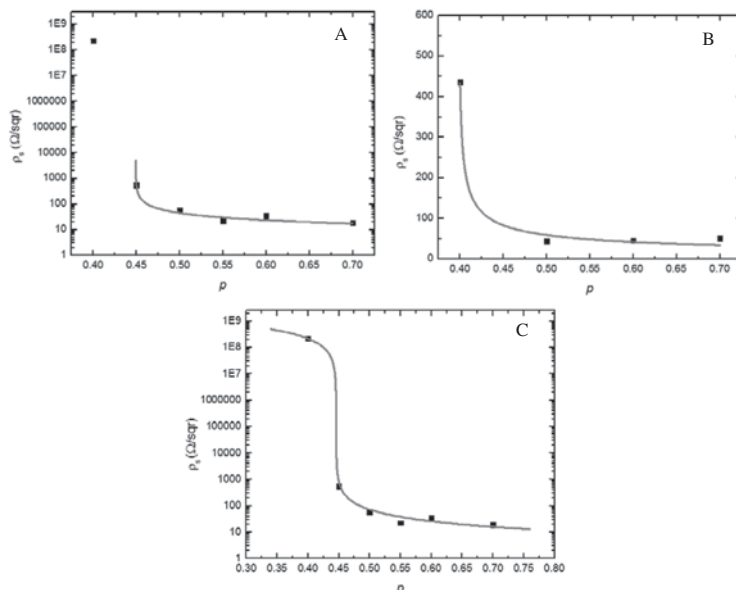


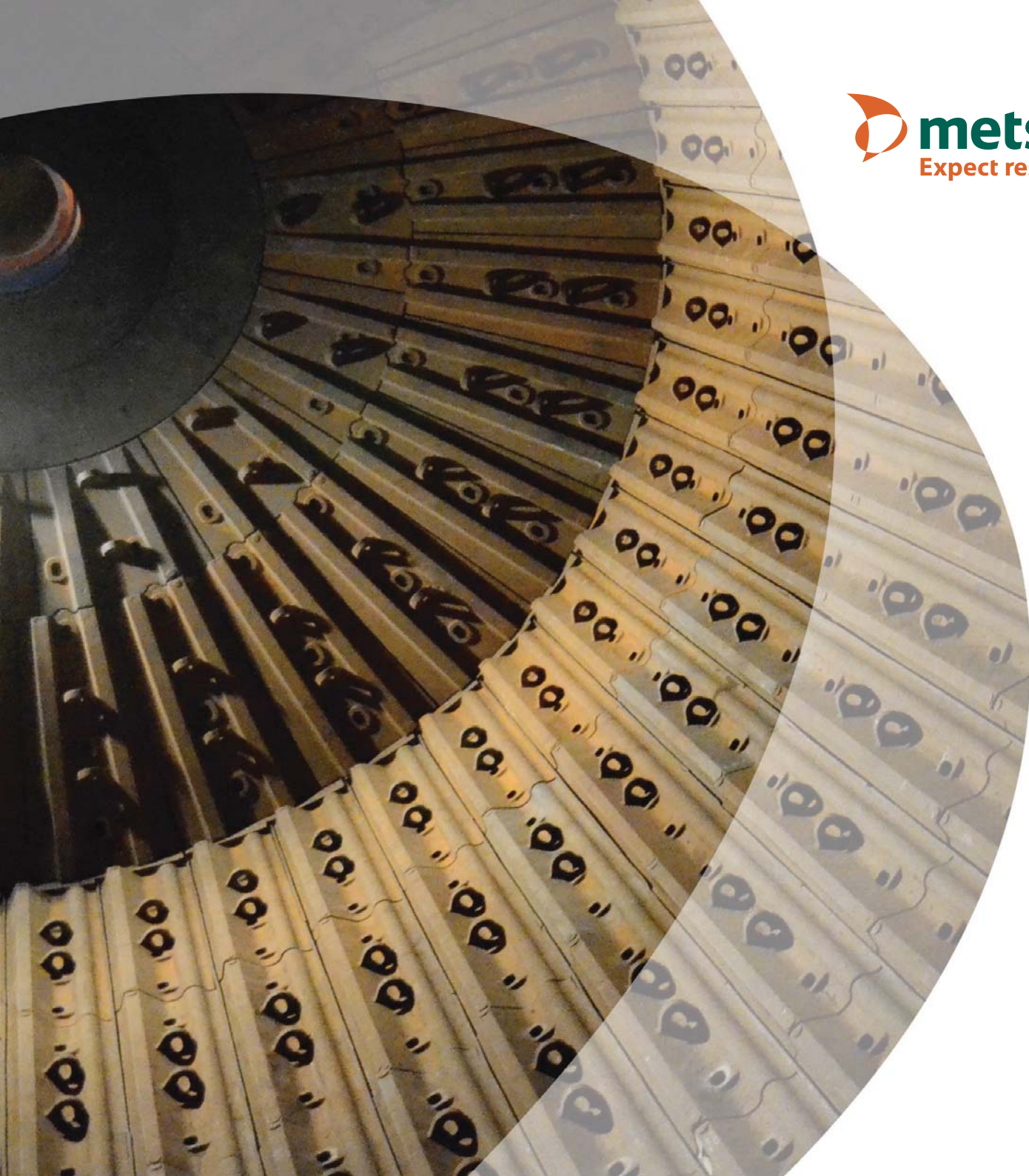
Figure 5—Graphs plotting ρ_s as a function of the nanoparticle weight fraction. (A) Ag and (B) Pd, fitted with Equation [1]. (C) Ag, fitted with Equation [2]

	σ_0	p_c	t	$\rho_i(\text{ohm/sqr})$	$\rho_s(\text{ohm/sqr})$
Equation [1]	Pd Ag	18.6 ± 0.56 7.62 ± 1.96	0.398 ± 0.006 0.449 ± 0.002	0.507 ± 0.005 0.595 ± 0.083	
Equation [2]	Ag	0.446 ± 0.021	0.975 ± 0.109	2.06×10^9	7.36 ± 1.00

Force Office of Scientific Research through the project ‘Nanoparticle Solutions for Printed Electronic Applications’, by the University of Cape Town Vice Chancellor’s Strategic Fund, and by the South African National Research Foundation (NRF) under area grants CPR20110717000020995 and CPR20110717000020998. Additional funding was provided by Mintek. The contents are the responsibility of the authors and do not necessarily reflect the views of HED, USAID, or the US Government or any of the organizations mentioned. The author would like to thank the Centre for High Resolution Transmission Electron Microscopy at Nelson Mandela Metropolitan University for help with the electron microscopy measurements.

References

- BRITTON, D.T. and HÄRTING, M. 2006. Printed nanoparticulate composites for silicon thick film electronics. *Pure and Applied Chemistry*, vol. 78, no. 9. pp. 1723–1739.
- FADDOL, R., REVERDY-BRUAS, N., and BOUREL, J. 2012. Silver content effect on rheological and electrical properties of silver pastes. *Journal of Materials Science: Materials in Electronics*, vol. 23, no. 7. pp. 1415–1426.
- HÄRTING, M., ZHANG, J., GAMOTA, D.R., and BRITTON, D.T. 2009. Fully printed silicon field effect transistors. *Applied Physics Letters*, vol. 94, no. 19. p. 3.
- KIRKPATRICK, S. 1973. Percolation and conduction. *Reviews of Modern Physics*, vol. 45, no. 4. p. 574.
- LAKE SHORE CRYOTRONICS. Not dated. LakeShore 7500/9500 Series Hall Series Hall System User’s Manual. Westerville, OH. www.lakeshore.com
- LEUENBERGER, H. 1999. The application of percolation theory in powder technology. *Advanced Powder Technology*, vol. 10, no. 4. pp. 323–352.
- McLACHLAN, D.S. 1990. A quantitative analysis of the volume fraction dependence of the resistivity of cermets using a general effective media equation. *Journal of Applied Physics*, vol. 68, no. 1. p. 195.
- McLACHLAN, D.S., BŁASZKIEWICZ, M., and NEWNHAM, R.E. 1990. Electrical resistivity of composites. *Journal of the American Ceramic Society*, vol. 73. pp. 2187–2205.
- NAN, C.-W., SHEN, Y., and MA, J. 2010. Physical properties of composites near percolation. *Annual Review of Materials Research*, vol. 40. pp. 131–151.
- ROLDUGHIN, V.I. and VYSOTSKII, V.V. 2000. Percolation properties of metal-filled polymer films, structure and mechanisms of conductivity *Progress in Organic Coatings*, vol. 39. pp. 81–100.
- SAHIMI, M. 1994. Applications of Percolation Theory. Taylor and Francis, London.
- SHIM, I.-K., LEE, Y.I., LEE, K.J., and JOUNG, J. 2008. An organometallic route to highly monodispersed silver nanoparticles and their application to ink-jet printing. *Materials Chemistry and Physics*, vol. 110. pp. 316–321.
- SICHEL, E.K. and GITTLEMAN, J.I. 1982. The Hall effect in granular metal films near the percolation threshold. *Solid State Communications*, vol. 42, no. 2. pp. 75–77.
- SUVAKOV, M. and TADIC, B. 2010. Modelling collective charge transport in nanoparticle assemblies. *Journal of Physics.: Condensed Matter*, vol. 22. pp. 163201–23.
- VYSOTSKY, V.V. and ROLDUGHIN, V.I. 1999. Aggregate structure and percolation properties of metal-filled polymer films. *Colloids and surfaces A: Physicochemical and Engineering Aspects*, vol. 160. pp. 171–180.
- ZABET-KHOSOUSI, A. and DHIRANI, A. 2008. Charge transport in nanoparticle



Metallic mill linings – a perfect fit

Metso has more than 30 years experience of designing customized metallic mill linings and developing high quality alloys. Reliable supply is ensured through local manufacturing in South Africa. Our complete range of products, combined with local production and service backed up by global support, makes Metso the world's most comprehensive supplier of mill linings.

For more information contact: +27 (11) 961 4000

www.metso.com | email: mmsa.info.za@metso.com



Investigating the chromium-platinum coated system

by N. Hanief*, C.I. Lang†, and M. Topics§

Synopsis

In this study, the effects of heat treatment on phase formation and surface morphology of the Cr-Pt coated system are investigated using X-ray diffraction and electron microscopy techniques. The CrPt and Cr₄Pt (Cr₃Pt - A15 type) phases were formed after heat treatment of the coated samples. Heat treating at 1000°C renders a distinct island coating morphology that is non-continuous in nature. A diffusional model is proposed for this coated system with regards to the surface morphology formation after heat treatment.

Keywords

coated systems, morphology, phase formation.

Introduction to the Cr-Pt coated system

The platinum-chromium system has been studied in depth over the last decade as it is known to form a crucial part of many alloy systems. In recent years this system, in applications such as catalysis and nanotechnology, has shown promise for fuel cells (Ghosh *et al.*, 2010; Koffi *et al.*, 2005; Escaño *et al.*, 2011). The study of thin films and coatings also proves useful in determining compositions and compounds with excellent properties that can be used as nano-materials for catalysis (Ghosh *et al.*, 2010). The use of coated systems, including Cr-Pt thin films, has increased recently in applications such as magnetic hard disk media (Ariake *et al.*, 2002; Uwazumi *et al.*, 2002; Kaitsu *et al.*, 2006) for the magnetic recording industry. Coated systems, as referred to in this study, are thick substrates (Cr in this work) with thin coatings (Pt) deposited on the surface. This study focuses on how coated systems are affected by heat treatment and the resulting effects on phase formation and surface morphology. The research aims to determine the mechanism of phase formation in this coated system, as it is known that coated systems behave differently to bulk systems in this regard (Pretorius *et al.*, 1993). Accordingly, experimental parameters can be controlled to form a desired phase with inherent properties for specific applications

(Pretorius *et al.*, 1993). Surface morphological changes are also monitored with respect to the diffusion characteristics of this coated system.

The formation of the coating after deposition can be described by nucleation and growth. These processes influence the grain structure that is developed, and ultimately the structural morphology of the coating after heat treatment (Ohring, 2002). Coatings are known to exhibit heterogeneous nucleation after being deposited, which can be described by the theory of capillarity (Ohring, 2002). The establishment of the coating introduces new surfaces and interfaces that provide an increase in the surface energy of the system. This causes coating systems to have different properties to bulk systems owing to the many surfaces that contribute to the total free energy. This can be described by the Gibbs free energy relation: the total Gibbs free energy is increased because in addition to the free energy of the system as a whole, the coated system now contains an interface region between the coating layer and substrate, as well as the surface free energy of the coating, acting upon it. Also inherent in coating layers is the high reactivity of elements, which is due to the increase in the density of the grain boundaries in coating layers also results in the high reactivity of elements (Ohring, 2002). This is caused by the high nucleation rate during the deposition process, which results in the formation of a fine-grained structure (Ohring, 2002). The thermodynamics of the

* Centre for Materials Engineering, University of Cape Town.

† Engineering Department, Macquarie University, Australia.

§ Materials Research Department, iThemba LABS Somerset West.

© The Southern African Institute of Mining and Metallurgy, 2014. ISSN 2225-6253. This paper was first presented at the, Precious Metals 2013 Conference, 14–16 October 2013, Protea Hotel, President, Cape Town, South Africa.



Investigating the chromium-platinum coated system

coated system govern the reactions that take place, as systems all strive towards the reduction of total free energy. Therefore reactions take place that continue to reduce the total free energy, and in comparing coated systems to bulk systems, the extra surfaces contribute to this reduction and thus ultimately contribute to the differences in properties between the two systems. This can also be related to a non-equilibrium description of the system, as in coated systems excess atoms available after compound formation will be available for the next compound to form (Pretorius *et al.*, 1993). Thus phase formation can also be attributed to the reduction in free energy of the system (Ohring, 2002).

The revised equilibrium phase diagram of the Cr-Pt system is shown in Figure 1. This binary phase diagram is known to contain two Cr₃Pt phases with different crystal structures. A congruent phase is formed at a temperature of 1599°C between 17.3 and 25 at.% Pt. This phase is designated the Cr₄Pt phase in the revised diagram, but it refers to the Cr₃Pt phase with the A15 crystal structure as described in the literature (Okamoto, 2009). The fcc phases include that of the L1₂ structure, which refers to the phases Cr₃Pt and CrPt₃, and the L10 crystal structure, which refers to the CrPt phase. After heat treatment, phase formation occurs at the interface region of the substrate and the coating. This phase formation is dependent on the processes of diffusion and the total energy of the system. Systems always tend to be driven towards a lower energy state. This can be taken into account via a thermodynamic description of the phases. Recent publications provide a good thermodynamic description of the Cr-Pt system (Preußner *et al.*, 2009; Zhang *et al.*, 2008).

Experimental procedure

Chromium (Cr) of 99.98% purity was used as substrates and prepared for electron beam deposition: pieces were cut using a diamond cutting wheel and ground to a 1200 grit finish using SiC grit paper. The substrates were then polished using an oxide polishing system with a colloidal silica suspension in the final polishing step. A cleaning procedure using solvents such as methanol, ethanol, acetone, and finally

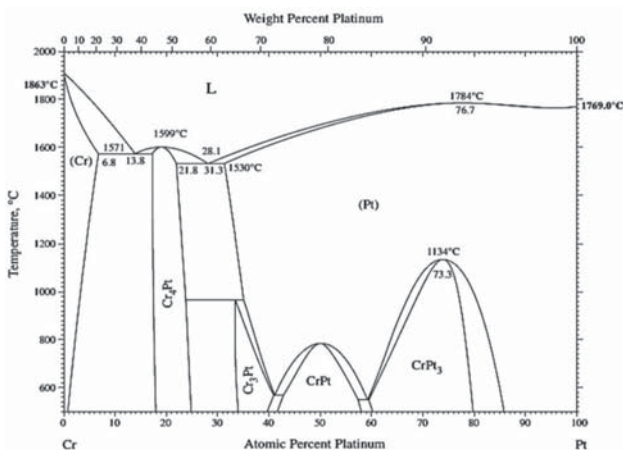


Figure 1—The revised equilibrium phase diagram of the Cr-Pt system (Okamoto, 2009)

hydrofluoric acid was used to sonicate samples and ensure that the coating would adhere to the substrate surface. Platinum (Pt) (purity of 99.99%) coatings were deposited with thicknesses of 0.1 μm and 0.3 μm . An electron beam sourced evaporation system was used with a deposition rate of 2.4 $\text{\AA}/\text{s}$ and a current of 150 mA. High vacuum conditions were present within the deposition chamber under a pressure of 5×10^{-4} Pa. After deposition, samples were heat treated for 8 hours at a range of different temperatures. These included temperatures of 700, 800, 900, and 1000°C followed by slow furnace cooling, with both heating and cooling rates controlled at 10°C/min. The substrate (after cleaning) and the coated sample before heat treatment are used as references to compare the morphological changes and the subsequent changes in phase formation.

A range of complementary techniques was used to analyse the coatings, including X-ray diffraction (XRD) with analysis using the Rietveld method. A Bruker D8-ADVANCE monochromatic diffractometer was used to obtain XRD patterns, with measurements carried out using of CuK α radiation at 1.5418 \AA . Using parameters of 40 kV and 40 mA, diffraction data was measured between 2 θ values of 30° and 70° at a 0.03° step size. Phases were identified by matching diffraction peaks using the database of the International Centre for Diffraction Data. Rietveld refinements were performed to determine the volume fraction of phases present within the samples. For this, the TOPAS 4.1 software was used, whereby the peak shapes of all the phases were modelled with the use of pseudo-Voigt functions (Coelho, 2007).

The microscopy techniques used involve both scanning and transmission electron microscopy (SEM and TEM). SEM in the backscattered electron mode (BSE) was used to observe changes in the morphology after heat treatment. A NOVA NANOSEM 230 was used at 20 kV to image the surface of the coating layer after heat treatment. In preparation for TEM, samples were milled in cross section using a focused ion beam (FIB). Prior to milling, a carbon layer was deposited on the area of interest of the coating surface to maintain the integrity of the coating during ion milling. A FEI Helios NANOLAB 650 FIB-SEM was operated using a Ga ion beam at 30 kV. The cross section was transferred to a Cu grid using an Omniprobe lift-out needle as part of the FIB-SEM, and final polishing of the section was completed at 500 eV to a thickness of 50 nm. For an in-depth characterization of the coating layer, scanning TEM (STEM) was performed using a JEOL 2100F TEM operating at 200 kV. Annular dark field (ADF) imaging was obtained of the coating layers in cross section. Energy dispersive spectroscopy (EDS), which provides an elemental quantification of the sample, was used as part of the STEM mode. Spot analyses of the coating layer in cross section were determined in the characteristic X-ray mode. The results for the 0.1 μm and 0.3 μm Pt coated samples, heat treated for 8 hours at different temperatures, are shown.

Results and discussion

The techniques used in this study complement one another in analysing the phase formation and surface morphology of Cr-Pt coated systems.

Investigating the chromium-platinum coated system

The formation of phases

Phase formation in the Cr-Pt coated system was analysed using XRD and the Rietveld method (Coelho, 2007). The samples used for analysis had Pt coatings of 0.1 μm and 0.3 μm . These samples were heat treated at temperatures ranging from 700°C to 1000°C for the 8-hour time interval. A reference pattern was also obtained of the Pt coated condition prior to heat treatment. This is shown in Figure 2, where peaks correspond to those of Cr and Pt with no phase formation. This shows that phase formation occurs only after the heat treatment. Also shown in Figure 2 are the XRD patterns for the 0.1 μm Pt coated samples that were heat treated. Two phases are seen to have formed after heat treatment at the range of temperatures considered. These include the formation of the CrPt phase observed at 700°C and the subsequent formation of the Cr₃Pt phase at 800–1000°C. The phases observed correspond to the revised equilibrium phase diagram (Figure 1). After heat treatment, the peaks for Pt are not seen, indicating that the Pt is consumed to form the CrPt and Cr₃Pt phases.

Figure 3 shows the XRD patterns of the 0.3 μm Pt coated samples after heat treatment. A Pt peak at can be seen at 700°C, indicating that the Pt has not been entirely consumed at this point. However, as the temperature is increased, the Pt peak disappears and the consumption of Pt is evident. Even though the Pt is not entirely consumed at 700°C, formation of the CrPt phase is still observed. Owing to the thicker Pt coating, the amount of Pt available for phase formation increases, and the CrPt phase now forms at temperatures of 700°C and 800°C. At 800°C, the CrPt and Cr₃Pt phases coexist. At 900°C and 1000°C the Cr₃Pt phase is the only phase to form. The Cr peaks are observed at all temperatures for both coating thicknesses. It can be inferred at this point that the CrPt phase decomposes to form the Cr₃Pt phase owing to the fact that after complete formation of the CrPt phase, the next phase to form is the phase richer in the unreacted element (Pretorius *et al.*, 1993), which in this case is the excess Cr from the thick substrate.

Volume fraction analysis

The volume fraction analysis was completed using the Rietveld method with pseudo-Voigt functions to model peak

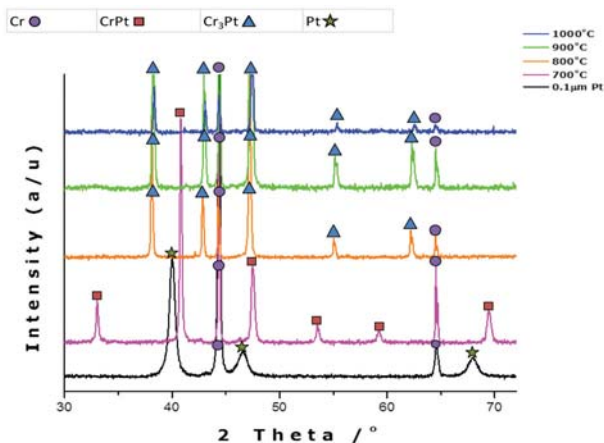


Figure 2—XRD patterns of the 0.1 μm Pt coated samples heat treated for 8 hours at different temperatures

shapes (Coelho, 2007). The volume fraction of the phases is determined using the area under each peak and corresponds to the intensity of each phase. The graphical representation in Figure 4 shows the volume fraction of phases for the 0.1 μm Pt coated samples after heat treatment at different temperatures. At 700°C the volume fraction of the CrPt phase is at approximately 40%, decreasing to zero as the temperature is increased. Subsequently, the Cr₃Pt volume fraction is increased from zero at 700°C to approximately 50% with an increase in temperature to 800°C, then decreases with a further increase in temperature from 800°C to 1000°C, with an increase in the volume fraction of a Cr-rich phase. This can be attributed to the change in coating morphology, which is described below, and the interaction volume of the X-ray beam. For the 0.3 μm Pt coated samples (Figure 5), the CrPt phase follows the same trend as before with increasing temperature, and decreases in volume fraction as the Cr₃Pt phase increases. At 0.3 μm coating thickness, however, more Pt is available for the formation of phases and thus the CrPt phase is now observed at a temperature of 800°C before decomposition is complete. With regard to phases forming sequentially in coating systems, it could be said that the decomposition of the current phase brings about the subsequent formation of a new phase. Thus, if these experimental parameters are manipulated, heat treatment at 1000°C promotes the formation of the Cr₃Pt phase, and at 700°C the

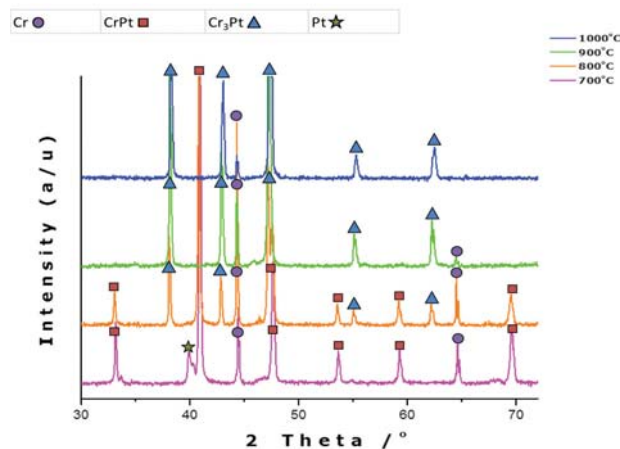


Figure 3—The formation of the CrPt and Cr₃Pt phases after heat treatment as seen in the XRD patterns of 0.3 μm Pt coated samples after heat treatment

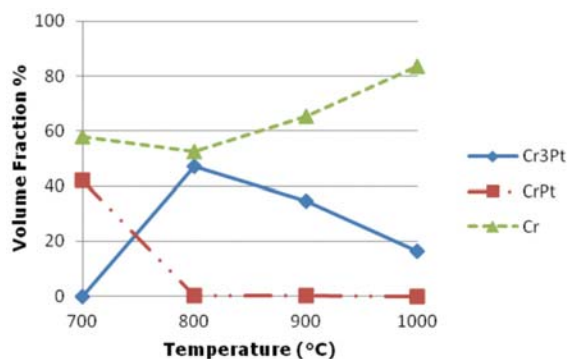


Figure 4—Rietveld analysis showing the volume fraction of the phases present in the 0.1 μm Pt coated samples after heat treatment

Investigating the chromium-platinum coated system

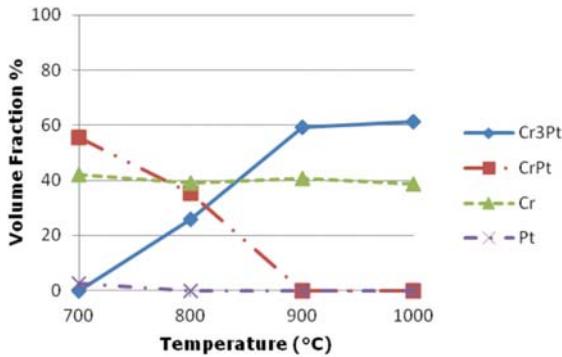


Figure 5—Rietveld analysis showing the volume fraction of the phases present in the 0.3 μm Pt coated samples after heat treatment

CrPt phase can be formed. A recent review of the Pt-Cr coated system attempted to relate the effective heat of formation (EHF) model with its phase formation sequence (Hanief *et al.*, 2012). To predict phase formation in this coated system, a more comprehensive study needs to be completed.

Morphological characterization

The following sections describe the results obtained using electron microscopy techniques to characterize the surface morphology of the Cr-Pt coated system after heat treatment, with a view to understanding the processes involved. SEM was used to image the surface of the coating layer, and STEM to image the coating layer and substrate in cross section, both after heat treatment. An elemental quantification is given with the use of EDS spot analyses.

Scanning electron microscopy

The surface morphology of the Cr-Pt coating layer after heat treatment was imaged using SEM in the characteristic BSE mode, as this technique is sensitive to contrast differences with regards to atomic number. Figure 6 shows the coating morphology of the reference samples. A relatively smooth surface finish is seen for both the substrate that had been polished with an oxide polishing system (a) and the coated sample prior to heat treatment (b). In Figure 7, the surface morphology of the coating layer is shown for the 0.1 μm Pt coated samples after heat treatment at different temperatures. As can be seen, the morphology of the Cr-Pt coated system changes significantly as the heat treatment temperature is increased. A relatively more uniform morphology is observed for temperatures of 700°C and 800°C (Figure 7a and b). At 900°C and 1000°C, however (Figure 7c and d), an island-like morphology is seen where the coating layer (1) is separated by thermal grooving of the grain boundary of the substrate. The compositional differences can be attributed to Pt being a heavier element than Cr, thus the contrast of Pt in the coating layer appears brighter in the image. With an increase in coating thickness to 0.3 μm , as seen in Figure 8, the Pt coatings after heat treatment are more uniform in morphology and do not show the islands as prominently as with the thinner coating, even as the temperature is increased. It can thus be said that the coating morphology

depends on the temperature of the heat treatment and also on the coating thickness. The area of interaction of the X-ray beam with the sample is between 1 and 2 mm^2 . Therefore, for the samples heat treated at 1000°C with the non-continuous coating layer, the XRD measurements include part of the substrate region, which could result in measured decrease in the Cr3Pt volume fraction.

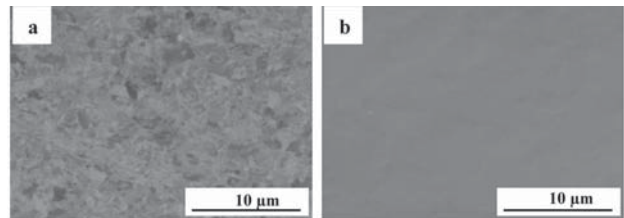


Figure 6—(a) Cr substrate and (b) Pt coated sample before heat treatment

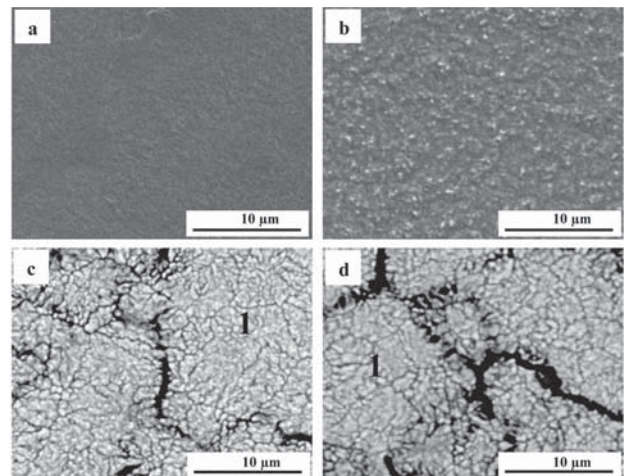


Figure 7—SEM-BSE images for the 0.1 μm Pt coated samples heat treated for 8 hours at (a) 700°C, (b) 800°C, (c) 900°C, and (d) 1000°C with (1) indicating the Pt coating layer at 900°C and 1000°C

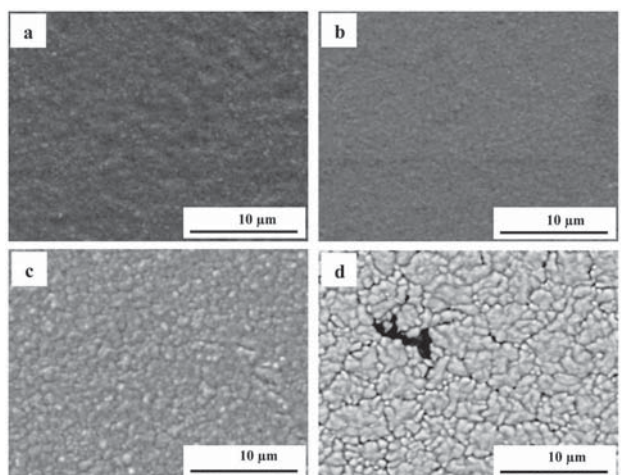


Figure 8—Pt coatings of 0.3 μm , heat treated at (a) 700°C, (b) 800°C, (c) 900°C, and (d) 1000°C for 8 hours shown by BSE imaging

Investigating the chromium-platinum coated system

The surface morphology that is formed in this coated system can be ascribed to a diffusional process. As mentioned previously, the formation of coatings after deposition renders a fine grain structure with many grain boundaries (Ohring, 2002). It is said that one of three growth modes can occur during coating formation. Owing to the surface energy of the coating and substrate in the system studied, the island growth mode occurs (Ohring, 2002). This is because the surface energy of Pt is higher than that of Cr (Ohring, 2002). Owing to this growth mode and the fine recrystallized grain structure that evolves during the formation of the coating, the application of heat treatment allows for rapid diffusion along the grain boundaries, both within the coating layer diffusing towards the substrate as well as within the substrate diffusing towards the coating. The activation energies for grain boundary diffusion are smaller than that of the lattice, leading to high diffusivity rates in this regard (Ohring, 2002). The solid solution range of Pt and Cr is broad, extending from 31.3 at.% Pt at 1530°C to 100 at.% Pt at 1769°C (Figure 1), indicating that the solubility of Cr in Pt is very high. This relates to the high affinity Cr has for Pt and indicates that the bulk of the grain boundary diffusion occurs where Cr diffuses into the Pt coating, initiating phase formation. The new phase nucleates at this point, with subsequent lateral diffusion at the interface region and surface diffusion of the coating and the substrate, which are thermodynamically favoured. Subsequent growth of the phase takes place at the interface region until the coating layer is formed. As the heat treatment continues, thermal grooving is observed, which is attributed to surface diffusion driven by surface curvature (Ohring, 2002). A coalescence mechanism is proposed to occur next, wherein larger islands grow in size at the expense of smaller island, such as the process of Ostwald Ripening (Ohring, 2002). What can also be noted in Figure 7 and Figure 8 is the progressive agglomeration of the coating layer as the temperature increases, resulting in the fine separation of agglomerates on the coating surface. This in turn increases the surface roughness and occurs as a result of dewetting of the coating layer (Lee and Kim, 2007). The fine separation of agglomerates is said to be energetically favoured at elevated temperature and thus dewetting of the substrate occurs, allowing the coating layer to rearrange itself into an energetically favourable state by the subsequent minimization of the surface free energy (Lee and Kim, 2007). The surface morphology of this coated system is governed by the reduction of the surface free energy which follows a surface energy increase caused by an increase in the number of surfaces present within coating systems in general. The diffusional model serves to describe the complex processes involved in the formation of the surface morphology that are driven by the minimization of the total energy of the system to form an equilibrium phase and structure.

Scanning transmission electron microscopy

The STEM mode was used to acquire annular dark field (ADF) imaging of the cross section of the coating layer after heat treatment. ADF images show contrast effects related to atomic number, as seen in the BSE images. Figure 9 shows the ADF image of the 0.1 μm Pt coated sample heat treated at 1000°C for 8 hours. The light contrast depicts the heavier

element, which can be seen in the coating layer (1), with substrate (2) being darker in contrast. The initial coating prior to heat treatment was 0.1 μm , increasing to approximately 0.5 μm after heat treatment. As the phase formed in this sample is known to be the Cr_3Pt phase, this can partially account for the increase in coating thickness after heat treatment. The cross section of the island-like sample shows a non-continuous coating layer morphology on the surface of the substrate, as expected from the SEM images. According to the diffusional model proposed, the non-continuous coating layer morphology is attributed to various mechanisms such as the island growth mode with recrystallized grain structure in the coating formation, the mechanisms of diffusion involving the grain boundary, surface, and interface, as well as Ostwald ripening and dewetting processes to form the island-like morphology. This also plays a role in the increase of the coating thickness after heat treatment. Agglomeration and dewetting of the coating layer, which is driven by surface curvature (Lee and Kim, 2007), increases the thickness of the non-continuous coating layer as seen in cross section.

Energy dispersive spectroscopy

EDS was used for elemental composition analysis of the coating layer after heat treatment. Spot analyses were determined in characteristic X-ray mode, and the position of each spot is shown in Figure 10. The composition of each spot determined is given in Table I. Spots 1–5, taken within the coating layer region, have an average composition of 24 at.% Pt. This inherently corresponds to the Cr_4Pt (Cr_3Pt with A15 crystal structure) phase as seen in the revised equilibrium phase diagram (Figure 1). The literature also confirms that Cr_4Pt (Cr_3Pt with A15 crystal structure) is stable and thus masks the formation of the Cr_3Pt (L_{12}) phase (Okamoto, 2009). This result is in agreement with the XRD analysis, which showed the formation of this phase after the heat treatment of 1000°C. Spots 6–8, within the substrate region, correspond to the Cr substrate. Thus the Cr_3Pt phase referred to in all the results is that of the A15 type crystal structure or the Cr_4Pt phase, otherwise known as Cr_3Pt with A15 crystal structure.

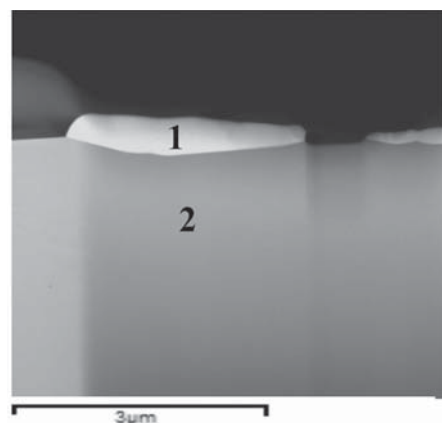


Figure 9—ADF image of the 0.1 μm Pt coated sample in cross section, heat treated at 1000°C, showing the Cr-Pt coating layer (1) and substrate

Investigating the chromium-platinum coated system

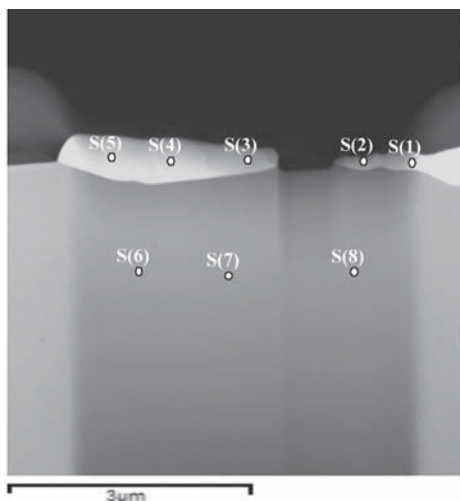


Figure 10—ADF image of sample heat treatment at 1000°C showing EDS spot analysis positions

Table 1
Composition of the positions shown in Figure 10

Spot	Cr (at %)	Pt (at %)
S(1)	74.7	25.3
S(2)	73.5	26.5
S(3)	76.1	23.9
S(4)	78.4	21.6
S(5)	78.4	21.6
S(6)	100.0	0
S(7)	100.0	0
S(8)	100.0	0

Conclusions

A non-continuous coating layer with increased thickness is formed during heat treatment of Pt coatings deposited on Cr substrates. The phases formed in the coating layers correspond to the CrPt and Cr₃Pt (A15) phases. Phase formation is affected by the coating thickness and the temperature and duration of the heat treatment. The experimental parameters can be manipulated to form the CrPt and Cr₃Pt (A15) phases. A diffusional model is proposed, by which the minimization of the total free energy within the coated system is maintained, and which includes the processes of an island growth mode in the coating formation, and mechanisms of diffusion that include grain boundary, lateral, and surface diffusion, as well as thermal grooving, Ostwald ripening, and subsequent dewetting of the coating to form an island-like surface morphology after heat treatment.

Acknowledgments

The authors wish to acknowledge Mintek and the National Research Foundation for funding this research. The use of the facilities at the Centre for Materials Engineering, and Electron Microscope Unit, UCT; Solid-State and XRD laboratories at iThemba LABS, Somerset West; and the Centre for

High Resolution Transmission Electron Microscopy, NMMU is greatly appreciated.

References

- ARIAKE, J., HONDA, N., OUCHI, K., and IWASAKI, S. 2002. Pt and Pd intermediate layers for controlling Co–Cr–Nb–Pt layer growth in double layered perpendicular magnetic recording media. *Journal of Magnetism and Magnetic Materials*, vol. 242–245. pp. 311–316.
- COELHO, A. 2007. TOPAS V4.1, Coelho Software, Brisbane, Australia.
- ESCAÑO, M.C., GYENGE, E., NAKANISHI, H., and KASAI, H. 2011. Pt/Cr and Pt/Ni catalysts for oxygen reduction reaction: to alloy or not to alloy? *Journal of Nanoscience and Nanotechnology*, vol. 11. pp. 2944–2951.
- GHOSH, T., LEONARD, B.M., ZHOU, Q., and DISALVO, F.J. 2010. Pt alloy and intermetallic phases with V, Cr, Mn, Ni, and Cu: synthesis as nanomaterials and possible applications as fuel cell catalysts. *Chemistry of Materials*, vol. 22. pp. 2190–2202.
- HANIEF, N., LANG, C.I., BUCHER, R., and TOPIC, M. 2012. Phase transformations and surface characterization of the platinum-chromium coated system. *Journal of the Southern African Institute of Mining and Metallurgy*, vol. 112. pp. 5–7.
- KAITSU, I., INAMURA, R., TODA, J., and MORITA, T. 2006. Ultra high density perpendicular magnetic recording technologies. *Fujitsu Scientific & Technical Journal*, vol. 130. pp. 122–130.
- KOFFI, R.C.C., COUTANCEAU, C., GARNIER, E., LÉGER, J.-M., and LAMY, C. 2005. Synthesis, characterization and electrocatalytic behaviour of non-alloyed PtCr methanol tolerant nanoelectrocatalysts for the oxygen reduction reaction (ORR). *Electrochimica Acta*, vol. 50. pp. 4117–4127.
- LEE, J.-M. and KIM, B.-I. 2007. Thermal dewetting of Pt thin film: etch-masks for the fabrication of semiconductor nanostructures. *Materials Science and Engineering A*, vol. 449–451. pp. 769–773.
- OHRING, M. 2002. *Materials Science of Thin Films*. Academic Press, London.
- Okamoto, H. 2009. Cr–Pt (chromium–platinum). *Journal of Phase Equilibria and Diffusion*. vol. 30. pp. 295–296.
- PRETORIUS, R., MARAIS, T.K., and THERON, C.C. 1993. Thin film compound phase formation sequence: an effective heat of formation model. *Materials Science and Engineering A*, vol. 10. pp. 1–83.
- PREUßNER, J., PRINS, S., VÖLKL, R., LIU, Z.-K., and GLATZEL, U. 2009. Determination of phases in the system chromium–platinum (Cr–Pt) and thermodynamic calculations. *Materials Science and Engineering A*, vol. 510–511, pp. 322–327.
- UWAZUMI, H., SAKAI, Y., and TAKENOIRI, S. 2002. Magnetic layers for perpendicular recording media. *Fuji Electric Review*, vol. 48. pp. 73–77.
- ZHANG, C., ZHU, J., BENGTON, A., MORGAN, D., ZHANG, F., YANG, Y., and CHANG, Y.A. 2008. Thermodynamic modeling of the Cr–Pt binary system using the cluster/site approximation coupling with first-principles energetics calculation. *Acta Materialia*, vol. 56. pp. 5796–5805. ◆



Technical and economic aspects of promotion of cobalt-based Fischer-Tropsch catalysts by noble metals—a review

by M. de Beer*, A. Kunene*, D. Nabaho*†, M. Claeys*†, and E. van Steen*†

Synopsis

The conversion of carbon-containing feedstock into liquid fuels can proceed via the Fischer-Tropsch synthesis, which is catalysed using supported cobalt catalysts. These catalysts contain noble metals to facilitate the reduction of oxidic cobalt species in the catalyst precursor to metallic cobalt, which is the catalytically active species for the Fischer-Tropsch synthesis. This is thought to occur via hydrogen spillover, i.e. the diffusion of atomic hydrogen over the support from the noble metal to the oxidic cobalt moieties. Noble metals may also affect the dispersion of cobalt in the active Fischer-Tropsch catalyst. The economic aspect of the addition of noble metals to the Fischer-Tropsch catalyst is discussed.

Keywords

catalysis, supported cobalt catalyst, noble metals, Fischer-Tropsch synthesis.

Background

The world depends on transportation fuels, which are classically obtained from oil refining. The dwindling resources of oil in conjunction with the increased costs of crude oil over the last decade yielded an opportunity for the synthesis of transportation fuels from other carbon-containing resources, such as natural gas, biomass, coal, or oil residue. The conversion of these materials into transportation fuels may proceed via the synthesis gas route, in which the carbon-containing feedstock is converted into synthesis gas, a mixture of H₂ and CO. Following a cleaning step and possibly the water-gas shift reaction, synthesis gas can be converted into long-chain hydrocarbons via the Fischer-Tropsch synthesis (Claeys and Van Steen, 2004). The long-chain hydrocarbons can subsequently be hydrocracked to yield high-quality diesel. The resulting product is low in aromatics (and has therefore a high cetane number (Knottenbelt, 2002; Lamprecht, Dancuart, and Harrilall, 2007; Leckel, 2011), and has a low nitrogen and sulphur content. These characteristics make this diesel a low-emission fuel (Knottenbelt, 2002; Huang, Wang, and Zhou, 2008; Hewu *et al.*, 2009) and an ideal blending agent.

Figure 1 shows a generic overview of the Fischer-Tropsch process for fuel production. The carbon source is gasified (in the case of biomass/coal/or oil residue as a feedstock) or reformed (using natural gas as a feedstock), yielding a mixture of synthesis gas, CO₂, and H₂O. In addition, this mixture contains compounds that are poisons for downstream processes, such as H₂S, N-containing compounds, tars, and even alkali compounds (if biomass is used as a feedstock). These compounds have to be removed in the gas cleaning stage. Furthermore, the H₂/CO ratio of the synthesis gas can be adjusted using the water-gas shift reaction, after which CO₂ removal and water removal is required. The clean synthesis gas (with poison levels down to ppm or even ppb levels (Van Steen and Claeys, 2008)) is fed to the Fischer-Tropsch reactor. Some hydrogen is separated from this feed stream for downstream processing. The synthesis gas is partially converted in the Fischer-Tropsch reactor, with some of the unconverted gas being recycled to the Fischer-Tropsch reactor and some being recycled to the gasifier/reformer to ensure a high overall conversion. The liquid products of the Fischer-Tropsch synthesis are separated and the heavy fraction is hydrocracked back into the diesel range.

The Fischer-Tropsch synthesis, which is the heart of the Fischer-Tropsch process, is the hydrogenation of carbon monoxide yielding long-chain hydrocarbons (Schulz, 1985), which is catalysed using transition metals, although carbides (Anderson, 1956; Ranhotra,

* Centre for Catalysis Research, Department of Chemical Engineering, University of Cape Town, Rondebosch, Cape Town, South Africa.

† DST-NRF Centre of Excellence in Catalysis.

© The Southern African Institute of Mining and Metallurgy, 2014. ISSN 2225-6253. This paper was first presented at the, Precious Metals 2013 Conference, 14–16 October 2013, Protea Hotel, President, Cape Town, South Africa.

Technical and economic aspects of promotion of cobalt-based Fischer-Tropsch catalysts

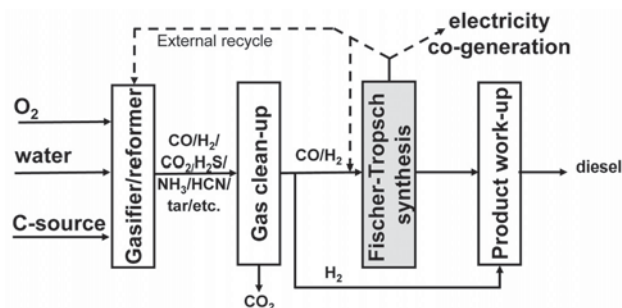


Figure 1—Schematic overview of a generic Fischer-Tropsch process for the production of diesel

Bell, and Reimer, 1987; Patterson, Das, and Davis, 2003) and nitrides (Ranhotra, Bell, and Reimer, 1987) may also catalyse this reaction. A common feature of these materials is their strong interaction with CO and the ability to dissociate adsorbed carbon monoxide. It should be noted that the CO adsorption should be neither too strong nor too weak, since this will lead to methanation rather than chain growth (Van Santen *et al.*, 2012). Coupling of partially hydrogenated surface intermediates leads to the formation of long-chain surface species, which upon desorption form a mixture of organic product compounds.

Vannice (1975) explored the intrinsic activity and selectivity of transition metals supported on γ - Al_2O_3 in different H_2/CO mixtures at temperatures between 240–280°C and at 1 bar. It was concluded that activity for methane formation follows the order of $\text{Ru} > \text{Fe} > \text{Ni} > \text{Co} > \text{Rh} > \text{Pd} > \text{Pt} > \text{Ir}$, whereas the average molecular weight of the product follows the order of $\text{Ru} > \text{Fe} > \text{Co} > \text{Rh} > \text{Ni} > \text{Ir} > \text{Pt} > \text{Pd}$. On silica as a support, the order of activity was mainly retained, but cobalt was now the most active material (Vannice, 1997).

The comparative studies by Vannice (1995, 1997) show that for the production of long-chain hydrocarbons ruthenium, cobalt, iron, and to a lesser extent nickel are the metals of choice. From an industrial point of view, the cost of the catalytic active material must be taken into account as well (Van Steen and Claeys, 2008). Hence, iron and cobalt-based catalysts are the industrially used Fischer-Tropsch catalysts. Van Berge and Everson (1997) compared the performance of iron and cobalt-based catalysts in a slurry reactor under realistic Fischer-Tropsch conditions and defined regimes in which the cobalt-based catalyst was more active than a precipitated iron catalyst. The cobalt-based catalyst showed a higher productivity at lower relative space velocity and lower reactor pressures. This was ascribed to the higher resistance of cobalt-based catalysts to higher water partial pressures. This means that a higher conversion per pass can be achieved with the cobalt-based catalyst, thereby improving the economics of the overall Fischer-Tropsch process (see also Botes, Niemantsverdriet, and Van de Loosdrecht, 2013). Cobalt catalyst also shows a low activity for the formation of CO_2 under Fischer-Tropsch conditions up to moderate levels of conversion (Ma *et al.*, 2011), making it ideal for the conversion of synthesis gas with a feed ratio of H_2/CO of 2. Furthermore, cobalt catalysts are preferred when a product with a low degree of branching is desired (Van Steen *et al.*, 1996).

Supported cobalt catalysts for the Fischer-Tropsch synthesis

The Fischer-Tropsch synthesis is a surface reaction (Claeys and Van Steen, 2004) and the cobalt-based Fischer-Tropsch synthesis is catalysed by the surface of metallic cobalt (Iglesia, 1997). Hence, smaller metallic crystallites should display a higher activity per unit mass of catalytically active material.

It has been observed that the intrinsic catalytic activity decreases with decreasing average crystallite size of the cobalt crystallite for metallic cobalt crystallites less than 6–10 nm (Barbier *et al.*, 2001; Bezemer *et al.*, 2006; Martínez and Prieto, 2007; Fischer, Van Steen, and Claeys, 2013). Hence, the mass-specific activity of cobalt-based Fischer-Tropsch catalysts passes a maximum as a function of the crystallite size (Den Breejen *et al.*, 2010), since with increasing crystallite size of the active phase the intrinsic activity of surface atoms increases, but the dispersion (i.e. the fraction of metal atoms at the surface) decreases (see Figure 2). Thus, ideally, the most active catalyst contains all cobalt in crystallites of a defined crystallite size, although the exact position of this optimum crystallite size depends on the nature of the dependency of the surface atom specific activity on the crystallite size, which has not yet been established beyond doubt.

The synthesis of supported cobalt-based catalysts has been reviewed by Khodakov, Chu, and Fongarland (2007). These catalysts are typically synthesized by impregnation (most commonly using cobalt nitrate as the cobalt source). The resulting metallic crystallites are somehow related to the average pore diameter of the support material (Khodakov *et al.*, 2001; Saib, Claeys, and Van Steen, 2002; Borg *et al.*, 2001), although cobalt supported on materials with a small average pore diameter might be located on the outer surface or in the larger pores of the materials (Saib, Claeys, and Van Steen, 2002). The impregnation of γ - Al_2O_3 or SiO_2 with cobalt nitrate yields clusters of cobalt crystallites (Feller, Claeys, and Van Steen, 1999; Storsæter *et al.*, 2005), i.e. regions with a typical diameter of approximately 100–400 nm with cobalt crystallites and regions without cobalt crystallites. This phenomenon is not observed with supports with a large average pore diameter, such as α - Al_2O_3 and TiO_2 (Storsæter *et al.*, 2005). Drying of the catalyst precursor will lead to the formation of cobalt nitrate droplets, which are typically of the

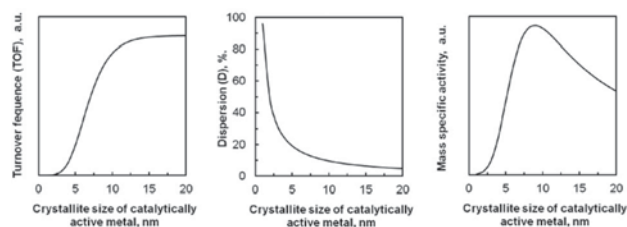


Figure 2—Schematic dependence of observed catalytic activity per surface atom in working cobalt-based Fischer-Tropsch synthesis (Barbier *et al.*, 2001; Bezemer *et al.*, 2006; Martínez and Prieto, 2007; Fischer, Van Steen, and Claeys, 2013) (left), the dispersion, i.e. the number of surface atom relative to the total number of atoms in a metallic cobalt crystallite (centre), and the corresponding activity per unit cobalt mass (right) as a function of the cobalt metal crystallite size

Technical and economic aspects of promotion of cobalt-based Fischer-Tropsch catalysts

size of the resulting clusters. Calcination of the droplets results in the formation of multiple Co_3O_4 crystallites, which will be trapped within the constraint of a narrow pore system, but will spread over a larger support area in systems with a large average pore diameter.

Reduction of cobalt oxide on materials with a large average pore diameter may result in break-up, leading to smaller crystallites (Borg *et al.*, 2001; Hauman *et al.*, 2012). The preparation of relatively large cobalt crystallites with a size of approximately 8–10 nm therefore requires support materials with an average pore diameter between 10–15 nm.

The use of supported catalysts results in a change in the ease of the transformation of the oxidic catalyst precursor into the catalytically active, metallic, phase. This is typically evidenced using temperature programmed reduction (TPR), in which the catalyst sample is reduced in a hydrogen-containing gas, while the temperature is linearly increased (see Figure 3). The TPR profile is characterized by multiple peaks, which represent different processes taking place with different reaction kinetics. The TPR profile of pure Co_3O_4 is characteristic of the two-stage reduction process $\text{Co}_3\text{O}_4 \rightarrow \text{CoO} \rightarrow \text{Co}$ (Van Steen *et al.*, 1996; Li *et al.*, 2009; Rane *et al.*, 2010). The oxide-supported Co_3O_4 shows a number of additional peaks. The additional low-temperature peak might be attributed to either reductive nitrate decomposition of residual nitrates in a catalyst synthesized from cobalt nitrate (see Figure 4 and Van Steen *et al.*, 1996; Rane *et al.*, 2010) or the reduction of CoOOH (Li *et al.*, 2009). The two peaks in the TPR profile in the range between approximately 220°C and 500°C are typically attributed to the reduction of Co_3O_4 unperturbed by the support. The reduction peaks of Co_3O_4 are followed by H_2 consumption due to the interaction of cobalt with the support. A higher reduction temperature implies a stronger interaction between cobalt and support, with the reduction of cobalt aluminate (Rane *et al.*, 2010), cobalt silicate (Van Steen *et al.*, 1996), or cobalt titanate (Jongsomjit *et al.*, 2004) typically taking place at temperatures of approximately 800–1000°C.

The interaction of cobalt with the support results in a material that is more difficult to reduce. Hence, a higher reduction temperature is required to ensure a reasonable extent of reduction. However, a higher reduction temperature typically results in larger cobalt crystallites due to sintering (thus representing a loss in the catalytically active metal surface area). It is thus desired to keep the reduction temperature as low as possible, while obtaining a high degree of reduction.

Promotion of cobalt Fischer-Tropsch catalysts with noble metals

Noble metals such as Pt, Ru, or Au (but also Re) are added to the catalyst in small amounts, mainly to enhance the transformation of the cobalt oxide in the supported catalyst precursor to the catalytically active metallic phase (Schanke *et al.*, 1995). Figure 4 shows the effect of the addition of 0.5 wt% Pt to a 20 wt% $\text{Co}/\text{Al}_2\text{O}_3$ catalyst. All reduction processes are more facile, allowing a lower reduction temperature while obtaining a high degree of reduction.

Promotion with small amounts of Pt, typically around 0.1 wt%, has a significant effect on the extent of this reduction

when the reduction takes place isothermally. However, the effects observed depend on the applied reduction conditions and the catalyst used. Schanke *et al.* (1995) noted an increase in the extent of reduction from 48% to 77% with the addition of 0.4 wt% Pt to 9.0 wt% $\text{Co}/\text{Al}_2\text{O}_3$, but a much smaller increase (from 90% to 92%) with the addition of 0.4 wt% Pt to 8.9 wt% Co/SiO_2 . Tsubaki, Sun, and Fujimoto (2001) noted a larger increase in the degree of reduction from 50% to 56% upon promotion of a 10 wt% Co/SiO_2 catalyst with 0.2 wt% Pt. A similar increase for cobalt supported on silica was reported by Jacobs *et al.* (2002), with an increase in the degree of reduction from 64% to 72% when promoting a 15 wt% Co/SiO_2 catalyst with 3.8 wt% Pt (and an increase from 51% to 53% when promoting a 20 wt% $\text{Co}/\text{ZrO}_2\text{-SiO}_2$ catalyst with 0.5 wt% Pt).

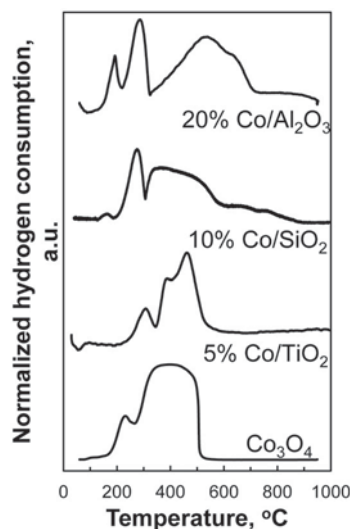


Figure 3—Normalized hydrogen consumption during temperature programmed reduction (TPR) of Co_3O_4 and supported cobalt catalysts (heating rate 10°C/min)

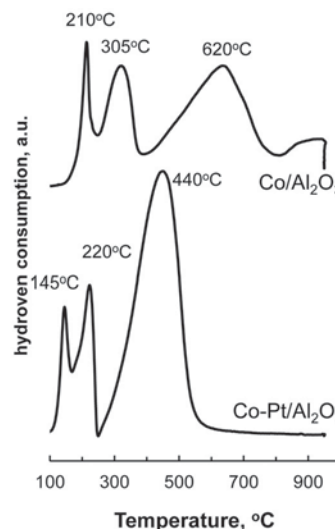


Figure 4—Normalized hydrogen consumption during temperature programmed reduction (TPR) of Co_3O_4 supported on alumina (20 wt% Co) and the catalyst co-impregnated with 0.5 wt% Pt

Technical and economic aspects of promotion of cobalt-based Fischer-Tropsch catalysts

A similar increase in the degree of reduction has been observed upon the addition of other noble metals to supported cobalt catalysts (Morales and Weckhuysen, 2006; Diehl and Khodakov, 2009; Hilmen, Schanke, and Holmen, 1996; Xu, *et al.*, 2008, 2005; Kogelbauer, Goodwin, and Oukaci, 1996; Jacobs *et al.*, 2009; Jalama *et al.*, 2007; McCue *et al.*, 2013). For instance, Jacobs *et al.* (2009) showed that promoting a 15 wt% Co/Al₂O₃ catalyst with Au resulted in a significant enhancement in the degree of reduction (see Table I). However, a Au loading of larger than 1.51 wt%, resulted in a decrease in the degree of reduction. A similar result was obtained by McCue *et al.* (2013).

Mechanism for enhanced reduction by noble metal promotion

It is commonly postulated that improved reducibility upon addition of noble metal promoters such as platinum occurs via hydrogen spillover from the promoter to the cobalt oxides (Diehl and Khodakov, 2009; Hilmen, Schanke, and Holmen, 1996; Jacobs *et al.*, 2004) (it should be noted that unequivocal evidence for this phenomenon is available only for Re-promoted cobalt catalysts (Hilmen, Schanke, and Holmen, 1996). Hydrogen spillover is defined as: the chemisorption of hydrogen molecules on metal surfaces to form adsorbed hydrogen species followed by their migration to another surface such as the support, (Roland, Braunschweig, and Roessner, 1997; Conradie, Gracia, and Niemantsverdriet, 2012). The driving force for hydrogen spillover is the difference in the energetic stability between adsorbed hydrogen on the metal and the adsorbed hydrogen on the support (Conradie, Gracia, and Niemantsverdriet, 2012). The energy levels associated with steps in the hydrogen spillover assisted reduction may be represented schematically by the dissociative adsorption of H₂ on the noble metal promoter, followed by the diffusion of atomic hydrogen on to the support and subsequently on to the reducible cobalt oxide (see Figure 5). The surface diffusion of adsorbed hydrogen species requires continually breaking and re-forming equivalent bonds with similar neighbouring atoms (Conner and Falconer, 1995) on the noble metal surface as well as the support surface. It has been observed that adsorbed species may travel over distances of up to several millimetres away from the dissociating metal surface (Conradie, Gracia, and Niemantsverdriet, 2012; Conner, and Falconer, 1995; Baeza *et al.*, 2006). The supply of dissociated (activated) hydrogen due to the presence of the noble metal in the catalyst by surface diffusion may facilitate the reduction of cobalt oxide, if the activation of hydrogen on cobalt oxide is kinetically the slow step in the reduction process.

The extent of surface diffusion depends not only on the noble metal present, but also on the support used. Baeza *et*

al. (2006) studied the extent of hydrogen spillover during hydrodesulphurization and observed that the extent of hydrogen spillover was: $\gamma\text{-Al}_2\text{O}_3 < \text{C} < \text{SiO}_2 < \text{MgSiO}_3$. This trend mimics the extent of surface 'acidity' or presence of OH groups. On oxidic surfaces such as Al₂O₃, spillover of hydrogen is commonly thought to occur via formation of 'hydroxyls' (Conradie, Gracia, and Niemantsverdriet, 2012). According to Luo and Epling (2010), the energetics of hydrogen transportation via continual formation and breakage of adjacent hydroxyl groups on an Al₂O₃ surface are quite high and slow because the spillover hydrogen first has to bond to a surface oxygen atom to form a hydroxyl group. The surface hydroxyls formed then act as a 'bucket brigade' with which subsequent spillover H species interact weakly as they are transported over the Al₂O₃ surface (see Figure 6). The bucket-brigade phenomenon can also be used to explain why the range of hydrogen spillover is reduced when catalysts are exposed to high temperature, because surface hydroxyls start to desorb, making spillover energetically less favourable.

It should, however, be realized that the reduction process of supported cobalt catalysts may be more complex than outlined above. The strong increase in the degree of reduction typically reported upon addition of the noble metal as a reduction promoter cannot be explained only by the enhanced rate of reduction of cobalt oxide crystallites present in the catalyst precursor. Cobalt in the supported cobalt catalyst prepared via impregnation may also contain highly dispersed cobalt (e.g. cobalt atomically dispersed over the support) in addition to cobalt-containing crystallites. This cobalt will be

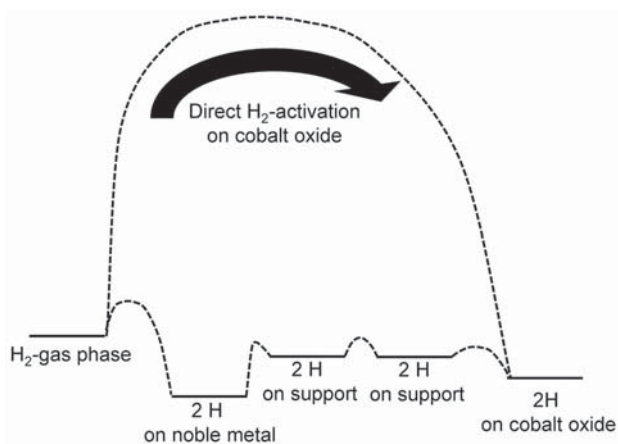


Figure 5—Schematic representation of the energy levels required to facilitate the reduction of cobalt oxide due to the presence of a noble metal promoter

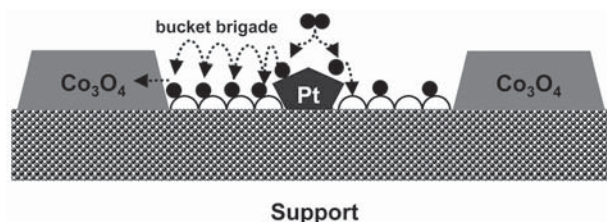


Figure 6—Illustration of hydrogen spillover transport assisted by OH group formation on Al₂O₃ giving rise to a 'bucket brigade' (Luo and Epling, 2010)

Table I

Effect of promotion with Au on the cobalt reducibility in 15 wt-% Co/Al₂O₃ (Jacobs *et al.* 2009)

Au-loading, wt.-%	0	0.1	1.51	5.05
Reduction of Cobalt (%)	49.8	58.9	94.1	81.5

Technical and economic aspects of promotion of cobalt-based Fischer-Tropsch catalysts

difficult to reduce. The supply of hydrogen to the support may result in the formation of mobile cobalt species, which may diffuse to larger cobalt crystallites. The slow reduction of this type of cobalt species on the support may account for the observed increase in the degree of reduction of the industrial cobalt Fischer-Tropsch catalysts during Fischer-Tropsch synthesis (Van de Loosdrecht *et al.*, 2007).

It is currently unclear where the noble metal promoter is positioned after the reduction process. Platinum and ruthenium seem to be incorporated into the oxidic cobalt in the catalyst precursor and in the cobalt metal after reduction (Weststrate, Saib, and Niemantsverdriet, 2013). Promotion with group 11 metals seems to lead to segregation between metallic cobalt particles and metallic group 11 particles (Ma *et al.*, 2012).

Change in cobalt dispersion due to noble metal addition

The preparation method may also result in a close proximity of the cobalt oxide phase and the noble metal (salt). It has been noted that the promotion of cobalt-based catalysts does affect the dispersion of cobalt particles in cobalt Fischer-Tropsch catalysts (Schanke, *et al.*, 1995; Tsubaki, Sun, and Fujimoto, 2001; Jacobs *et al.*, 2002) (see Table II). The increase in dispersion upon addition of noble metal promoter has been attributed to a higher concentration of cobalt oxide nucleation and crystallization sites (Khodakov, 2009). A higher number of sites will result in a larger number of crystallites and hence a smaller average particle size and larger percentage dispersion.

The enhanced cobalt dispersion may be beneficial for cobalt-based Fischer-Tropsch catalysts, since the number of exposed metal atoms will increase more rapidly than by an increase in the degree of reduction. However, an enhanced dispersion in addition to an enhanced degree of reduction will not necessarily lead to an increase in the catalytic activity, since the turnover frequency depends on the dispersion as well (see Figure 2).

Change in catalytic behaviour due to noble metal addition

An increase in the degree of reduction (in conjunction with an increase in the cobalt dispersion) may, but does not necessarily, result in an increase in the catalytic activity.

Table III summarizes some of the obtained activities and selectivities upon promoting a Co/ γ -Al₂O₃ Fischer-Tropsch catalyst with various noble metals as reported by Jacobs *et al.* (2009); Ma *et al.* (2012). The activity is given as the rate of CO conversion per surface atom as determined by H₂ desorption on the freshly reduced catalyst (reduction in hydrogen at atmospheric pressure and 350°C for 10 h) in order to assess whether the promoter elements affect the intrinsic activity of the catalyst (i.e. enhance the catalyst activity beyond the change in dispersion and the change in the degree of reduction). This comparison is non-trivial since the catalyst undergoes further changes during the Fischer-Tropsch synthesis (viz. further reduction and deactivation (Van de Loosdrecht *et al.*, 2007). The further reduction may have a significant effect on the turnover frequency of, in particular, the unpromoted cobalt catalysts, and these turnover frequencies are much higher than those typically obtained for impregnated catalysts (Van Steen and Claeys, 2008). Nevertheless, a tentative comparison of the intrinsic activity of the various promoter elements can be made, which starts mostly at a degree of reduction of approximately 70%.

Copper, the typical reduction promoter for iron-based Fischer-Tropsch catalysts, which would be the cheapest reduction promoter, yields an increase in the degree of reduction, but a decrease in the catalytic activity (Jacobs *et al.*, 2009; Baker, Burch, and Yuqin, 1991), despite the observed increase in the cobalt dispersion. This can be ascribed to blockage of the active metallic cobalt surface with copper. Surface enrichment or blockage with copper can be expected if copper is associated with metallic cobalt, since the surface energy of copper is much lower than that of cobalt (Swart, Van Helden, and Van Steen, 2007). A similar surface blockage effect could have been expected for silver, gold, and to a lesser extent palladium, if these metals are associated with metallic cobalt in the reduced catalyst.

Other noble metals have a higher surface energy than metallic cobalt (Vitos *et al.*, 1998), and surface enrichment with these metals is therefore not expected. The addition of platinum was originally thought to increase the intrinsic activity as well as the degree of reduction (Schanke *et al.*, 1995), but tests under more realistic Fischer-Tropsch conditions (Vada *et al.*, 1995; Jacobs *et al.*, 2002) do not seem to show an enhancement of the intrinsic activity. However, Xu *et al.* (2005) reported an enhancement of the catalytic activity due to a catalytic synergistic effect between

Table II

Effect of noble metal addition on cobalt dispersion

Catalyst	D _{Co} , unpromoted, %	Promoter	D _{Co} , promoted, %	Ref.
9 wt% Co/SiO ₂	7.5	0.4 wt.-% Pt	9.6	Schanke <i>et al.</i> , 1995
10 wt% Co/SiO ₂	8.6	0.2 wt.-% Pt	22.7	Tsubaki, Sun, and Fujimoto, 2001
15 wt% Co/SiO ₂	2.1	3.8 wt.-% Pt	2.7	Jacobs <i>et al.</i> , 2002
15 wt% Co/Al ₂ O ₃	17.5	0.5 wt.-% Pt	18.4	Jacobs <i>et al.</i> , 2002
25 wt% Co/Al ₂ O ₃	8.7	0.5 wt.-% Pt	9.4	Jacobs <i>et al.</i> , 2002
15 wt% Co/Al ₂ O ₃	11.4	0.1 wt.-% Au	12.6	Jacobs <i>et al.</i> , 2009
		1.5 wt.-% Au	15.3	
		5.1 wt.-% Au	16.0	

Technical and economic aspects of promotion of cobalt-based Fischer-Tropsch catalysts

Table III

Physical characteristics (DOR: degree of reduction of cobalt; D_{Co} : corrected dispersion of cobalt), activity (expressed as turnover frequency for CO conversion as determined from the space velocity to obtain $X_{CO} = 50\%$ after approximately 100 h on line relative to the amount of H_2 desorbed on the freshly reduced catalyst) and selectivity for the formation of methane (S_{CH_4}) and for the formation of liquid hydrocarbons ($S_{C_{5+}}$) of some noble metal promoted cobalt catalysts

Mn	25	Fe	26	Co	27	Ni	28	Cu	29
					[a] [b]				
				DOR, %	54.5 49.8			wt.-% [b]	0.49
				D_{Co} , %	5.5 11.4			DOR, %	69.4
				TOF, min^{-1}	4.0 1.6			D_{Co} , %	15.2
				S_{CH_4} , C-%	7.9 8.9			TOF, min^{-1}	0.8
				$S_{C_{5+}}$, C-%	83.4 80.6			S_{CH_4} , C-%	9.9
								$S_{C_{5+}}$, C-%	76.6
Tc	43	Ru	44	Rh	45	Pd	46	Ag	47
		wt.-% [a]	0.26			wt.-% [a]	0.27	wt.-% [b]	0.49
		DOR, %	70.7			DOR, %	72.1	DOR, %	69.4
		D_{Co} , %	9.3			D_{Co} , %	8.1	D_{Co} , %	15.2
		TOF, min^{-1}	2.4			TOF, min^{-1}	1.4	TOF, min^{-1}	1.3
		S_{CH_4} , C-%	7.7			S_{CH_4} , C-%	12.6	S_{CH_4} , C-%	8.5
		$S_{C_{5+}}$, C-%	85.2			$S_{C_{5+}}$, C-%	73.8	$S_{C_{5+}}$, C-%	81.5
Re	75	Os	76	Ir	77	Pt	78	Au	79
wt.-% [a]	0.48					wt.-% [a]	0.5	wt.-% [b]	1.51
DOR, %	67.2					DOR, %	68.4	DOR, %	94.1
D_{Co} , %	10.1					D_{Co} , %	8.3	D_{Co} , %	15.3
TOF, min^{-1}	2.94					TOF, min^{-1}	1.5	TOF, min^{-1}	1.0
S_{CH_4} , C-%	7.0					S_{CH_4} , C-%	8.3	S_{CH_4} , C-%	8.7
$S_{C_{5+}}$, C-%	86.2					$S_{C_{5+}}$, C-%	83.2	$S_{C_{5+}}$, C-%	82.0

[a] Catalyst contains 25% Co on $\gamma-Al_2O_3$ and the Fischer-Tropsch synthesis was performed at 493 K, 2.2 MPa, $(H_2/CO)_{inlet} = 2.1$ (Ma *et al.* 2012)

[b] Catalyst contains 15% Co on $\gamma-Al_2O_3$ and the Fischer-Tropsch synthesis was performed at 493 K, 2.0 MPa, $(H_2/CO)_{inlet} = 2.1$ (Jacobs *et al.* 2009)

cobalt and noble metals, which resulted in an increased reactivity of the adsorbed carbon monoxide. Induced electronic effects by the promoter may result in electronic donation or withdrawal, which may lead to an increased intrinsic turnover frequency or a change in product selectivity (Morales and Weckhuysen, 2006). This may be attributed to the high promoter loading, when the noble metal and metallic cobalt form a single particle. At relative low loadings of industrial interest (*vide verde*), the synergistic effect is expected to diminish. Addition of low amounts of ruthenium increase the site time yield, which is ascribed to a reduced deactivation of the catalyst (Jacobs *et al.*, 2002) (this could not be confirmed with Co/Al_2O_3 (Kogelbauer, Goodwin, and Oukaci, 1996; Vada *et al.*, 1995; Hosseini *et al.*, 2004)). Rhenium shows a high turnover frequency (Ma *et al.*, 2012), although it was previously thought not to affect the intrinsic activity of the resulting metallic cobalt crystallites (Vada *et al.*, 1995; Barkhuizen *et al.*, 2006).

The selectivity towards the desired products, typically expressed as the conversion of CO to C_{5+} hydrocarbons, is of prime importance in the conversion of CO to liquid hydrocarbons. It can be seen from Table III that, in particular, the addition of Pd and Cu at the tested levels results in a decrease in the selectivity for the desired products (and concomitantly an increase in the selectivity for the undesired methane).

Economic outlook for noble metal additions to cobalt Fischer-Tropsch catalysts

The Fischer-Tropsch synthesis is nowadays still a relative

small process with a total world-wide capacity on the industrial scale of approximately 363 000 bbl per day. The total amount of liquid fuels produced using cobalt-based catalyst will be approximately 193 000 bbl per day in 2014. The required amount of cobalt can thus be estimated using the typically quoted turnover frequency of $0.01 s^{-1}$ (Van Steen and Claeys, 2008) (see Figure 7). A Fischer-Tropsch plant producing 100 000 bbl per day of liquid products (amounting to the capacity of a single small oil refinery) would then require 646 t of cobalt (taking into account a dispersion of 12%, average crystallite size of the cobalt metal of 8 nm, and a degree of reduction of 80% (Luo and Epling, 2010) or approximately 1% of annual cobalt production (Diehl, and Khodakov, 2009).

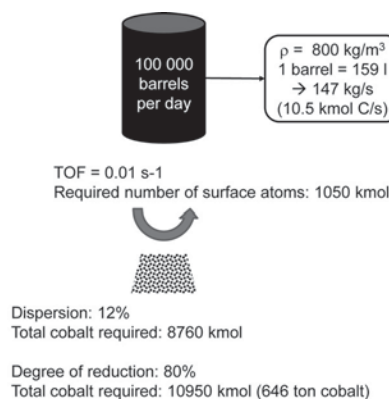


Figure 7—Amount of cobalt required to produce 100 000 bbl per day of liquid hydrocarbons using the Fischer-Tropsch process

Technical and economic aspects of promotion of cobalt-based Fischer-Tropsch catalysts

The choice of metal utilized as the noble metal promoter in cobalt-based Fischer-Tropsch catalysts depends on the amount of noble metal required, its effect, its current price, and the effect of the newly added market on the price of the metal. The latter is difficult to establish, but might be anticipated comparing the required amount of the noble metal to its annual production (see Table IV).

The effectiveness of the noble metal promoters depends on the level of the promotion (Jacobs *et al.*, 2009). However, it should be realized that most academic studies are performed to show the effect of the noble metal promoter, and the amount of promoter may be higher than required. For instance, the comparison of the effect of different noble metals by the group of Davis (Jacobs *et al.*, 2009; Ma *et al.*, 2012) utilized 0.5 wt% Pt for a catalyst containing 25 wt% cobalt. The commercial catalyst seems to have a lower platinum loading of approximately 0.05 wt% Pt with a cobalt loading of 20 wt% (Ma *et al.*, 2012). This affects the required amount of the noble metal significantly.

The reported levels for the use of rhenium are high (0.02–0.04 g Re per gram Co), implying a high demand on rhenium if this promoter is to be used on a large scale. Furthermore, the large amount of rhenium used in the catalyst implies that a large amount of capital will be locked up in the reactor (assuming that rhenium itself does not contribute to the Fischer-Tropsch synthesis – *vide supra*). Worldwide rhenium production is low, and the amount of rhenium required corresponds to 33–57% of annual production. Hence, the introduction of rhenium on a large scale in Fischer-Tropsch catalysts may result in large fluctuations in the rhenium price.

Ruthenium as a promoter is quite attractive (Xu *et al.*, 2008; Kogelbauer, Goodwin, and Oukaci, 1996; Ma *et al.*, 2012; Iglesia *et al.*, 1993; Hosseini *et al.*, 2004), certainly at the anticipated level of 0.1 g Ru per gram Co (this value may even be further reduced). The evaluation of ruthenium as a promoter is somewhat complicated, since ruthenium itself shows activity for Fischer-Tropsch synthesis (Bertole, Mims, and Kiss 2004). The low price of ruthenium will result in a relative low amount of capital being locked up in the reactor. However, the low annual worldwide production of ruthenium will result in a volatile price if this metal is used on a large scale in Fischer-Tropsch catalysts.

Platinum is currently used as a noble metal promoter in an industrial cobalt-based Fischer-Tropsch catalyst. The typical platinum content seems to be 0.003 g Pt per gram Co (Van de Loosdrecht *et al.*, 2007) (significantly lower than used by Ma *et al.*, (2012). The amount of platinum to be used in a 100 000 barrel per day Fischer-Tropsch plant is expected to be in the range of 1% of the annual worldwide production. A concern from an economic viewpoint is the large amount of capital that is locked up in the reactor.

Gold as a noble metal promoter can enhance the degree of reduction (Jacobs *et al.*, 2009), but the typically tested levels are too high to be of economic use. The high price of gold in conjunction with the required level of promotion results in a large amount of capital being locked up in the process, making the conversion of carbon-containing feedstock into liquid hydrocarbons economically not feasible.

The primary role of the noble metals added to cobalt-based Fischer-Tropsch catalysts is to increase the degree of reduction of cobalt in supported catalysts, while at the same time yielding high cobalt dispersion. Noble metals were introduced in the catalyst at a time when the price of cobalt was relatively high (approximately 200 times the price of iron, whereas it is nowadays approximately 70 times the price of iron). Hence, it might be argued that the need for noble metal promoters has diminished. However, the drive nowadays is to increase reactor yields, which must be achieved by having catalysts containing a high level of metallic cobalt per unit mass of catalyst. This can be achieved by addition of (low levels of) noble metal promoters or changing the catalyst preparation route (Fischer *et al.*, 2012).

Concluding remarks

Noble metals are added to the cobalt-based Fischer-Tropsch catalyst primarily to facilitate the reduction of oxidic cobalt in the impregnated, supported catalyst precursor. The enhancement in reduction is attributed mainly to H₂ spillover due to the presence of reduced metal facilitating the production of dissociated hydrogen, which may diffuse over the support to oxidic cobalt moieties. The increased degree of reduction (with the often observed change in dispersion) results in an improved catalyst activity. The catalyst activity may be further enhanced through a synergistic effect between the noble metal and the catalytically active metallic cobalt.

Table IV

Market aspects of the utilization of noble metals as a promoters in cobalt-based Fischer-Tropsch catalysts to produce 100 000 barrels of liquid per day (assuming TOF = 0.01 s⁻¹, D_{Co} = 12%, DOR = 80%)

Promoter	Promoter level, g per gram Co	Required ¹ , t	Price ² , 106 US\$	Relative usage ³ , %
Re	0.042 [30]	26.9	94.1	57
0.019 [58]	15.5	54.2	33	
Ru	0.010 [58]	6.7	16.2	56
Pt	0.020 [58]	12.9	590.5	7
0.003 [53]	1.6	73.8	1	
Au	0.100 [44]	65.0	2798	3

¹Required tonnage of the noble metal to add to 646 t of cobalt

²Cost of the noble metal adding to 646 t of cobalt in 2013 (Re: US\$ 3500/kg; Ru: US\$ 2410/kg; Pt: US\$ 45730/kg; Au: US\$ 43050/kg)

³The amount of noble metal to be added to 646 t of cobalt relative to the annual production of the noble metal in 2012 (Re: 47.2 t; Ru: 75 t; Pt: 192 t; Au: 2350 t)

Technical and economic aspects of promotion of cobalt-based Fischer-Tropsch catalysts

The levels of promotion of most metals as currently reported in the open literature seem too high for commercial operation, and a decrease in the level of the noble metal promoter is desired, for which a more detailed understanding on the effect of the loading of the noble metal promoter is required.

References

- ANDERSON, R.B. 1956. Hydrocarbon synthesis, hydrogenation and cyclization. *Catalysis*. Emmet, P.H. (ed.). vol. IV, Reinhold, New York.
- BAEZA, P., VILLARROEL, M., AVILA, P., AGUDO, L.A., DELMON, B., and GIL-LLAMBIAS, F.J. 2006. Spillover hydrogen mobility during Co-Mo catalyzed HDS in industrial-like conditions. *Applied Catalysis A: General*, vol. 304. pp. 109–115.
- BAKER, J.E., BURCH, R., and YUQIN, N. 1991. Investigation of CoAl₂O₄, Cu/CoAl₂O₄ and Co/CoAl₂O₄ catalysts for the formation of oxygenates from carbon monoxide – carbon dioxide – hydrogen mixture. *Applied Catalysis*, vol. 73. pp. 135–152.
- BARBIER, A., TUEL, A., ARCON, I., KODRE, A., and MARTIN, G.A. 2001. Characterization and catalytic behaviour of Co/SiO₂ catalysts: Influence of dispersion in the Fischer-Tropsch reaction. *Journal of Catalysis*, vol. 200. pp. 106–116.
- BARKHUIZEN, D., MABASO, I., VIJJOEN, E., WELKER, C., CLAEYS, M., NAN STEEN, E., and FLETCHER, J.C.Q. 2006. Experimental approaches to the preparation of supported metal nanoparticles. *Pure and Applied Chemistry*, vol. 78. pp. 1759–1769.
- VAN BERGE, P.J. and EVERSON, R.C. 1997. Cobalt as an alternative Fischer-Tropsch catalyst to iron for the production of middle distillates. *Studies in Surface Science and Catalysis*, vol. 107. pp. 207–212.
- BERTOLE, C.J., MIMS, C.A., and KISS, G. 2004. Support and rhenium effects on the intrinsic site activity and methane selectivity of cobalt Fischer-Tropsch catalysts. *Journal of Catalysis*, vol. 221. pp. 191–203.
- BEZEMER, G.L., BITTER, J.H., KUIJPERS, H.P.C.E., OOSTERBEEK, H., HOLEWIJN, J.E., XU, Z., KAPTEJN, F., VAN DILLEN, A.J., and DE JONG, K.P. 2006. Cobalt particle size effects in the Fischer-Tropsch reaction studied with carbon nanofiber supported catalysts. *Journal of the American Chemical Society*, vol. 128. pp. 3956–3964.
- BORG, Ø., ERI, S., BLEKKAN, E.A., STORSÆTER, S., WIGUM, H., RYTTER, E., and HOLMEN, A. 2007. Fischer-Tropsch synthesis over γ -alumina-supported cobalt catalysts: effect of support variables. *Journal of Catalysis*, vol. 248. pp. 89–100.
- BOTES, F.G., NIEMANTSVERDRIET, J.W., and VAN DE LOOSDRECHT, J. 2013 A comparison of cobalt and iron based slurry phase Fischer-Tropsch synthesis. *Catalysis Today*, vol. 215. pp.112–120. <http://dx.doi.org/10.1016/j.cattod.2013.01.013>
- CLAEYS, M. and VAN STEEN, E. 2004. Fischer-Tropsch synthesis: basic studies. *Studies in Surface Science and Catalysis*, vol. 152. pp. 601–680.
- CONNER, W.C. JR. and FALCONER, J.L. 1995. Spillover in heterogeneous catalysis. *Chemical Reviews*, vol. 95. pp. 759–788.
- CONRADIE, J., GRACIA, J., and NIEMANTSVERDRIET, J.W. 2012. Energetic driving force of H spillover between rhodium and titania surfaces: a DFT view. *Journal of Physical Chemistry C*, vol. 116. pp. 25362–25367.
- DEN BREEJEN, J.P., SIETSMA, J.R.A., FRIEDRICH, H., BITTER, J.H., and DE JONG, K.P. 2010. Design of supported cobalt catalysts with maximum activity for the Fischer-Tropsch synthesis. *Journal of Catalysis*, vol. 270. pp. 146–152.
- DIEHL, F. and KHODAKOV, A.Y. 2009. Promotion of cobalt Fischer-Tropsch catalysts with noble metals: a review. *Oil and Gas Science and Technology – Review IFP*, vol. 64. pp. 11–24.
- FELLER, A., CLAEYS, M., and VAN STEEN, E. 1999. Cobalt cluster effects in zirconium promoted Co/SiO₂ Fischer-Tropsch catalysts. *Journal of Catalysis*, vol. 185. pp. 120–130.
- FISCHER, N., VAN STEEN, E., and CLAEYS, M. 2013. Structure sensitivity of the Fischer-Tropsch activity and selectivity on alumina supported catalysts. *Journal of Catalysis*, vol. 299. pp. 67–80.
- FISCHER, N., MINNERMANN, M., BAEUMER, M., VAN STEEN, E., and CLAEYS, M. 2012. Metal support interactions in Co₃O₄/Al₂O₃ catalysts prepared from w/o microemulsions. *Catalysis Letters*, vol. 142. pp. 830–837.
- HAUMAN, M.M., SAIB, A., MOODLEY, D.J., DU PLESSIS, E., CLAEYS, M., and VAN STEEN, E. 2012. Re-dispersion of cobalt on a model Fischer-Tropsch catalyst during reduction-oxidation-reduction cycles. *ChemCatChem*, no. 4. pp. 1411–1419.
- HEWU, W., HAN, H., XIHAO, L., KE, Z., and MINGGAO, Q. 2009. Performance of Euro III common rail heavy duty diesel engine fuelled with Gas to Liquid. *Applied Energy*, vol. 86. pp. 2257–2261.
- HILMEN, A.M., SCHANKE, D., and HOLMEN, A. 1996. TPR study of the mechanism of rhenium promotion of alumina supported cobalt Fischer-Tropsch catalysts. *Catalysis Letters*, vol. 38. pp. 143–147.
- HOSSEINI, S.A., TAEB, A., FEYZI, F., and YARIPOUR, F. 2004. Fischer-Tropsch synthesis over Ru-promoted Co/ γ -Al₂O₃ catalysts in a CSTR. *Catalysis Communications*, vol. 5. pp. 137–143.
- HUANG, Y., WANG, S., and ZHOU, L. 2008. Effects of Fischer-Tropsch diesel fuel on combustion and emissions of direct injection diesel engine. *Frontiers of Energy and Power Engineering in China*, vol. 2. pp. 261–267.
- IGLESIA, E. 1997. Design, synthesis and use of cobalt-based Fischer-Tropsch synthesis catalysts. *Applied Catalysis A: General*, vol. 161. pp. 59–78.
- IGLESIA, E., SOLED, S.L., FIATO, R.A., and VIA, G.H. 1993. Bimetallic synergy in cobalt ruthenium Fischer-Tropsch catalysts. *Journal of Catalysis*, vol. 143. pp. 345–368.
- JACOBS, G., RIBEIRO, M.C., MA, W., JI, Y., KHALID, S., SUMODJO, P.T.A., and DAVIS, B.H. 2009. Group 11 (Cu, Ag, Au) promotion of 15%Co/Al₂O₃ Fischer-Tropsch synthesis catalysts. *Applied Catalysis A: General*, vol. 361. pp. 137–151.
- JACOBS, G., CHANEY, J.A., PATTERSON, P.M., DAS, T.K., MAILLOT, J.C., and DAVIS, B.H. 2004. Fischer-Tropsch synthesis: study of the promotion of Pt on the reduction property of Co/Al₂O₃ catalysts by in situ EXAFS of Co K and Pt L_{III} edges and XPS. *Journal of Synchrotron Radiation*, vol. 11. pp. 414–422.
- JACOBS, G., PATTERSON, P.M., ZHANG, Y., DAS, T., LI, J., and DAVIS, B.H. 2002. Fischer-Tropsch synthesis: deactivation of noble metal-promoted Co/Al₂O₃ catalysts. *Applied Catalysis A: General*, vol. 233. pp. 215–226.
- JACOBS, G., DAS, T.K., ZHANG, Y., LI, J., RACOLLET, G., and DAVIS, B.H. 2002. Fischer-Tropsch synthesis: support, loading, and promoter effects on the reducibility of cobalt catalysts. *Applied Catalysis A: General*, vol. 233. pp. 263–281.
- JALAMA, K., COVILLE, N.J., HILDEBRANDT, D., GLASSER, D., JEWELL, L.L., ANDERSON, J.A., TAYLOR, S., ENACHE, D., and HUTCHINGS, G.J. 2007. Effect of the addition of Au on Co/TiO₂ catalyst for the Fischer-Tropsch reaction. *Topics in Catalysis*, vol. 44. pp. 129–136.
- JONGSOMJIT, B., SAKDAMNUSON, C., GOODWIN, J.G., and PRASERTHDAM, R. 2004. Co-support compound formation in titania-supported cobalt catalysts. *Catalysis Letters*, vol. 94. pp. 209–215.

Technical and economic aspects of promotion of cobalt-based Fischer-Tropsch catalysts

- KHODAKOV, A.Y. 2009. Fischer-Tropsch synthesis: relations between structure of cobalt catalysts and their catalytic performance. *Catalysis Today*, vol. 144. pp. 251–257.
- KHODAKOV, A.Y., GRIBOVAL-CONSTANT, A., BECHARA, R., and VILLAIN, F. 2001. Pore size control of cobalt dispersion and reducibility in mesoporous silicas. *Journal of Physical Chemistry B*, vol. 105. pp. 9805–9811.
- KHODAKOV, A.Y., CHU, W., and FONGARLAND, P. 2007. Advances in the development of novel cobalt Fischer-Tropsch catalysts for synthesis of long chain hydrocarbons and clean fuels. *Chemical Reviews*, vol. 107. pp. 1692–1744.
- KNOTTENBELT, C. 2002. Mossgas 'gas-to-liquid' diesel fuels—an environmentally friendly option. *Catalysis Today*, vol. 71. pp. 437–445.
- KOGELBAUER, A., GOODWIN, J.G., and OUKACI, R. 1996. Ruthenium promotion of Co/Al₂O₃ Fischer-Tropsch catalysts. *Journal of Catalysis*, vol. 160. pp. 125–133.
- LAMPRECHT, D., DANQUART, L.P., and HARRILLALL, K. 2007. Performance synergies between low-temperature and high-temperature Fischer-Tropsch diesel blends. *Energy & Fuels*, vol. 21. pp. 2846–2852.
- LECKEL, D. 2011. Diesel production in coal-based high-temperature Fischer-Tropsch plants using fixed bed dry bottom gasification technology. *Fuel Processing Technology*, vol. 92. pp. 959–969.
- LI, Y., ZHAO, Z., DUAN, A., JIANG, G., and LIU, J. 2009. Comparative study on the formation and reduction of bulk and Al₂O₃-supported cobalt oxides by H₂-TPR technique. *Journal of Physical Chemistry C*, vol. 113. pp. 7186–7199.
- LUO, J.-Y. AND EPLING, W.S. 2010. New insights into the promoting effect of H₂O on a model Pt/Ba/Al₂O₃ NSR catalyst, vol. 97. pp. 236–247.
- MA, W., JACOBS, G., KEOGH, R.A., BUKUR, D.B., and DAVIS, B.H. 2012. Fischer-Tropsch synthesis: effect of Pd, Pt, Re, and Ru noble metal promoters on the activity and selectivity of a 25%Co/Al₂O₃ catalyst. *Applied Catalysis A: General*, vol. 437–438. pp. 1–9.
- MA, W., JACOBS, G., LI, Y., BHATELIA, T., BUKUR, D.B., KHALID, S., and DAVIS, B.H. 2011. Fischer-Tropsch synthesis: influence of CO-conversion on selectivities, H₂/CO usage ratios, and catalyst stability for a Ru promoted Co/Al₂O₃ catalyst using a slurry reactor. *Topics in Catalysis*, vol. 54. pp. 757–767.
- MARTÍNEZ, A. and PRIETO, G. 2007. Breaking the dispersion-reducibility dependence in oxide supported cobalt nanoparticles. *Journal of Catalysis*, vol. 245. pp. 470–476.
- MCCUE, A.J., APONAVICIUTE, J., WELLS, R.P.K., and ANDERSON, J.A. 2013. Gold modified cobalt-based Fischer-Tropsch catalysts for conversion of synthesis gas to liquid fuels. *Frontiers of Chemical Science and Engineering*, vol. 7, no. 3. pp. 1–8.
- MORALES, F. and WECKHUYSEN, B.M. 2006. Promotion effects in Co-based Fischer-Tropsch catalysis. *Catalysis*, vol. 19. pp. 1–40.
- PATTERSON, P.M., DAS, T.K., and DAVIS, B.H. 2003. Carbon monoxide hydrogenation over molybdenum and tungsten carbides. *Applied Catalysis A: General*, vol. 251. pp. 449–455.
- RANE, S., BORG, Ø., YANG, J., RYTTER, E., and HOLMEN, A. 2010. Effect of alumina phases on hydrocarbon selectivity in Fischer-Tropsch synthesis. *Applied Catalysis A: General*, vol. 388. pp. 160.
- RANHOTRA, G.S., BELL, A.T., and REIMER, J.A. 1987. Catalysis over molybdenum carbides and nitrides: II. Studies of CO hydrogenation and C₂H₆ hydrogenolysis. *Journal of Catalysis*, vol. 108. pp. 40–49.
- ROLAND U., BRAUNSCHWEIG, T., and ROESSNER, F. 1997. On the nature of spilt-over hydrogen. *Journal of Molecular Catalysis A: Chemical*, vol. 127. pp. 61–84.
- SAIB, A.M., CLAEYS, M., and VAN STEEN, E. 2002. Silica supported cobalt Fischer-Tropsch catalysts: effect of pore diameter of support. *Catalysis Today*, vol. 71. pp. 395–402.
- VAN SANTEN, R.A., CIOBICA, I.M., VAN STEEN, E., and GHOURI, M.M. 2011. Mechanistic issues in Fischer-Tropsch catalysis. *Advances in Catalysis*, no. 54. pp. 127–187.
- SCHANKE, D., VADA, S., BLEKKAN, E.A., HILMEN, A.M., HOFF, A., and HOLMEN, A. 1995. Study of Pt-promoted cobalt CO hydrogenation catalysts. *Journal of Catalysis*, vol. 156. pp. 85–95.
- SCHULZ, H. 1985. Selectivity and mechanism of the Fischer-Tropsch CO-hydrogenation. *C1 Molecular Chemistry*, vol. 1. p. 231.
- VAN STEEN, E. and CLAEYS, M. 2008. Fischer-Tropsch catalysts for the Biomass-to-Liquid (BTL)-process. *Chemical Engineering and Technology*, vol. 31, no. 5. pp. 655–666.
- STORSÆTER, S., TØTDAL, B., WALMSLEY, J.C., TANEM, B.S., and HOLMEN, A. 2005. Characterization of alumina-, silica-, and titania-supported cobalt Fischer-Tropsch catalysts. *Journal of Catalysis*, vol. 236. pp. 139–152.
- SWART, J.C.W., VAN HELDEN, P., and VAN STEEN, E. 2007. Surface energy estimation of catalytically relevant fcc transition metals using DFT-calculations on nano-rods. *Journal of Physical Chemistry C*, vol. 111. pp. 4998–5005.
- TSUBAKI, N., SUN, S., and FUJIMOTO, K. 2001. Different functions of the noble metals added to cobalt catalysts for Fischer-Tropsch synthesis. *Journal of Catalysis*, vol. 199. pp. 236–246.
- VADA, S., HOFF, A., ADNANES, E., SCHANKE, D., and HOLMEN, A. 1995. Fischer-Tropsch synthesis on supported cobalt catalysts promoted by platinum and rhenium. *Topics in Catalysis*, vol. 2. pp. 155–162.
- VADA, S., HOFF, A., ADNANES, E., SCHANKE, D., and HOLMEN, A. 1995. Fischer-Tropsch synthesis on supported cobalt catalysts promoted by platinum and rhenium. *Topics in Catalysis*, vol. 2. pp. 155–162.
- VAN DE LOOSDRECHT, J., BALZHINIMAEV, B., DALMON, J.-A., NIEMANTSVERDIET, J.W., TSYBULYA, S.V., SAIB, A.M., VAN BERGE, P.J., and VISAGIE, J.L. 2007. Cobalt Fischer-Tropsch synthesis: deactivation by oxidation? *Catalysis Today*, vol. 123. pp. 293–302.
- VAN STEEN, E., SEWELL, G.S., MAKHOTE, R.A., MICKLETHWAITE, C., MANSTEIN, H., DE LANGE, M., and O'CONNOR, C.T. 1996. TPR study on the preparation of impregnated Co/SiO₂ catalysts. *Journal of Catalysis*, vol. 162. pp. 220–230.
- VANNICE, M.A. 1975. The catalytic synthesis of hydrocarbons from H₂/CO mixtures over the group VIII metals. I The specific activity and product distributions of supported metals. *Journal of Catalysis*, vol. 37. pp. 449–461.
- VANNICE, M.A. 1977. The catalytic synthesis of hydrocarbons from H₂/CO mixtures over the group VIII metals. V. The catalytic behaviour of silica-supported metals. *Journal of Catalysis*, vol. 50. pp. 228–236.
- VITOS, L., RUBAN, A.V., SKRIVER, H.L., and KOLLAR, J. 1998. The surface energy of metals. *Surface Science*, vol. 411. pp. 186–202.
- WESTSTRATE, C.J., SAIB, A., and NIEMANTSVERDIET, J.W. 2013. Promoter segregation in Pt and Ru promoted cobalt model catalysts during oxidation-reduction treatments. *Catalysis Today*, vol. 215, no. 15. pp. 2–7. <http://dx.doi.org/10.1016/j.cattod.2013.01.009>
- XU, D., DAI, P., GUO, Q., and LI, W. 2008. Promotional effects of noble metal addition to cobalt Fischer-Tropsch catalysts. *Reaction Kinetics and Catalysis Letters*, vol. 94. pp. 367–374.
- XU, D., LI, W., DUAN, H., GE, Q., and XU, H. 2005. Reaction performance and characterization of Co/Al₂O₃ Fischer-Tropsch catalysts promoted with Pt, Pd and Ru. *Catalysis Letters*, vol. 102. pp. 229–235. ◆



COLLISION WARNING SYSTEMS

INTRINSICALLY SAFE SOLUTIONS

INDUSTRIAL NETWORKING, TELEMETRY, MONITORING AND CONTROL SOLUTIONS

ENVIRONMENTAL SENSING INSTRUMENTS

ASSET MANAGEMENT AND SOLUTIONS



THE MINING INDUSTRY TRUSTS BOOYCO ELECTRONICS TO PUT IT ALL TOGETHER!

0861 BOOYCO (0861 266926)

+2711 823 6842 • www.booyco-electronics.co.za

Subscription

to the

**SAIMM Journal for the year
January to December 2014**

*The SAIMM Journal
all you need to know!*



- **R1 717.20** local
- **US\$477.00** overseas per annum per subscription.

- ★ Less 15% discount to agents only
- ★ PRE-PAYMENT is required
- ★ The Journal is printed monthly
- ★ Index published annually
- ★ Surface mail postage included
- ★ ISSN 2225-6253

In the new world of work, we all have

- ☞ to achieve more
- ☞ at a faster pace
- ☞ with less resources
- ☞ against greater competition
- ☞ in a global economy tougher than ever before

The SAIMM Journal gives you the edge!

- ☞ with cutting-edge research
- ☞ new knowledge on old subjects
- ☞ in-depth analysis

For more information please contact:

The Southern African Institute of Mining and Metallurgy



Kelly Mathee
The Journal Subscription Department
27-11-834-1273/7



P O Box 61127, MARSHALLTOWN,
2107, South Africa



kelly@saimm.co.za or
journal@saimm.co.za
Website: <http://www.saimm.co.za>



The Southern African Institute of Mining and Metallurgy
Founded in 1894



Formation of amorphous Ti-50 at.% Pt by solid-state reactions during mechanical alloying

by M.L. Mahlatji* †, S. Chikosha*, H.K. Chikwanda*, W.E. Stumpf†, and C.W. Siyasiya†

Synopsis

Mechanical alloying of an equiatomic mixture of crystalline Ti and Pt elemental powders in a high-energy ball mill formed an amorphous alloy by solid-state reactions. Mechanical alloying was carried out in an argon atmosphere at a rotation speed of 1200 r/min and a 20:1 ball-to-powder weight ratio, for time intervals of 4 to 40 hours. At an intermediate stage of mechanical alloying, scanning electron microscopy showed the formation of characteristic layered structures of inhomogeneous composition within the powder particles. X-ray diffraction analysis showed the gradual disappearance of crystalline Bragg peaks and the emergence of broad amorphous maxima as milling progressed. The amorphization process was completed after 8–12 hours. The amorphous state of the product indicated that temperatures during processing did not exceed the crystallization temperature of the alloy.

Keywords

TiPt alloy, mechanical alloying, amorphization, solid-state reactions.

Introduction

Shape memory alloys (SMAs) undergo a reversible martensite transformation, which drives the thermoelastic properties of shape memory and pseudoelasticity (Otsuka and Ren, 1999). The Ti-50 at.% Pt alloy, which transforms on cooling from the high-temperature cubic B2 phase to the low-temperature orthorhombic B19 phase (Donkersloot and Van Vucht, 1970), has potential for high-temperature shape memory applications. The alloy has a reported martensite transformation temperature (M_S) of 1050°C (Biggs *et al.*, 2001). The pseudoelasticity and shape memory properties of the Ti-50 at.% Pt alloy under stress-free conditions have been well documented (Yamabe-Mitarai *et al.*, 2006, 2010). Shape memory applications in high-temperature environments such as in the aerospace, energy, and automotive industries require alloys with a high M_S range (300–1000°C), much higher than the M_S range reported for the commercially successful Ti-Ni alloys of just over 100°C (Otsuka and Ren, 2005). While the addition of certain alloying elements can slightly raise the M_S of Ti-Ni alloys (Firstov *et al.*, 2004),

higher transformation temperatures can be achieved only by systems with high M_S such as Ti-Pt. Alloying elements can then be used to reduce the M_S according to specific applications and to improve ductility. Reducing the M_S also lowers the effect of diffusion-controlled processes such as recrystallization, recovery, and phase separation, all of which are known to be detrimental to the reversible martensite transformation.

Conventional methods of forming the TiPt alloy usually involve plasma arc, electron beam, or vacuum induction melting, followed by a suitable thermomechanical treatment to homogenize and age the alloy. The current work explores mechanical alloying (MA) as an alternative means of producing the alloy. MA is a process of alloy formation from a mixture of powder particles in a high-energy ball mill (Soni, 2001). Chemical homogenization proceeds through a series of ball-powder-ball collisions (Figure 1), resulting in the repeated flattening, fracturing, and mutual cold welding of the powder particles coupled with short-range diffusion. This leads to the formation of a particulate alloy material suitable for consolidation and further processing.

MA of crystalline powder mixtures of two transition metals often results in the formation of amorphous alloys (Koch *et al.*, 1983; Schwarz and Koch, 1986). It is generally accepted that this is due to solid-state amorphization reactions (SSARs), driven by (a) a large negative heat of mixing in the amorphous state, and (b) one element in the powder mixture having anomalously fast diffusivity in the other (Johnson, 1986). These conditions ensure the availability of a sufficient thermodynamic driving force for the amorphization reaction, and that the

* CSIR/ MSM/LM.

† Department of Materials Science and Metallurgical Engineering, University of Pretoria, South Africa.

© The Southern African Institute of Mining and Metallurgy, 2014. ISSN 2225-6253. This paper was first presented at the, Precious Metals 2013 Conference, 14–16 October 2013, Protea Hotel, President, Cape Town, South Africa.

Formation of amorphous Ti-50 at.% Pt by solid-state reactions during mechanical alloying

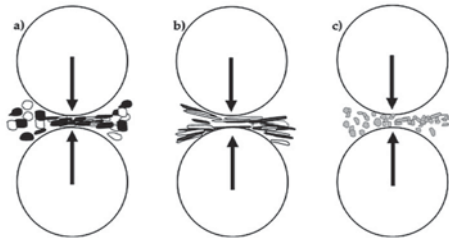


Figure 1—Schematic of the different stages during MA of a nominally ductile powder mixture: a) starting powder; b) flattened, layered composite particles; c) homogenous equiaxed particles

amorphous phase forms at a reasonable rate, faster than the competing crystalline equilibrium phase(s). The free energy state of such a process can be generally illustrated by the schematic free energy diagram (Figure 2), where it is assumed that a fully homogenous amorphous alloy with composition X is formed from a starting crystalline powder mixture of A and B. The free energy of the amorphous phase, indicated by the thick solid curve, is shown together with the dashed schematic free energies of the crystalline α -A(B) and β -B(A) solid solution phases and the equilibrium crystalline γ -intermetallic phase.

The amorphous MA product formed by SSAR is a metastable phase that requires devitrification to form an equilibrium crystalline phase suitable for the envisaged shape memory applications. As Figure 2 suggests, such alloys typically have no thermodynamic barrier against crystallization of the amorphous phase, only a kinetic barrier that suppresses the long-range atomic diffusion required for crystallization (Johnson, 1986). The amorphous phase will therefore readily undergo crystallization when heated above the crystallization temperature (T_x), where enough activation energy becomes available to overcome the kinetic barrier against crystallization.

Compared to conventional melting methods, MA offers the advantages of solid-state processing and better composition control, with the possibility of directly forming near net shape parts that require minimum machining and metal loss to produce the final part dimensions. The disadvantages of MA include easy oxidation of powder particles due to the large activated surface area involved, and the formation of a nanocrystalline parent austenite phase. Grain refinement is known to suppress the martensite transformation (Waitz *et al.*, 2004; Guimaraes, 20007). This is due to the increasing difficulty of accommodating the martensite transformation shape strain in the nanocrystalline austenite parent phase. This effect has been demonstrated for Ti-Ni based SMAs formed by crystallization of an amorphous phase (Tian *et al.*, 2009; Valeanu *et al.*, 2011). In the Ti-Pt system, however, Ti-50 at.% Pt has an M_s that lies above the T_x of 477°C (De Reus and Saris, 1990). For such alloys, the amorphous phase can be directly crystallized into the martensite phase with no prior austenite phase, as demonstrated for the Zr-Cu-Ni system (Firstov *et al.*, 2006). The possibility of directly crystallizing B19-TiPt martensite from an amorphous phase removes the limitations that would otherwise be associated with martensite formation from a nanocrystalline B2-austenite parent phase.

Experimental methods

Mechanical alloying

Elemental powders of commercially pure Ti and Pt were mixed in a 1:1 atomic ratio. The Ti particles were spherical and the Pt particles were spongy and irregular (Figure 3). MA was carried out in a Simoloyer CM01® ½ l high-energy horizontal ball mill. The charge, composed of powder and milling balls, was loaded into the jar and the jar was sealed in an Ar-filled glove box. The MA parameters are shown in Table I. The jar was periodically discharged to minimize the cold welding of powder to the milling equipment. The steady state external temperature of the jar did not exceed 37.8°C during MA due to cooling water running through the double-walled jar and flange connection. Cooling the jar increases the transfer of heat away from the contents, promoting brittle particle fracture over ductile coating of the jar walls, balls, and rotor.

Energy-dispersive X-ray analysis (EDX) showed increasing levels of contamination in the powder with increasing MA time. The major contaminants were Fe, Cr, and

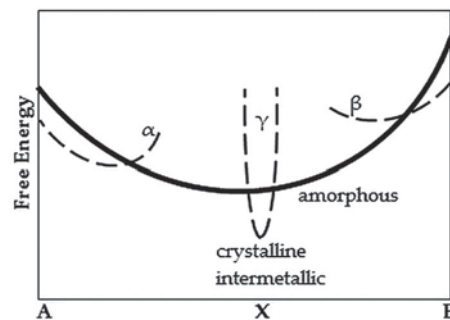


Figure 2—Schematic free energy diagram showing the free energies of the amorphous phase, the crystalline solid solutions α and β , and the crystalline intermetallic γ phase

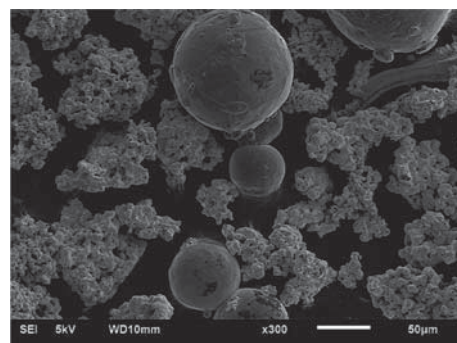


Figure 3—SE-SEM micrograph of the starting powder for MA showing spherical particles (Ti) and spongy, irregular particles (Pt)

Table I

Mechanical alloying parameters

Mill type	Simoloyer CM01® ½
Ball-Powder ratio	20:1 (w/w); 100Cr6 Ø5mm milling balls
Milling intervals	0, 4, 8, 12, 16, 24, 32, 40 hrs
Milling atmosphere	Argon
Milling speed	1200 r/min, operating and discharging runs

Formation of amorphous Ti-50 at.% Pt by solid-state reactions during mechanical alloying

Mo, corresponding to the hardened steel composition of the mill lining and rotor. Hence the contamination was attributed to wear of milling equipment. Fe levels in the milled powder ranged from ≤ 1 wt% Fe after 4 hours to well over 20 wt% Fe in powder milled for 16 hours and longer.

Structural characterization

Phase characterization of the powder was performed using X-ray powder diffraction (XRD) in a Phillips PW 1710[®] powder diffractometer with Cu K α radiation ($\lambda = 1.5421 \text{ \AA}$) over the 2θ range of $20\text{--}120^\circ$. Where applicable, the resulting diffraction patterns were analysed for average domain size and internal strain using the Scherrer method (Suryanarayana and Norton, 1998). Scanning electron microscopy (SEM) was carried out with a JEOL JSM-6510[®] microscope operating at 20 kV and equipped with an EDX detector. Transmission electron microscopy (TEM) work was performed with a JEOL JSM-2100[®] microscope operating at 200 kV with a beam current of approximately 112 μA .

Results

Morphology of powder

During the first few hours of MA, the powder displayed a strong tendency to cold weld to the balls and walls of the milling jar due to the ductility of the powder. The cold-welded powder was restricted mostly to a specific region of the jar and could be easily dislodged by turning the jar by 180° at regular intervals and running a discharging procedure. While the formation of a thin coating on milling equipment can help prevent excessive wear and minimize powder contamination, the authors have previously observed that not dislodging the welded particles regularly to reintroduce the powder back into the MA process as free-flowing powder will result in a heterogeneous final product. As MA progressed, plastic deformation strongly reduced the ductility of the powder particles, until cold welding to the milling equipment was no longer observed. Figure 4 shows that for powder milled for 4 and 8 hours, the powder particles transformed from spherical/spongy morphology (Figure 3) to a fissured morphology with a wide particle size distribution.

SEM micrographs of sectioned particles at different stages of the alloying process after MA for 4 hours are shown in Figure 5. EDX analysis showed that the dark grey regions are pure Ti and the lighter grey regions have a composition of 39–51 at.% Pt, while the white regions are Pt-rich. The repeated impact experienced by the powder particles when trapped between colliding balls causes plastic deformations and flattening. Mutual cold welding of these flattened particles result in the lamellar structure of Figure 5(a). A similar layered structure at an intermediate stage of alloying of ductile metal powders was also reported by Benjamin and Volin (1974). The repeated fragmentation and cold welding of the powder particles refined the lamellar structure, resulting in a random orientation of the lamellae within the particles as seen in Figure 5(b). Continued structural refinement resulted in homogenization and disappearance of the layered structure, with the Pt-rich layers in Figure 5(c) being the last to disappear. Beyond 4 hours of MA, all particles displayed a homogenous structure similar to Figure 5(d) with a near equiatomic composition.

Crystallinity of powder

Figure 6 shows a series of selected XRD patterns of Ti-50 at.% Pt powders at different MA time intervals. The pattern at zero hours is a superposition of hcp Ti and fcc Pt reflection peaks, showing that the starting material was a mixture of elemental crystalline powders of Ti and Pt. After 4 hours, all Ti reflection peaks have disappeared and only broad low-

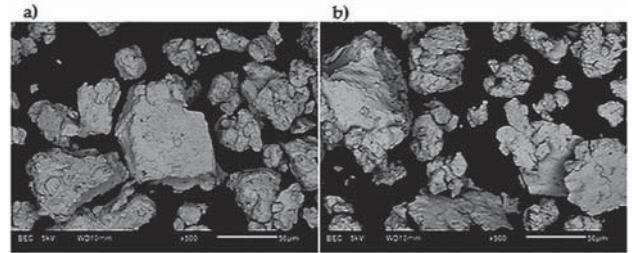


Figure 4—SE-SEM micrographs of Ti-50at%Pt powder particles after MA for (a) 4 and (b) 8 hours

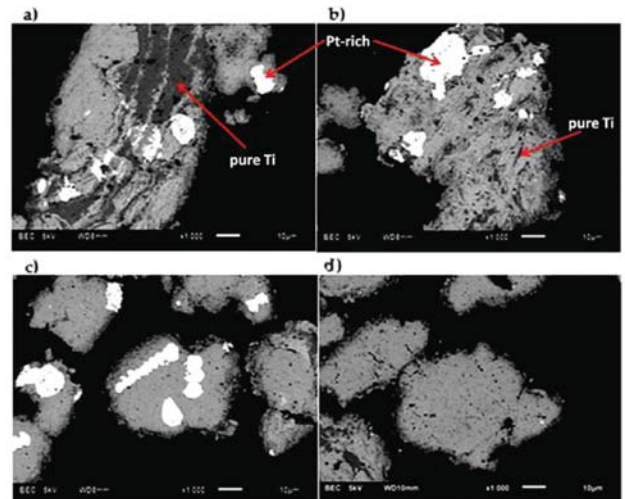


Figure 5—Ti-50at.%Pt cut and polished MA powder particles after 4 hours: (a) lamellar structure with Pt-rich (white) and pure Ti regions (dark grey); (b) randomly oriented lamellae; (c) residual Pt-rich regions in homogenous matrix; (d) complete homogenization

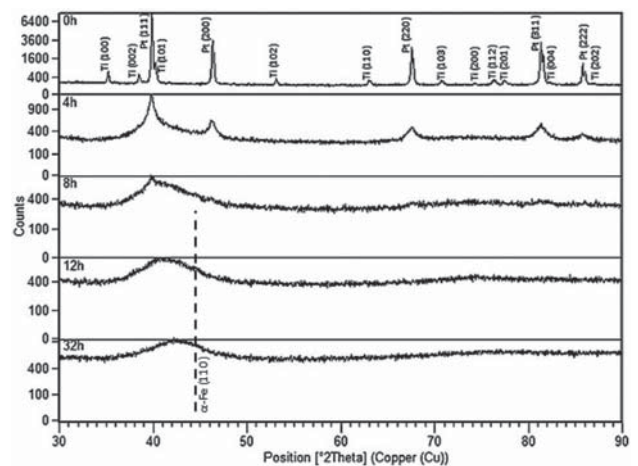


Figure 6—X-Ray diffraction patterns of Ti-50at.%Pt at different MA time intervals, the dotted line shows the position of the α -Fe (110) peak

Formation of amorphous Ti-50 at.% Pt by solid-state reactions during mechanical alloying

intensity Pt reflections can be identified. At the same time, there is an emergence of the broad maxima characteristic of amorphous alloys. The Ti layers in the composite layered particles of Figure 5 (a, b) are thinner than 5 μm and were not detected by XRD. Hence, no Ti reflections appear on the 4-hour scans.

The crystallite size of the powder was determined using the Scherrer method (Equation [1]), where d is the average domain dimension along the scattering vector (\AA), K is a shape constant ($= 0.9$), λ is the wavelength ($K\alpha_{\text{Cu}} = \lambda = 1.5421 \text{ \AA}$), θ is the X-ray scattering angle, and β is the line width (FWHM) after correction for instrument broadening with a Si standard. The tangent formula in Equation [2] was used to determine the internal strain, where ϵ is the mean lattice distortion, and β and θ are the same as for Equation [1]. The average crystallite size is reduced (and the lattice strain is increased) from 13 nm (0.87%) after 4 hours to 8.3 nm (1.30%) after 8 hours. For MA of 12 hours and beyond, all Bragg reflections had disappeared, indicating completion of the amorphization process.

$$d = \frac{K\lambda}{\beta \cos \theta} \quad [1]$$

$$\epsilon = \frac{\beta}{4 \tan \theta} \quad [2]$$

The accumulation of crystalline contaminants (mostly Fe) from wear of milling equipment as detected by EDX is not immediately apparent in the XRD patterns of Figure 6 due to the low resolution of XRD. The fully amorphous reflection after 12 hours, where the contamination level was still relatively low, has the major maximum centred near the 2θ position corresponding to the strong fcc Pt (111) and hcp Ti (101) Bragg reflections, as expected. The 32-hour pattern, however, shows how the major maximum had gradually shifted and is now centred at a higher 2θ position, due to the accumulation of Fe-rich contaminants (the highest intensity peak of bcc α -Fe (110) is $2\theta = 44.674^\circ$).

The MA process was further studied by TEM for the time intervals corresponding to partial amorphization (4 hours' MA), fully amorphous alloy (12 hours), and heavily contaminated amorphous alloy (32 hours). Figure 7 (a, b) shows TEM images with corresponding selected area diffraction (SAD) patterns after MA for 4 hours, where the amorphous phase co-exists with un-reacted Ti and Pt. This is reflected by the fine lattice fringes on the high-magnification image (arrow) and diffraction spots on the SAD. The lack of diffraction spots and lattice fringes on the powder after 12 hours (Figure 8a and b) shows that the powder is now fully amorphous, in agreement with the XRD results. After 32 hours (Figure 9a and b), SAD patterns show traces of crystalline diffraction spots in the amorphous matrix. The crystalline spots can be due to either: (a) crystallization of the previously fully amorphous powder when the powder particles trapped between colliding balls experience a momentary temperature rise exceeding the T_x of the alloy (as Figure 2 suggests), or (b) the introduction of crystalline contaminant phases into the amorphous alloy. The temperature rise from ball impacts during MA has been estimated to be only a few hundred degrees (Joarder *et al.*, 2004), well below the reported T_x of amorphous Ti-50 at.% Pt alloy. The crystallites can therefore be attributed to contam-

inants from wear of milling equipment, as detected by the low-resolution analytical techniques. This indicates that to avoid contamination, MA should not be carried out for unnecessarily long time intervals, such as beyond the point of complete amorphization.

Discussion

The formation of amorphous Ti-50 at.% Pt alloy is demonstrated by the transformation of Bragg elemental Ti and Pt crystalline reflections at the start of MA into broad, featureless reflections characteristic of amorphous alloys after 8–12 hours of MA. Similar results of amorphous phase formation by MA from elemental powder mixtures have been reported for the closely related TiNi (Schwarz *et al.*, 1985;

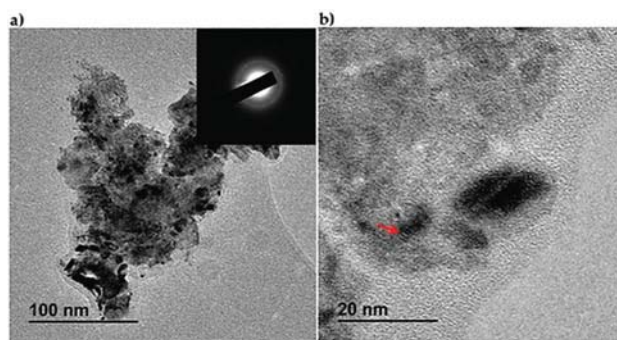


Figure 7 – Ti-50at.%Pt powder after MA for 4 hours: (a) The SAD pattern shows an amorphous halo and crystalline diffraction spots, corresponding to the remaining crystalline phases; (b) lattice fringes (arrow) in an amorphous matrix

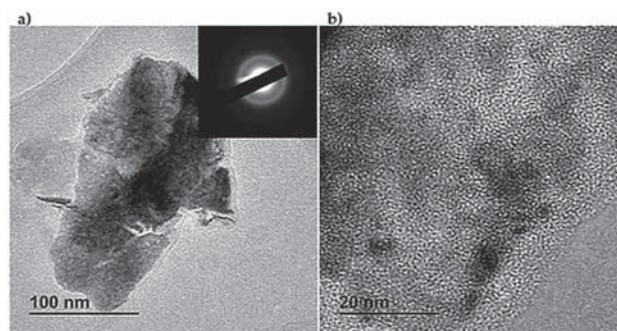


Figure 8 – Ti-50at.%Pt powder after MA for 12 hours: (a) TEM image with corresponding SAD pattern showing the amorphous halo, (b) the amorphous phase

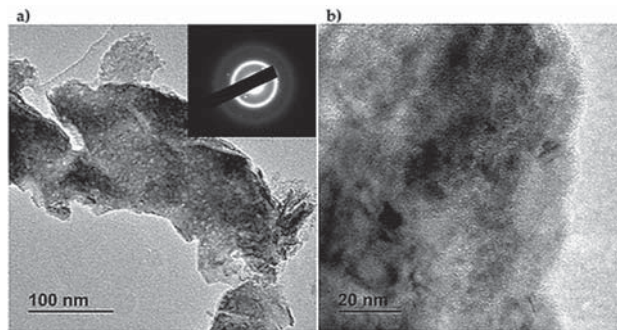


Figure 9 – Ti-50at.%Pt powder after MA of 32 hours: (a) The SAD pattern shows the amorphous halo and crystalline diffraction spots, attributed to contamination from wear of milling equipment; (b) the amorphous phase

Formation of amorphous Ti-50 at.% Pt by solid-state reactions during mechanical alloying

Liang *et al.*, 1995) and TiPd (Thompson and Politis, 1987) systems. The deformation, fracturing, and cold welding of powder particles is illustrated by Figure 4 (a, b), where the formerly spherical and spongy particles had formed agglomerates, and in some cases had become flattened and fissured. These structural changes also resulted in a reduction in crystallite size and an increase in lattice strain. The characteristic layered structure shown in Figure 5, which precedes the appearance of the homogenous structure, indicates that the alloying process proceeded by SSAR. The layered structure was due to the preferential cold welding of newly created clean Ti and Pt boundaries formed by particle fracture. It has been suggested that conditions at the layer interfaces during an intermediate stage of MA of two metals closely resemble those within conventional thin-film diffusion couples (Johnson, 1988), leading to alloy formation by solid-state interfacial interdiffusion reactions. According to the classification of Weeber and Bakker (1988), SSAR of two metals can proceed along three different paths, depending on the alloy system and experimental conditions. The XRD patterns of Figure 6 indicate that the Ti-50 at.% Pt alloy underwent a Type II reaction path, characterized by a decrement in intensity of the elemental crystalline reflections and an increment in intensity of the broad amorphous reflection.

The SSAR alloying mechanism observed in the current work is different from the observation made by Maweja *et al.*, (2012), where MA of Ti-50 at.% Pt powder in a high-energy ball resulted in formation of a disordered crystalline fcc Pt(Ti) extended solid solution. It is suggested that the different MA product phases were due to differences in milling parameters, such as the effect of using a process control agent (PCA) to control the cold welding of powder particles to milling equipment. A PCA was not used in the current work to avoid contamination and to optimize alloy formation. Besides improving the amount of free-flowing powder in the milling jar, PCAs have been shown to have a generally negative effect on the alloying process (Machio *et al.*, 2011). Similar inconsistencies in the crystallinity of the milled product have been observed in the MA of other alloy systems such as Ti-Ni, where formation of solid solutions (Mousavi *et al.*, 2008) and disordered intermetallics (Takasaki, 1998) have been reported in addition to amorphous phase formation when using different MA parameters. Determination of the relative thermodynamic stability of the fcc Pt(Ti) solid solution (reported by Maweja *et al.*, 2012), the amorphous phase (reported in the current work), and the crystalline equilibrium phase under conditions of suppressed atomic diffusion (illustrated in Figure 2) is required for a better understanding of phase transformations during MA of the Ti-Pt system.

While it is currently possible to measure the process temperature during operation of the high-energy ball mill only with a thermocouple attached externally to the wall of the milling jar, some general deductions can be made about thermal conditions inside the jar during operation. Two temperatures can be defined: (a) the ambient temperature in the jar, and (b) the momentary temperature rise during high-speed ball collisions, which is expected to be much higher than the ambient temperature. The amorphous phase is expected to readily crystallize into an equilibrium crystalline phase when heated above the T_x of the alloy. The fully

amorphous state of the milled powder after 8–12 hours shows that both the ambient and the ball-collision temperatures inside the milling jar did not exceed the T_x of the alloy, otherwise the alloy powder would have become crystalline.

Conclusions

- i. Amorphous Ti-50 at.% Pt alloy was formed by SSAR during MA of crystalline elemental powders of Ti and Pt. At an intermediate stage, the mechanical mixing and deformation led to formation of characteristic layered particles. Amorphization was completed after 8–12 hours. Milling for longer time intervals beyond the completion of amorphization should be avoided as it would result in powder contamination from wear of milling equipment. While it was possible to measure only the external temperature of the milling jar, it can be inferred from the amorphous state of the product that the temperature during processing did not exceed the T_x of the alloy
- ii. Analogies can be drawn between the formation of a homogenous amorphous alloy by MA and the formation of a homogenous molten alloy by ordinary melting. A liquid and an amorphous alloy with the same composition represent the 'molten' and 'frozen' intermediate states in the process of forming crystalline alloys. The former requires cooling towards T_x and the latter requires heating towards T_x to form the equilibrium crystalline phase. An amorphous Ti-50 at.% Pt alloy formed by MA therefore represents a 'molten' phase, formed without heating above the extremely high melting points of the components and of the intermetallic phase
- iii. Future work includes devitrification of the amorphous alloy to form crystalline Ti-50 at.% Pt suitable for shape memory testing. Semi-empirical thermodynamic modelling will be done to establish solid solubility limits of Ti in fcc Pt under polymorphic conditions, as well as the relative free energies of the solid solution and the amorphous and the crystalline α -TiPt phases at temperature below the T_x . This is required to understand the differences in the product phases formed during MA of the Ti-Pt system.

Acknowledgements

The authors wish to thank the Department of Science and Technology and Anglo American Platinum for co-funding the work, and Anglo American Platinum for providing the Pt powder. The kind permission of both the CSIR and the University of Pretoria to publish this work is acknowledged.

References

- BENJAMIN, J.S. and VOLIN, T.E. 1974. The mechanism of mechanical alloying. *Metallurgical Transactions*, vol. 5. pp.1929-1934.
- BIGGS, T., CORTIE, M.B., WITCOMB, M.J., and CORNISH, L.A. 2001. Martensitic transformations, microstructure, and mechanical workability of TiPt. *Metallurgical and Materials Transactions A*, vol. 32A. pp. 1881-1886.
- DE REUS, R. and SARIS, F.W. 1990. The crystallization temperature of amorphous transition-metal alloys. *Materials Letters*, vol. 9, no. 12. pp. 487-493.
- DONKERSLOOT, H.C. and VAN VUCHT, J.H.N. 1970. Martensitic transformations in gold-titanium, palladium-titanium and platinum-titanium alloys near the equiatomic composition. *Journal of the Less-Common Metals*, vol. 20. pp. 83-91.

Formation of amorphous Ti-50 at.% Pt by solid-state reactions during mechanical alloying

- FIRSTOV, G.S., VAN HUMBEECK, J., and KOVAL, Y.N. 2004. High-temperature shape memory alloys: some recent developments. *Materials Science and Engineering A*, vol. A378. pp. 2–10.
- FIRSTOV, G.S., KOVAL, Y.N., VAN HUMBEECK, J., PORTIER, R., VERMAUT, P., and OCHIN, P. 2006. Phase transformations in Zr-29.56at.%Cu-19.85at.%Ni melt-spun high-temperature shape memory alloy. *Materials Science and Engineering A*, vol. A438-440. pp. 816–820.
- GUIMARÃES, J.R.C. 2007. Excess driving force to initiate martensite transformation in fine-grained austenite. *Scripta Materialia*, vol. 57. pp. 237–239.
- JOARDAR, J., PABI, S.K., and MURTY, B.S. 2004. Estimation of entrapped powder temperature during mechanical alloying. *Scripta Materialia*, vol. 50. pp. 1199–1202.
- JOHNSON, W.L. 1986. Thermodynamic and kinetic aspects of the crystal to glass transformation in metallic materials. *Progress in Materials Science*, vol. 30. pp. 81–134.
- JOHNSON, W.L. 1988. Crystal-to-glass transformation in metallic materials. *Materials Science and Engineering*, vol. 97. pp. 1–13.
- KOCH, C.C., CAVIN, O.B., MCKAMEY, C.G., and SCARBROUGH, J.O. 1983. Preparation of 'amorphous' Ni60Nb40 by mechanical alloying. *Applied Physics Letters*, vol. 43. pp. 1017–1019.
- LIANG, G.X., WANG, E.D., and LI, Z.M. 1995. Effects of ball milling intensity on structural changes in mixed 50Ni-50Ti powders during mechanical alloying process. *Materials Science and Technology*, vol. 11. pp. 347–350.
- MACHIO, C., CHIKWANDA, H., and CHIKOSHA, S. 2011. Effect of process control agent (PCA) on the characteristics of mechanically alloyed Ti-Mg powders. *Journal of the Southern African Institute of Mining and Metallurgy*, vol. 111. pp. 149–153.
- MAWEJA, K., PHASHA, M.J., and YAMABE-MITARAI, Y. 2012. Alloying and microstructural changes in platinum-titanium and annealed powders. *Journal of Alloys and Compounds*, vol. 523. pp. 167–175.
- MOUSAVI, T., KARIMZADEH, F., and ABBASI, M.H. 2008. Synthesis and characterization of nanocrystalline NiTi intermetallic by mechanical alloying. *Materials Science and Engineering A*, vol. 487. pp. 46–51.
- OTSUKA, K. and REN, X. 1999. Recent developments in the research of shape memory alloys. *Intermetallics*, vol. 7. pp. 511–528.
- OTSUKA, K. and REN, X. 2005. Physical metallurgy of Ti-Ni-based shape memory alloys. *Progress in Materials Science*, vol. 50. pp. 511–687.
- SCHWARZ, R.B., PETRICH, R.R., and SAW, C.K. 1985. The synthesis of amorphous Ni-Ti alloy powders by mechanical alloying. *Journal of Non-Crystalline Solids*, vol. 76. pp. 281–302.
- SCHWARZ, R.B., and KOCH, C.C. 1986. Formation of amorphous alloys by the mechanical alloying of crystalline powders of pure metals and powders of intermetallics. *Applied Physics Letters*, vol. 49. pp. 146–148.
- SONI, P.R. 2001. *Mechanical Alloying: Fundamentals and Applications*. Cambridge International Science Publishing, Cambridge.
- SURYANARAYANA, C. and NORTON, M.G. 1998. *X-Ray Diffraction. A Practical Approach*. Plenum Press, New York.
- TAKASAKI, A. 1998. Mechanical alloying of the Ti-Ni system. *Physica Status Solidi (a)*, vol. 169. pp. 183–191.
- THOMPSON, J.R. and POLITIS, C. 1987. Formation of amorphous Ti-Pd alloys by mechanical alloying methods. *Europhysics Letters*, vol. 3. pp. 199–205.
- TIAN, B., TONG, Y.X., CHEN, F., LIU, Y., and ZHENG, Y.F. 2009. Phase transformation of NiTi shape memory alloy powders prepared by ball milling. *Journal of Alloys and Compounds*, vol. 477. pp. 576–579.
- VALEANU, M., LUCACI, M., CRISANO, A.D., SOFRONIE, M., LEONAT, L., and KUNCSER, V. 2011. Martensitic transformation in Ti50Ni30Cu20 alloy prepared by powder metallurgy. *Journal of Alloys and Compounds*, vol. 509. pp. 4495–4498.
- WAITZ, T., KAZYKHANOV, V., and KARNTHALER, H.P. 2004. Martensitic phase transformations in nanocrystalline NiTi studied by TEM. *Acta Materialia*, vol. 52. pp. 137–147.
- WEEBER, A.W. and BAKER, H. 1988. Amorphization by ball milling. A review. *Physica B*, vol. 153. pp. 93–135.
- YAMABE-MITARAI, Y., HARA, T., MIURA, S., and HOSODA, H. 2010. Shape memory effect and pseudoelasticity of TiPt. *Intermetallics*, vol. 18. pp. 2275–2280.
- YAMABE-MITARAI, Y., HARA, T., MIURA, S., and HOSODA, H. 2006. Mechanical properties of Ti-50(Pt, Ir) high-temperature shape memory alloys. *Materials Transactions*, vol. 47, no. 3. pp. 650–657. ◆

Leader in Refractory Solutions



Adding value to the pyrometallurgical and chemical industries of Southern Africa and the world.

Verref is a leading manufacturer of refractories and provider of solutions to the pyrometallurgical, chemical and manufacturing industries.

Our team of experienced refractory engineers, metallurgists and technicians can assist with problem identification, areas for improvement and training.

Verref is focused on building long term partnerships, adding value to our partner's businesses from product specification to product disposal.

www.verref.co.za Email: salesadmin@verref.co.za

VEREENIGING REFRACTORIES
HEAD OFFICE
Barrage Road, Vereeniging,
P.O. Box 117, Vereeniging, 1930
Republic of South Africa
Tel: +27 (0)16 450 6111
Fax: +27(0)16 421 2481



Verref
Vereeniging Refractories (Pty) Ltd
Trusting in Experience and Innovation




PROUD TO BE
SOUTH AFRICAN



Ion exchange technology for the efficient recovery of precious metals from waste and low-grade streams

by V. Yahorava* and M. Kotze*

Synopsis

Efficient recovery of precious metals from process solutions is essential for improving process economics. Traditionally, precious metals are relatively effectively recovered from waste streams via precipitation or cementation. However, these approaches have a number of drawbacks, including poor water balance, creation of environmentally unfriendly waste streams, and losses of precious metals. Ion exchange technology is an alternative for the recovery of precious metals from waste or low-grade streams. This technology allows the recovery of the precious metals to extremely low levels (micrograms per litre) with relatively high upgrade ratios from the solution onto the resin without major water balance concerns, while the impact on the environment could be minimized or avoided.

Research was conducted on the recovery of platinum group metals and gold from different low-grade and waste streams from one of the precious metals refineries in South Africa by means of ion exchange. Various functionalities and matrices (granular and fibrous) of ion exchange materials were evaluated. The results from these studies indicated that in some cases ion exchange could be very effective for the recovery of precious metals, and that the PGM concentration could be reduced to < 1 mg/L. The upgrading ratios of the various PGMs onto the specific fibres were relatively high for the specific streams evaluated, which might in some cases justify incineration of the loaded material instead of stripping and recycling the adsorbent. The cost of direct incineration for one of the waste streams tested would be less than 1% of the value of the PGMs recovered. However, the adsorbent has to be carefully selected and the process design optimized for each specific stream.

Keywords

PGMs and Au refining, precious metals, waste streams, low-grade streams, ion exchange, resin, fibre, recovery.

Introduction

Waste streams generated during the refining of precious metals may contain significant amounts of platinum group metals (PGMs) and gold (Au). Currently, refineries are using mainly precipitation and cementation techniques for the recovery of valuable metals from low-grade and waste streams. However, there are major drawbacks in using these technologies, including incomplete recovery of valuable metals and generation of waste streams that carry significantly more contaminants than the original waste streams. There is therefore a need to use alternative

technology to precipitation/cementation, which would allow the cost-effective and efficient recovery of precious metals, with low or minimal additional environmental implications.

Ion exchange and/or adsorption technology can resolve difficulties associated with the recovery of precious metals from low-grade and waste streams by minimizing waste generation and improving the overall economics of the process. Smopex® and SuperLig® materials are widely known as an option for recovery of valuable metals in the precious metals industry (Danks, n.d.; Izatt, Bruening, and Izatt, 2012). However, the cost of these materials (typically much greater than US\$200 per kilogram) often prevents refineries from considering them for waste treatment.

Over the past few years extensive research has been performed on the application of conventional ion exchange (IX) materials for the recovery of PGMs and Au from various low grade streams. A number of South African refineries provided some of their low-grade streams, which are currently treated via precipitation or cementation for PGM and Au recovery. The current paper reports on a few successful examples of the potential of ion exchange technology for the treatment of such streams. Ion exchange can be designed to result in highly efficient recovery of PGMs and Au, often without the addition of further contaminants.

The test work programme for the evaluation of the various ion exchange materials for the recovery of precious metals from various streams was as follows:

* Mintek, Randburg, South Africa.

© The Southern African Institute of Mining and Metallurgy, 2014. ISSN 2225-6253. This paper was first presented at the, Precious Metals 2013 Conference, 14–16 October 2013, Protea Hotel, President, Cape Town, South Africa.

Ion exchange technology for the efficient recovery of precious metals from waste

- Selection of the most promising functional groups commercially available on ion exchange materials;
- Evaluation of granular and fibrous ion exchangers
- Comparison of equilibria and fixed bed breakthrough profiles.

Detailed results and information on the streams and materials that were tested are not provided in this paper due to confidentiality. Nevertheless, the major benefits of conventional ion exchange for the treatment of some low-grade/waste streams containing precious metals are highlighted.

Background

The precious metal refineries combine different methods to recover silver, gold, and PGMs (platinum, palladium, rhodium, iridium and ruthenium). Depending on the process used in a specific refinery, waste streams containing PGMs and/or gold have different chemical compositions, pH, and Eh values. Due to the competitive nature of the PGM refining business and the high value of the products, very little detail of the processes used by the individual South African refiners has been published. The refineries from which waste streams were sourced for this study restricted the publication of the detailed compositions of their waste streams in this paper.

The efficiency of IX for the recovery of various metals from low-grade refinery streams depends on the chemical characteristics of the stream. For example, PGMs form a number of complexes in chloride medium depending on Eh, pH/free acid concentrations, and chloride concentrations. The major PGM species in chloride medium are shown in Table I.

In chloride acid media PGMs are present mainly as anionic species and conventional anion exchange materials could be considered for their bulk recovery from low-grade streams.

IX, using commercially available adsorbents, might be a very cost-effective technology for the recovery of PGMs and Au from low-grade or waste streams, without the generation of more contaminated waste as is the case with precipitation and cementation.

IX materials traditionally used in hydrometallurgy are supplied in the form of granular resins. Recently, production of fibrous ion exchange materials was scaled-up, thus opening an opportunity for their evaluation and comparison with granular materials (Yahorava, Kotze, and Auerswald, 2013). Enlarged images of resin beads and fibre filaments are shown in Figure 1.

Granular IX materials, in fixed bed systems, have some disadvantages []:

- Slow reaction rates and diffusion: relatively large resin bead sizes (400–600 μm) are generally used in order to prevent excessive pressure drop in fixed bed columns, which results in relatively slow kinetics and diffusion. The main consequences of this are:
 - Large ion exchange resin columns and resin inventories, so high CAPEX
 - Higher OPEX due to kinetic constraints on achieving equilibrium, thereby limiting the operating capacity of the resin, hence increasing reagent consumption per mass of valuable metal
 - Generation of relatively large, mixed volumes of solutions due to mixing occurring during diffusion when different process streams are passed through the resin bed (adsorption stream, wash streams, elution stream).
- Poor water balance:
 - Generation of excessively large effluent streams (especially at low upgrading ratios onto the resin).

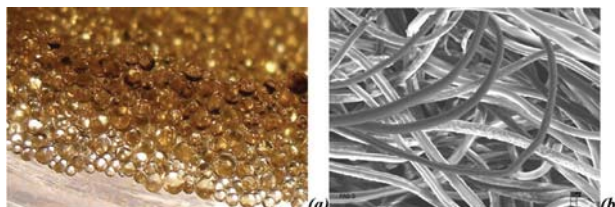


Figure 1 – Images of: (a) granules of resins and (b) filaments of fibres

Table I

PGM species in aqueous chloride medium (Bernardis, Grant, and Sherrington, 2005; Boehm Hampel, 1972; Borg et al., 1955; Hubicki et al., 2006; Anonymous, n.d; Ginzburg et al., 1975)

Ruthenium		Rhodium		Palladium	
Ru (III)	[RuCl ₆] ³⁻ [Ru(H ₂ O)Cl ₅] ⁻ [Ru(H ₂ O) ₂ Cl ₄] ⁻ [Ru(H ₂ O) ₃ Cl ₃]	Rh (III)	[RhCl ₆] ³⁻ [Rh(H ₂ O)Cl ₅] ⁻ [Rh(H ₂ O) ₂ Cl ₄] ⁻	Pd (II)	[PdCl ₄] ²⁻ [PdH ₂ OCl ₃] ⁻
Ru (IV)	[RuCl ₆] ²⁻ [Ru ₂ OCl ₁₀] ⁴⁺ [Ru ₂ OCl ₈ (H ₂ O) ₂] ²⁻	Rh (IV)	RhCl ₆ ²⁻	Pd (IV)	[PdCl ₆] ²⁻
Osmium		Iridium		Platinum	
Os (IV)	[OsCl ₆] ²⁻ [Os(H ₂ O)Cl ₅] ⁻	Ir (III)	[IrCl ₆] ³⁻ [Ir(H ₂ O)Cl ₅] ⁻ [Ir(H ₂ O) ₂ Cl ₄] ⁻	Pt (II)	[PtCl ₄] ²⁻
				Pt (IV)	[PtCl ₆] ²⁻ [PtOHC ₅] ²⁻ [Pt(OH) ₂ Cl ₄] ²⁻

Ion exchange technology for the efficient recovery of precious metals from waste

- Resin loss:
 - Osmotic shock and excessive pressure results in resin loss through breakage, which increases the pressure drop across a fixed bed column and the OPEX (resin replacement). Also, resin breakage can result in a loss of valuable metal loaded onto the resin fines.

Fibrous ion exchange materials are filaments with diameters of 20–50 μm , containing ionizing and complexing functional groups (Soldatov, 2008). These materials can have the same functional groups to those on resins, and hence be applied for similar applications.

Fibres have the following advantages over granular analogues (Soldatov, 2008):

- Short diffusion paths that provide adsorption rates that can be up to hundred times faster than that of conventional granular resins (with particle diameters usually between 0.25 and 1 mm). This would result in a significant decrease in the CAPEX for the specific unit operation
- Higher osmotic stability and hence minimal losses, thereby decreasing the associated OPEX and valuable metal loss
- Pressure drop across a fibre bed is lower than in packed resin beds, as the compressibility of fibre is limited.
- Operating capacities are closer to theoretical capacities as a result of faster kinetics, hence reagent consumption and OPEX could be lower.

Both fibrous and granular ion exchange materials were evaluated for the recovery of PGMs and Au from low-grade or waste streams.

Experimental

Resin/fibre conversion

Portions of each of the selected exchangers were loaded into a column. Strong- and weak-base anion exchange resins/fibres were converted to the chloride form, while the chelating resin was converted to the H^+ -form by passing 4 bed volumes (BVs) of 1 M HCl through the column at a flow rate of 2 BV per hour. In order to remove entrained acid, the adsorbents were washed with deionized water until the pH of the effluent water reached approximately 2.

Screening tests

Portions of the converted (H^+ or Cl^- form) adsorbents were batch-contacted with the specific liquor at different volumetric or mass ratios for 24 hours at ambient temperature in rolling bottles. The contact ratio was calculated based on the capacity of the tested material and the estimated total concentration of precious metal complexes in the liquor.

After 24 hours, the solution was separated from the resin/fibre via screening through a 212 μm screen. The resins were washed with deionized water and oven-dried at 60°C. The solution samples and the resins were analysed for the metals of interest by inductively coupled plasma – optical emission spectroscopy (ICP-OES) or inductively coupled

plasma – mass spectroscopy (ICP-MS) depending on the detection limit required. Detection limits of ICP-OES and ICP-MS are >5 mg/L >10 $\mu\text{g/L}$ respectively.

Equilibrium loading/adsorption isotherm

The ion exchange materials to be used for the generation of the equilibrium loading isotherms were selected based on the preliminary screening tests. If promising materials were available in both fibrous and granular forms, both adsorbents were tested. The solution was batch-contacted with the chosen adsorbents at different resin-to-solution ratios (mass ratios for fibre and volumetric ratios for granular resins) for 24 hours in a similar manner as described above. After 24 hours, the adsorbents were separated from the solution and barren solution samples were collected. The adsorbents were then washed with de-ionized water and oven-dried at 60°C. Solution samples and dried adsorbents were analysed for the metals of interest.

Column breakthrough test work

Column breakthrough tests were conducted by passing the feed solution through a fixed bed of resin/fibre at a specified flow rate. The column was charged with wet resin, and then filled with water. The resin bed was stirred with a spatula to remove any air bubbles prior to actual solution being passed through the column. Dry fibre was packed into the column, which was wetted by passing water upwards through the column to limit air entrainment in the fibre bed and solution bypass during operation. Hence, during the test work liquors flowed downwards through the granular resin beds and upwards through the fibre beds.

The solution throughput was estimated based on the results of the equilibrium loading isotherm tests. Barren solution samples were collected at specific bed volume intervals. After the bed had reached saturation level (>80% of the metals targeted was detected in the effluent), it was washed with deionized water to remove entrained solution. The adsorbents were then oven-dried at 60°C. Solution and adsorbent samples were analysed for the metals of interest via ICP-OES or ICP-MS.

Fibres were tested in the form of staple; they were packed into the column to 0.33 g/cm^3 packing density (absolutely dry fibre). This density was similar to the density of the resins tested (d_{50} of the resins included in the evaluation varied between 500 and 600 μm).

Since the height of the column was 20 cm and the diameter was 1.4 cm, the column was charged with approximately 30 mL of resin and 10 g of fibre.

Results and discussion

Brief description of low-grade PGM streams

Result of the evaluation of three low-grade PGMs streams are reported:

- 'Pd Waste' – barren liquor after precipitation and filtration of $(\text{Pd}(\text{NH}_3)_2\text{Cl}_2)$
- 'Pt Waste' – barren liquor after precipitation and filtration of NH_4PtCl_6
- 'Mixed Waste' – a combination of various low-grade PGMs and Au streams prior (taken before neutralization and sulphidization).

Ion exchange technology for the efficient recovery of precious metals from waste

During the test work programme a number of batches of solution were obtained, and the concentrations of the precious metals as well as Eh and pH values varied. Results generated for some of the streams (Pd and Pt wastes, Mixed Waste) are reported in this paper. However, the impact of the variation in feed composition has to be well understood in order to ensure optimum process design.

IX materials tested

The typical speciation of the precious metals (Table II) in the respective solutions was used in the selection of appropriate ion exchangers.

Abbreviations used for the ion exchange materials as well as some of characteristics and indicative prices for the granular resins are listed in Table II.

Strong acid cation exchanger was included in the evaluation as examples of its successful application for precious metals recovery have been reported in the open literature (Boehm and Hampel, 1972; Borg *et al.*, 1955). IDA resin was tested as it exhibits the properties of an anion exchanger in solutions of pH < 2 or less as both carboxylic groups and nitrogen occur in the protonated form (Hubicki *et al.*, 2006).

Adsorbents 1, 3, and 5 are commercially available in fibrous and granular form. Other adsorbents can be produced on a fibrous matrix on request if a market need is identified. Generally, the price of fibrous materials is approximately 25 % higher than that of granular ones (mass basis comparison).

Ion exchange fibres are usually supplied in the air dry form as yarn, staple, threads, non-woven materials, or webs and sold on the mass basis. Ion exchange resins typically are sold on the wet volume basis. In order to compare fibre and resin performance it was assumed that once packed into the column and pressed, fibre will have density of 0.33 g/cm³.

Screening of IX functional groups

Palladium and Platinum Waste streams

The compositions of the Pt Waste, Pd Waste, and Mixed Waste streams used for the screening tests are given in Table III. Base metal concentrations were less than 5 mg/L in the streams tested.

Adsorbents were contacted with portions of solution in a 1-to-10 (v/v) ratio. Results of screening various functional groups (Table I) for the recovery of Pt and Pd from the Pd and Pt Waste streams are presented in Figure 2 and Figure 3 respectively.

The adsorbents were evaluated with regard to Pt and Pd upgrading ratios only as the other impurities were present in concentrations close to or below the detection limit of ICP-OES (<5 mg/L). During selecting the most suitable material for treatment of the Mixed Waste solution, all the PGMs were traced.

Upgrades were calculated as follows:

$$Upgrade = \frac{q}{Me_{barren}}$$

where

q – metal concentration on resin, mg/L

Me_{barren} – metal concentration in solution after contact, mg/L.

Table II

IX materials tested

Adsorbent	Functionality	Groups	Matrix	Forms evaluated	Theoretical capacity, eq/L	Resin price, USD/L
1	Polyamine amphoteric	TETA	PAN	Fibrous and granular	4.8 (fibre & resin)	16
2	Chelating weak acid	IDA	PP-ST-DVB	Granular	2	11
3	Strong acid	SA		Fibrous & granular	1.8 (resin) 1.4 (fibre)	4
4	Strong base	TMA		Granular	1.4	6
5	Strong base	TBA		Fibrous and granular	0.3 (resin) 0.8 (fiber)	8
6	Weak base	DMA		Granular	n/a	5

TETA – triethyltetramine; IDA – iminodiacetic acid; SA – sulphonic acid; TMA – trimethylamine; TBA – tributylamine; DMA – dimethylamine; PAN – polyacrylonitrile; PP-ST-DVB – polypropylene styrene divinylbenzene

Table III

Composition of waste streams used for scouting test work

Stream	Concentration, mg/L						Concentration, g/L	ORP (Ag/ AgCl)	pH
	Ru	Rh	Pd	Ir	Pt	Au			
Pd Waste	<2	<2	88	<2	24	<2	60	653	0.18
Pt Waste	<2	<2	3	<2	14	n/a	120	520	0.3
Mixed Waste	119	7	2	21	43	1	71	367	0.31

Ion exchange technology for the efficient recovery of precious metals from waste

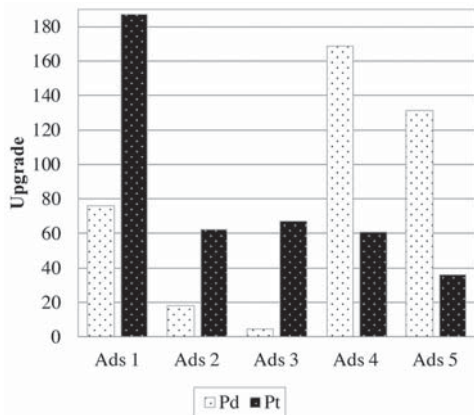


Figure 2—Pt and Pd upgrading ratios from Pd Waste stream

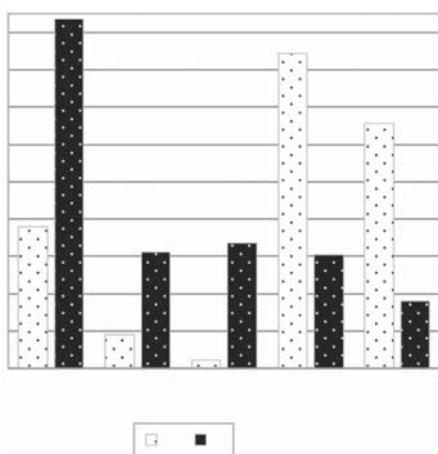


Figure 3—Pt and Pd upgrading ratios from Pt Waste stream

The highest Pd and Pt upgrades from both streams were achieved by Adsorbents 1, 4, and 5 having anion exchange functionalities (see Table I). For the Pd Waste stream (Figure 1) Pd was upgraded more than a 100 times with Adsorbents 1, 4, and 5, while the upgrading of Pt onto these adsorbents was negligible. This was probably due to preferential adsorption of Pd chloride species of Pt at the conditions tested.

For the Pt Waste stream, the following results were found:

- Adsorbent 1: Pt and Pd upgrade ratios of >180 and > 60 respectively
- Adsorbents 4 and 5 showed higher upgrades for Pd (>120) than for Pt (<60) ;

Adsorbent 4 was excluded from further test work as no fibrous analogue was available, but it could be considered in future.

Mixed Waste stream

Results of the adsorbent screening tests on the Mixed Waste solution are presented in Figure 4. Only Adsorbent 1 was found to be promising for Pt and potentially Rh recovery from this liquor.

Equilibrium adsorption isotherms

Palladium and Platinum Waste streams

Equilibrium adsorption isotherms for Pd and Pt recovery from the relevant waste streams were generated using Adsorbents 1 and 5 in fibrous and granular form. The compositions of the solutions used are given in Table IIIII.

Figure 5 illustrates the equilibrium isotherms for Pd and Pt obtained with the Pd Waste stream. Resin/fibre loadings were calculated by using feed and barren solution analysis. In order to convert metal loadings onto fibre into mg/L, a fibre compression density of 0.33 g/cm³ was used. In some cases, a full equilibrium isotherm was not achieved due to an insufficient amount of solution available for the test work.

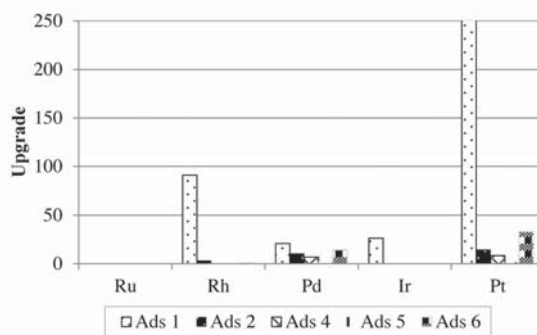


Figure 4—PGM recovery from mixed waste stream

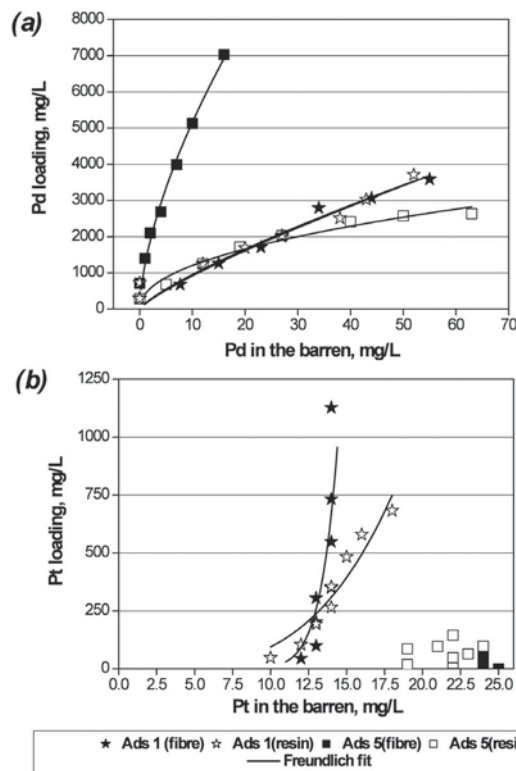


Figure 5—Equilibrium adsorption isotherms for (a) Pd and (b) Pt generated for the Pd Waste stream

Ion exchange technology for the efficient recovery of precious metals from waste

Adsorbent 1 (TETA functional groups), in fibrous and granular forms, showed similar equilibrium behaviour towards Pd and Pt:

- ▶ Comparable maximum Pd loadings of approximately 3.5 g/L were achieved, giving upgrade ratio of about 65–70
- ▶ Upgrading ratios for Pt at around 13 mg/L Pt in the equilibrium solution were 80 and 30 for the resin and fibre respectively.

The following results were obtained with Adsorbent 5 (TBA functional groups):

- ▶ The Pd loading onto the resin at >40 mg/L Pd in solution was around 2.8 g/L, which was a <50 times upgrade
- ▶ The fibrous IX material resulted in a Pd loading of 7 g/L at a Pd solution concentration of 18 mg/L in solution, which was a >380 times upgrade
- ▶ Very little Pt loading was obtained on either the granular or fibrous materials.

Based on the results from these scouting tests, it seemed that Adsorbent 1 would be successful for the recovery of Pt and Pd, but Adsorbent 5 might be useful in the selective recovery of Pd from streams containing Pt. The performance of this fibre in the actual separation of Pd from the other PGMs during refining should also be further evaluated.

Due to the unfavourable shape of the equilibrium isotherm and impossibility of reducing Pt concentration to <10 mg/L, this type of material was excluded from further evaluation for this specific stream. The reason for inefficient Pt extraction from the Pd waste stream might be due to the formation of poorly extracted Pt species under the conditions tested.

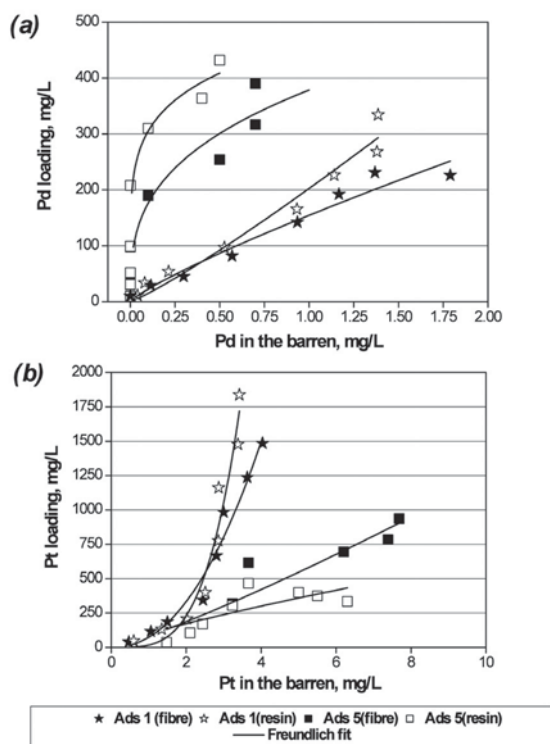


Figure 6—Equilibrium adsorption isotherms for (a) Pt and (b) Pd adsorption from the Pt Waste stream

Equilibrium adsorption isotherms generated for Pt and Pd recovery from the Pt Waste stream are presented in Figure 6.

None of the tested materials reached their final maximum loadings for this specific liquor, as the barren concentrations were still considerably lower than that of the feed concentration at the maximum ratio tested (1:500 resin- to-liquor m/m).

Adsorbent 1 showed higher recovery efficiencies towards Pt, while Adsorbent 5 extracted more Pd. Maximum Pd and Pt upgrades achieved with Adsorbent 5 were around 860 and 100 respectively, while Adsorbent 1 produced upgrades of 240 and 680 for Pd and Pt respectively at the maximum solution-to-adsorbent ratio (v/v) of 500.

Adsorbent 5, containing strong base functional groups on both fibrous and granular forms, was chosen for further evaluation of Pd recovery from the relevant waste stream, while Adsorbent 1 with polyamine functionality, was tested for Pt recovery from the platinum waste stream.

New batches of waste streams were received, and the compositions are given in Table IV. Concentrations of other PGMs in the feed were close to the ICP-OES detection limit of 2 mg/L and were not monitored further.

Equilibrium isotherms generated for the recovery of Pd and Pt from the second batch of Pd and Pt Waste streams with fibrous and granular ion exchangers carrying TBA and TETA groups are presented in Figure 7 and Figure 8 respectively.

Maximum loadings of palladium achieved from the Pd Waste solution with strong-base fibre and resin (Adsorbent 5) were 10.5 g/L and 5 g/L, respectively, at equilibrium Pd barren concentrations of 110 mg/L. Upgrades of approximately 100 and 50 were achieved for the fibre and resin

Table IV

Composition of second batch of Pt and Pd waste streams

Streams	Concentration, mg/L		[Cl] g/L	Eh (Ag/AgCl), mV	pH
	Pd	Pt			
Pd Waste	119	22	63	646	0.6
Pt Waste	<5	333	133	580	0.3

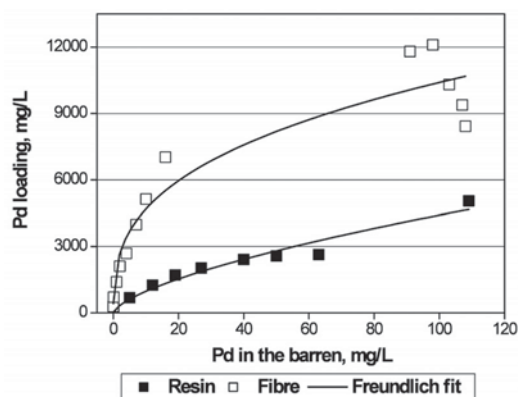


Figure 7—Equilibrium loading isotherms for palladium on fibre and resin with TBA functional groups, Pd Waste stream

Ion exchange technology for the efficient recovery of precious metals from waste

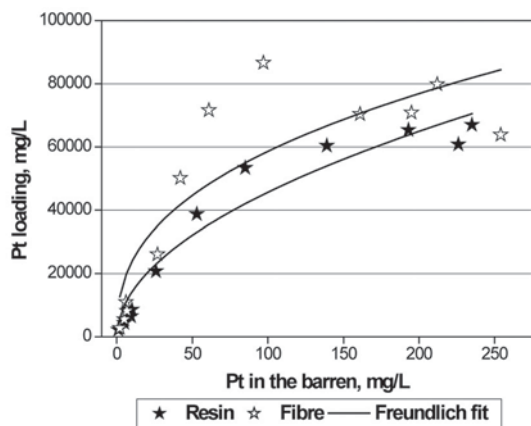


Figure 8—Equilibrium loading isotherms for platinum on fibre and resin with TETA functional groups, Pt Waste stream

respectively; hence recovery of the Pd from the loaded adsorbents via incineration would probably not be economically feasible. Therefore, recovery of the metal from the adsorbent by elution should be considered. Eluants such as 6 M HCl, acidic thiourea, and ammonia bisulphite might be suitable (Korkisch, 2000; Bernardis, Grant, and Sherrington, 2005).

The maximum Pt loadings achieved with both fibrous and granular ion exchangers (Adsorbent 1) from the Pt Waste stream were similar at about 60-75 g/L resin/fibre, at an equilibrium barren Pt concentration of about 250 mg/L, hence upgrading ratios of >200 times. Based on the relatively high upgrade achieved, the current price of Pt metal (i.e. 45 818 US\$ per kilogram on 13 March 2014) and the cost per kilogram of adsorbent (about US\$50), it might be cost-effective to recover the metal by incineration of the adsorbent instead of elution.

Table V presents preliminary costs for platinum recovery from the low-grade waste stream via ion exchange technology (resin or fibre with weak base polyamine functionality can be used) followed by incineration of the loaded material.

The cost of the material, if incinerated and not recycled, would be less than 1% of the value of metal recovered. This might allow for incineration to be economically attractive. Ion exchange columns/cartridges could easily be introduced into the refinery for waste treatment without excessive capital costs, and tested on site.

Mixed Waste stream

Equilibrium adsorption isotherms for platinum recovery from the Mixed Waste stream (Table III) with Adsorbent 1 are presented in Figure 9. The upgrading ratio for Pt was about 140 for both adsorbents.

The Pt adsorption equilibrium of the resin was somewhat more favourable than that of the fibre. Based on these results and those obtained for the recovery of Pt from the Pt Waste stream, it was clear that the target would generally be to recover Pt and Pd from their individual waste streams and not from a mixture in order to obtain improved performance from the IX system.

There was very little Pd in the Mixed Waste stream, but the Ru concentration was relatively high. However, the loadings observed for these metals were <0.1 g/L.

Breakthrough tests with fibrous and granular IX materials

Pd Waste Stream: breakthrough

Breakthrough profiles for the recovery of Pd from the Pd waste stream (Table V) using granular and fibrous Pd-selective ion exchange materials (Adsorbent 5) are shown in Figure 10.

Pd breakthrough (>1 mg/L in barren) was reached after passing approximately 21 BVs of solution through the resin bed and approximately 93 BVs through the fibre column at a flow rate of approximately 2 BV/h. Various solution flow rates were evaluated for the fibre: namely, 2, 5, 10, and 15 BV/h. Results indicated that the Pd mass transfer zone time for the fibre was highly dependent on flow rate. A summary of the results achieved as well as some preliminary design parameters is given in Table VI.

Indicative adsorbent requirements for a plant treating 100 L/h of a waste stream containing approximately 100 mg/L Pd were generated assuming that:

Table V

Preliminary economic evaluation of Pt recovery from relevant low-grade streams via ion exchange technology

Recovery	
Pt per year (generated from waste), kg	240
Value of Pt recovered, US\$	10 996 320
Loading by adsorbent, Pt g/kg	177
Typical residence time, min	2-6
Cost	
Price of ion exchanger, US\$/kg	60
Adsorbent inventory per year, kg	1356
US\$/year	81 360
% adsorbent vs metal recovered cost	0.7

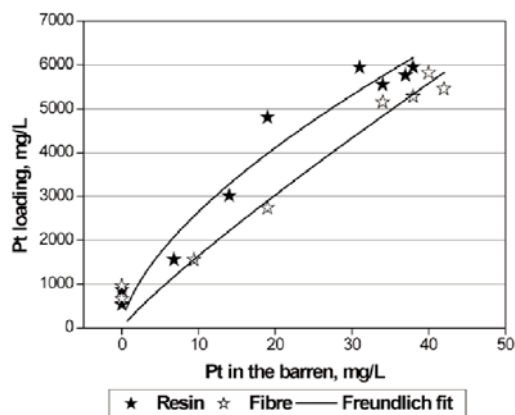


Figure 9—Platinum equilibrium adsorption isotherms for the Mixed Waste stream

Ion exchange technology for the efficient recovery of precious metals from waste

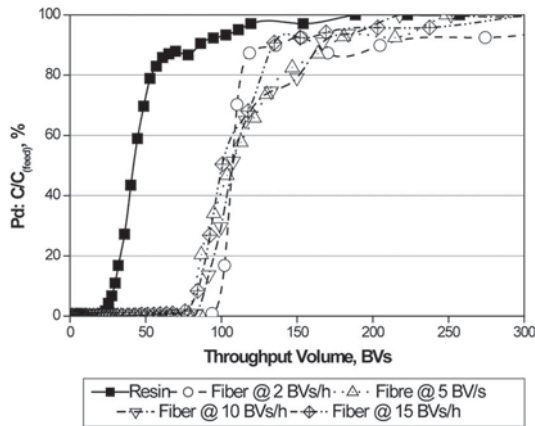


Figure 10—Palladium breakthrough profiles

Table VI						
Pd breakthrough profiles						
Parameter		Resin		Fibre		
Flow rate	BV/h	2	2	5	10	15
	cm/min	0.65	0.65	1.6	3.2	4.9
BV @ 1 mg/L breakthrough	BV	21	93	79	70	68
BV @ 80% breakthrough	BV	57	117	122	12	11
MTZ residence time	min	19	6	4	3	2
Pd loading	g/L	5.02	10.8	10.4	9.7	9.4
Pd upgrade		42	91	88	82	79
Pt co-loading	g/L	1.51	1.93	1.4	1.2	0.9
Sizing of full scale plant						
Feed flow rate	L/h	100	100	100	100	100
Pd flow rate	g/h	11.9	11.9	11.9	11.9	11.9
Adsorbent flow rate	L/h	2.4	1.1	1.1	1.2	1.3
Adsorbent for MTZ	L	37	11	7	5	3
Transfer	h	17.7	11.6	7.7	4.4	2.7

- Solution will be passed through a lead-lag column arrangement
- Once the resin/fibre in the first column reaches approximately 80% palladium breakthrough, the column will be removed from the system and the loaded adsorbent incinerated for Pd recovery
- A column containing fresh adsorbent will be placed in the lag position.

Treatment of the Pd Waste stream using IX resulted in effective palladium recovery (>99%) leaving <1 mg/L in the barren solution. Some co-loading of Pt was observed (Table VI), which might be beneficial for the specific application.

The fibre IX system would have the following advantages over a granular system:

- Higher Pd upgrade (>2 times), hence lower adsorbent flow rate
- The fibre column could be operated at about 95% breakthrough, hence closer to theoretical equilibrium, than the resin column, which would be operated at about 80% breakthrough

- Faster adsorption kinetics and hence significantly smaller inventory requirements;

Use of fibrous instead of granular ion exchange material for the treatment of the Pd Waste stream allowed a decrease in the size of the plant by >70%. Also in this specific case, the flow rate of fibre was approximately half that of resin, and hence the incineration costs would be significantly reduced. Fibres are generally more expensive than granular resins (mass basis), hence a cost comparison would have to be done to identify the most cost-effective option for a specific application. However, efficient elution employing a suitable reagent (HCl, thiourea, etc.) should make the recovery of Pd from low-grade or waste streams using ion exchange technology highly attractive.

Mixed Waste solution: breakthrough

Results for the recovery of Pt from the Mixed Waste solution (Table IV) using Adsorbent 1, in the fibrous and granular forms, are presented in Figure 11. Results and some preliminary design parameters are listed in Table VII.

Both fibre and resin were effective for the recovery of Pt from the Mixed Waste stream. The loaded adsorbents contained primarily Pt and some Rh. The ratios of Pt to Rh in the feed liquor and on the loaded ion exchangers were similar, indicating that Adsorbent 1 was effective for the simultaneous recovery of Pt and Rh, as the selectivity coefficients for Pt over Rh were about 1.

Similar final Pt loadings of 8.4–8.9 g/L were achieved with the fibre and resin. However, for a full-scale plant treating about 100 L/h of waste containing approximately 50 mg/L Pt, the plant using fibre could be > 40% smaller than the equivalent granular ion exchange plant.

Recovery of all the PGMs from the Mixed Waste solution by using an exchanger with a TETA type of adsorbent was ineffective. Potentially, it is possible to improve recovery of the Pd, Ir, and Ru by introducing another type or types of ion exchange materials into the treatment sequence. Also, an efficient elution procedure must be developed for the recycling of the adsorbents to make the process economically viable for such types of streams.

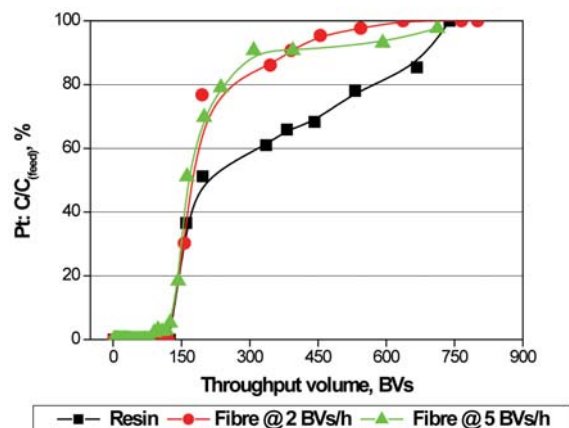


Figure 11—Platinum breakthrough profiles achieved with adsorbent 1: Mixed Waste

Ion exchange technology for the efficient recovery of precious metals from waste

Table VII

Results of breakthrough tests for Pt recovery from the Mixed Waste stream

Parameter		Adsorbent		
		Resin	Fibre	
Flowrate	BV/h	2	2	5
	cm/min	0.65	0.65	1.6
BV @ 0.1 mg/L breakthrough	BV	124	158	90
BV@ 80% breakthrough	BV	538	300	237
MTZ residence time	min	23	14	7
Pt loading	g/L	8.9	8.5	8.4
Pt upgrade		211	202	200
Rh co-loading	g/L	1.3	2.1	1.2
Rh upgrade		185	300	171
Preliminary sizing of full-scale plant				
Feed flow rate	L/h	100		
Pt flow rate	g/h	4.3	4.3	4.3
Adsorbent flow rate	L/h	0.48	0.51	0.51
Adsorbent for MTZ	L	38	24	12
Transfer	h	80	47	24

Conclusions

Evaluation of ion exchange technology for the recovery of precious metals from low grade or waste streams indicated that:

- It was possible to decrease the PGM tenor in the effluent streams to <1 mg/L
- Commercially available ion exchange materials with triethyltetramine and tributylamine functional groups were found to be suitable for recovery of Pt, Rh, and Pd respectively with high upgrade ratios
- Pt-selective resins/fibres were capable of loading up to 17% platinum with the cost of direct incineration of materials loaded in some cases being less than 1% of the value of the metals recovered.

Optimization of adsorption parameters and further conditioning of the low-grade liquor prior to contact with ion exchange material might improve upgrades and maximum loadings of the PGMs.

Two types of ion exchange materials, fibrous and granular, were evaluated. It was concluded that in spite of the fact that fibrous ion exchangers are generally more expensive (approximately 25%) than granular ones, they can improve economics of the waste treatment as:

- In some cases they have higher selectivity for a valuable metal and higher operating capacity
- Due to faster reaction rates, the size of the adsorption unit and, hence, overall treatment plant footprint could be much smaller compared with a resin plant
- The benefits for application of fibrous ion exchange instead of granular material should be quantified and evaluated for each specific case
- Elution instead of incineration might increase the benefits of fibrous materials over granular ones for the waste treatment sequence.

Before designing a process to treat a given PGM waste or low-grade stream, laboratory studies should be performed to optimize the choice of resin, elution system, and operating parameters. In order to do this, it is essential that the chemistry of the metals in the waste stream be understood.

References

- ANONYMOUS. Not dated. Equilibriums in solutions of palladium chloride
http://www.chemweek.ru/sobitiya/Ravnovesiya_v_rastvorah_kompleksnyh_hloridov_palladiya.htm [in Russian]. [Accessed 12 March 2014].
- BERNARDIS, F.L., GRANT, R.A., and SHERRINGTON, D.C. 2005. A review of methods of separation of the platinum-group metals through their chloro-complexes. *Reactive and Functional Polymers*, vol. 65. pp. 205–217.
- BOEHM, D.R. and HAMPEL, K.R. 1972. Recovery of palladium from rinse water. US patent 3656939. Gulf & Western Ind. Prod. Co. Publ. 18 Apr.. 1972.
- BORG, R.J., FRANKE, A.A., NERVIK, W.E., and STEVENSON, P.C. 1955. A method of separating certain platinum group metals with cation exchange resins. US patent 2714555. Publ. 2 Aug. 1955.
- DANKS, M. Not dated. Smopex® fibres for metal recovery.
<http://www.docstoc.com/docs/114085582/Smopex-%EF%BF%BD-Fibres-For-Metal-Recovery>
- GINZBURG, S.I., EZERSKAYA, N.A., PROKOF'eva, I.V., FEDORENSKO, N.V., SCHLENSKAYA, V.I., and BEL'SKII, N.K. 1975. Analytical Chemistry of Platinum Metals. Translated by N. Kaner. Shnelnitz, P. (ed.). John Wiley & Sons, New York.
- Hubicki, Z., Leszczyńska, M., Łodyga, B., and Łodyga, A. 2006. Palladium (II) removal from chloride and chloride-nitrate solutions by chelating ion-exchangers containing N-donor atoms. *Minerals Engineering*, vol. 19. pp. 1341–1347.
- IZATT, S.R., BRUENING, R.L., and IZATT, N.E. 2012. Some applications of molecular recognition technology (MRT) to the mining industry. *T.T. Chen Honorary Symposium on Hydrometallurgy, Electrometallurgy and Materials Characterisation*. Wang, S., Dutrizac, J.E., Free, M.L., Hwang, J.Y., and Kim, D. (eds.). TMS, Warrendale, PA. pp. 51–63.
- KLOOPER, R. 2006. An investigation into the complex formation and potential solvent extraction of Os(IV/III) with N,N-dialkyl-N'-acryl(aroyl)thioureas. Magister Scientie thesis, University of Stellenbosch.
- KORKISCH, J. 2000. Handbook of Ion Exchange Resins: Their Application to Inorganic Analytical Chemistry. Vol. III. Platinum Metals. CRC Press, Boca Raton, FL 288 pp.
- SOLDATOV, V.S. 2008. Syntheses and the main properties of fibrous ion exchangers. *Solvent Extraction And Ion Exchange*, vol. 26. pp. 457–513.
- YAHORAVA, V., KOTZE, M., and AUERSWALD, D. 2013. Evaluation of different adsorbents for copper removal from cobalt electrolyte. Seventh Southern African Base Metals Conference, White River, Mpumalanga, South Africa, 2–6 September 2013. *The Southern African Institute of Mining and Metallurgy*, Johannesburg. pp. 283–298.
- ZAGANARIS, E.J. 2009. Ion Exchange Resins in Uranium Hydrometallurgy. Books On Demand, Stoughton, WI. p. 200. ◆

Air Liquide - Improving gold recovery through local expertise



ALDOC

Air Liquide is a leading innovator in the application of gases to assist the metallurgy industry.

The development of the **ALDOC** system for leaching gold leads to improved efficiencies, reduction in costs and a boost in profits.

ALDOC facilitates, monitors and controls the oxygen in cyanidation tanks with an efficient injection system that delivers flow-rate, purity, pressure, uptime and Dissolved Oxygen. Air Liquide has been developing the right technology for the mining and metallurgy industry for years and is a world leader in industrial gases.

AIR LIQUIDE'S summary of benefits

- Reduced Process Cost
- Quality
- Service
- Reduced Cyanide Consumptions
- Improved Kinetics
- Improved Recoveries

Air Liquide Southern Africa
Tel: +2711 389 7000, Kobus Durand (Metallurgy Manager) +2711 389 7377
www.airliquide.co.za

There is an Air Liquide solution that is right for you.

BACKGROUND

The primary method of production and rock breaking in the South African mining industry is drilling and blasting. This method of rock breaking has been subjected to continuous improvement both with regard to the technological applied and the practices followed.

To maximize the benefits offered by these new technologies and techniques, it is necessary to review the basic theory of rock breaking, blast design and drilling technology. Specialized blasting techniques and optimization drilling and blasting will be covered. Best practices will be dealt with and case studies considered illustrating practically how to achieve the greatest benefit.

Emphasis will be placed on the integration of drilling and blasting into the broader mine to mill value chain, in order to reach a true economic optimum for the total mining process.

For further information contact:

Head of Conferencing, Raymond van der Berg
SAIMM, P O Box 61127, Marshalltown 2107
Tel: (011) 834-1273/7 · Fax: (011) 833-8156 or
(011) 838-5923 · E-mail: raymond@saimm.co.za
Website: www.saimm.co.za



SCHOOL

Drilling and Blasting

19-20 May 2014

Swakopmund Hotel & Entertainment Centre, Swakopmund, Namibia

WHO SHOULD ATTEND

- Academics
- Accounts managers
- Blasters
- Blasting specialists
- Business line managers
- Consultants
- Contract managers
- Conversion engineers
- Drill & blast engineers
- Drill & blast superintendents
- Drill & blast supervisors
- Engineers
- Explosives engineers
- General managers
- Geotechnical engineers
- Mine managers
- Mine planners
- Mining engineers
- Operations managers
- Product managers
- Production engineers
- Project engineers
- Project managers
- Rock engineers
- Surveyors
- Technical co-ordinators
- Technical representatives



Synthesis and crystal structure of tetrakis(1,3-diphenyl-1,3-propanedionato) zirconium(IV)

by M. Steyn*, H.G. Visser*, and A. Roodt*

Synopsis

The coordination compound *tetrakis*(1,3-diphenyl-1,3-propanedionato)zirconium(IV), $[\text{Zr}(\text{DBM})_4]$, (DBM = dibenzoyl methane/1,3-diphenyl-1,3-propanedionol) was synthesized and characterized by single-crystal X-ray diffraction. $[\text{Zr}(\text{DBM})_4]$ crystallizes in the monoclinic space group $P2_1/c$ ($a = 24.769(4)$ Å, $b = 10.216(5)$ Å, $c = 19.314(4)$ Å, and $\beta = 101.541(5)^\circ$). The coordination geometry around the zirconium atom, formed by the eight O-donating atoms of the four β -diketonates, is found to be a near-perfect square antiprism. Crystal packing is stabilized by C—H $\cdots\pi$ interactions throughout the crystal lattice. This structure is a noteworthy example of the application of ambient condition synthesis of zirconium compounds in N,N'-dimethylformamide (DMF) as reaction and crystallization solvent, highlighting the possibilities of aerobic condition metal purification through chelation.

Keywords

zirconium, β -diketone, square-antiprismatic coordination polyhedron.

Introduction

Zirconium and its organometallic complexes have featured in a wide range of research studies for several years (Hoard and Silverton, 1963; Von Dreele, Stezowski, and Fay, 1971; Clegg, 1987; Calderazzo *et al.*, 1998). Zirconium, with its very low affinity for thermal neutrons (radioactive energy), high thermal stability, and exceptional anti-corrosive properties, is widely used as cladding material for nuclear reactor fuel rods (Weast, 1982). Purification of zirconium from its minerals is known to be a laborious task, broadly utilizing dangerous acids and highly hazardous thermal conditions (Lowe and Parry, 1976; Nielsen, Schlewitz, and Nielsen, 2000; Speight, 2010).

The purification method that appears to be a significant point of interest in certain literature fields (Smolik, Jakobik-Kolon, and Poranski, 2009; Taghizadeh *et al.*, 2009; Taghizadeh, Ghanadi, and Zolfonoun, 2011) is ion exchange purification – a method that involves the filtering of specific metal oxides through acidification processes along ion-exchange columns (Benedict, Schumb, and Coryell, 1954; Machlan and Hague, 1962;

Qureshi and Husain, 1971). The main principles of organometallic compound behaviour in both solid state and solution are of substantial interest when considering the design of newer variations of such ion exchange purification methods.

As part of an ongoing study investigating coordination behaviour of O,O'- and N,O-bidentate ligands with zirconium(IV) and hafnium(IV) for possible influencing factors in the purification of these metals from base ore sources, we have been able to refine methods of synthesis and crystallization of zirconium complexes. This is in particular as a reference and a comparison with much older methods and results reported or published in the literature. In this paper we describe and elaborate on the synthesis and crystallographic characterization of the structure [*tetrakis*(1,3-diphenyl-1,3-propanedionato)-zirconium(IV)] as a redetermination and comparison to a previously published structure (Chun, Steffen, and Fay, 1979), and as a comparison to the hafnium(IV) counterpart (Viljoen, Visser, and Roodt, 2010).

The intimate geometric properties in the immediate coordination sphere of the Zr(IV) metallic molecule are essentially reproduced here, but with correspondingly elaborative statistical implication, indicating that the susceptibility of chelation geometry to intermolecular forces is greater than that of ligand internal geometry, as also previously published for the standard *tetrakis*(acetylacetonato)zirconium(IV) ($[\text{Zr}(\text{acac})_4]$) structure (Clegg, 1987).

A schematic of $\text{Zr}(\text{DBM})_4$ is shown in Figure 1.

* Department of Chemical, University of the Free State, Bloemfontein, South Africa..

© The Southern African Institute of Mining and Metallurgy, 2014. ISSN 2225-6253. This paper was first presented at the, Precious Metals 2013 Conference, 14–16 October 2013, Protea Hotel, President, Cape Town, South Africa.

Synthesis and crystal structure of tetrakis(1,3-diphenyl-1,3-propanedionato)

Experimental

Materials and instruments

All the starting chemicals and solvents were of analytical grade, commercially purchased and used without further purification. Synthesis was conducted under ambient laboratory conditions. All ^1H NMR spectra were obtained in acetone- d_6 on a Bruker 300 MHz nuclear magnetic resonance spectrometer.

Synthesis of $[\text{Zr}(\text{DBM})_4]$

ZrCl_4 (101.2 mg, 0.434 mmol) and dibenzoylmethane (DBM)

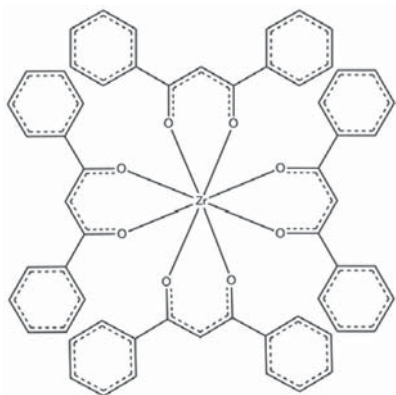


Figure 1—Schematic representation of the title compound, tetrakis(1,3-diphenyl-1,3-propanedionato)zirconium(IV) - $[\text{Zr}(\text{DBM})_4]$

(396.6 mg, 1.769 mmol) were separately dissolved in DMF (10 ml each) and heated to 60°C . The DBM solution was added dropwise to the zirconium solution and stirred at 60°C for 30 minutes. The reaction solution was removed from heating, covered and left to stand for crystallization.

Colourless trapezoidal crystals, suitable for single-crystal X-ray diffraction, formed after 21 days. (Yield: 382 mg, 88%). ^1H NMR (300 MHz, acetone- d_6): δ = 9.04 (dd, 1H), 8.13 (dd, 1H), 7.72 (q, 1H), 7.62 (s, 1H).

X-ray crystal structure determination

The X-ray intensity data was collected on a Bruker X8 ApexII 4K Kappa CCD area detector diffractometer, equipped with a graphite monochromator and $\text{MoK}\alpha$ fine-focus sealed tube ($\lambda = 0.71069 \text{ \AA}$, $T = 100(2) \text{ K}$) operated at 2.0 kW (50 kV, 40 mA). The initial unit cell determinations and data collections were done by the SMART software package (Bruker, 1998a). The collected frames were integrated using a narrow-frame integration algorithm and reduced with the Bruker SAINT-Plus and XPREP software packages (Bruker, 1999) respectively. Analysis of the data showed no significant decay during the data collection. Data was corrected for absorption effects using the multi-scan technique SADABS (Bruker, 1998b), and the structure was solved by the direct methods package SIR97 (Altomare *et al.*, 1999) and refined using the WinGX software (Farrugia, 1999) incorporating SHELXL (Sheldrick, 1997). The final anisotropic full-matrix least-squares refinement was done on F^2 . The aromatic protons were placed in geometrically idealized positions ($\text{C-H} = 0.93 - 0.98 \text{ \AA}$) and constrained to ride on their parent atoms with $U_{\text{iso}}(\text{H}) = 1.2U_{\text{eq}}(\text{C})$. Non-hydrogen atoms were refined with

Table 1	
Crystallographic and refinement details for the title compound	
Crystal formula	$[\text{Zr}(\text{DBM})_4]$
Empirical formula	$\text{C}_{60} \text{H}_{44} \text{O}_8 \text{Zr}$
Formula weight ($\text{g}\cdot\text{mol}^{-1}$)	984.17
Crystal system, space group	Monoclinic, $P2_1/c$
Unit cell dimensions:	
a, b, c (\AA)	24.769(4), 10.216(5), 19.314(4)
α , β , γ ($^\circ$)	90.000, 101.541(5), 90.000
Volume (\AA^3), Z	4788(3), 4
Density (calculated, $\text{mg}\cdot\text{cm}^{-3}$)	1.365
Crystal morphology	trapezoid
Crystal colour	colourless
Crystal size (mm)	0.792 x 0.630 x 0.331
Absorption coefficient μ (mm^{-1})	0.288
F(000)	2032
Theta range	1.68 to 28.00
Index ranges	$-32 \leq h \leq 32$ $-13 \leq k \leq 13$ $-25 \leq l \leq 25$
Reflections collected,	88438, 11558, 0.0303
Independent reflections, R_{int}	
Completeness to 2θ ($^\circ$, %)	28.00, 100.0
Max. and min. transmission	0.9110 and 0.8044
Data, restraints, parameters	11558, 0, 622
Goodness-of-fit on F^2	1.023
Final R indices [$I > 2\sigma(I)$]	$R_1 = 0.0279$ $wR_2 = 0.0665$
R indices (all data)	$R_1 = 0.0333$ $wR_2 = 0.0700$
Largest diff. peak and hole ($\text{e}\cdot\text{\AA}^{-3}$)	0.407 and -0.529

Synthesis and crystal structure of tetrakis(1,3-diphenyl-1,3-propanedionato)

anisotropic displacement parameters. The graphics were obtained with the DIAMOND program (Brandenburg and Putz, 2006) with 50% probability ellipsoids for all non-hydrogen atoms.

Results and discussion

Most literature reports on the synthesis of zirconium(IV) compounds with β -diketones, and most reports on work in which where N- and O-donating bidentate ligands were used emphasize the importance of working under anaerobic conditions employing Schlenk-type apparatus. This is of course not viable in industrial applications like the purification of metal ores by organometallic reactions. The synthesis of $[\text{Zr}(\text{DBM})_4]$ in DMF under aerobic conditions opens up new possibilities in the rich coordination chemistry of zirconium complexes.

The title compound, $[\text{Zr}(\text{DBM})_4]$, crystallizes in the monoclinic space group, $P2_1/c$. The asymmetric unit consists of a Zr(IV) metal ion coordinated to four unique, bidentate, oxygen-donating, β -diketonato ligands. The molecular structure of the title compound is represented in Figure 2 together with the atom numbering scheme. General crystallographic details are presented in Table I, while selected bond lengths, bond angles, and torsion angles are listed in Table II.

In this structure the Zr—O bond distances range from 2.141(1) Å to 2.2125(1) Å while the average O—Zr—O bite angle is $74.53(4)^\circ$ (Table II). The four DBM-ligands are arranged around the metal centre in a space-filling, fan-like arrangement to give a square-antiprismatic coordination polyhedron (Figure 3a), with an almost negligible outward distortion towards dodecahedral geometry. This distortion of the ideal square antiprism lies with an outward bend of $3.71(4)^\circ$, as illustrated in Figure 3b.

A noteworthy characteristic of the zirconium metal centre is observed in this structure, in that it distorts the backbone

of the bidentate (acac-type) ligands from its preferred coordination geometry of approx. 180° towards a highly distorted bent-like geometry to accommodate the overall polyhedron geometry around the metal centre. These ligands are chelated around the metal centre with a bend in the ligand at the intersection of the two planes formed by the ligand-backbone (O—C—C—O) and the O—Zr—O bite angle (Figure 4). The extent of this ligand distortion ranges from $16.64(5)$ to $25.76(4)^\circ$.

The ligand backbone itself also displays a twisting/bending in the arrangement of each individual phenyl ring at the edges of the C—C—C-backbone. Each

Table II

Selected geometric parameters for $[\text{Zr}(\text{DBM})_4]$

Selected bond lengths (Å)			
Zr—O ₁	2.1405 (11)	C ₀₁ —C ₁₀₁	1.4937 (17)
Zr—O ₂	2.2069 (12)	C ₀₃ —C ₂₀₁	1.4881 (17)
Zr—O ₃	2.1904 (10)	C ₀₄ —C ₃₀₁	1.4896 (19)
Zr—O ₄	2.1621 (10)	C ₀₆ —C ₄₀₁	1.4981 (18)
Zr—O ₅	2.1578 (10)	C ₀₇ —C ₅₀₁	1.4904 (18)
Zr—O ₆	2.2014 (13)	C ₀₉ —C ₆₀₁	1.4912 (19)
Zr—O ₇	2.2125 (11)	C ₁₀ —C ₇₀₁	1.4957 (18)
Zr—O ₈	2.1517 (10)	C ₁₂ —C ₈₀₁	1.4921 (18)
Selected bond angles (°)			
O ₁ —Zr—O ₂	74.91 (4)	O ₅ —Zr—O ₆	74.59 (4)
O ₃ —Zr—O ₄	74.53 (4)	O ₇ —Zr—O ₈	74.10 (4)
Selected torsion angles (°)			
O ₁ —C ₀₁ —C ₀₃ —O ₂	6.02(11)	O ₅ —C ₀₇ —C ₀₉ —O ₆	10.98(11)
O ₃ —C ₀₄ —C ₀₆ —O ₄	-1.39(11)	O ₇ —C ₁₀ —C ₁₂ —O ₈	-1.54(11)

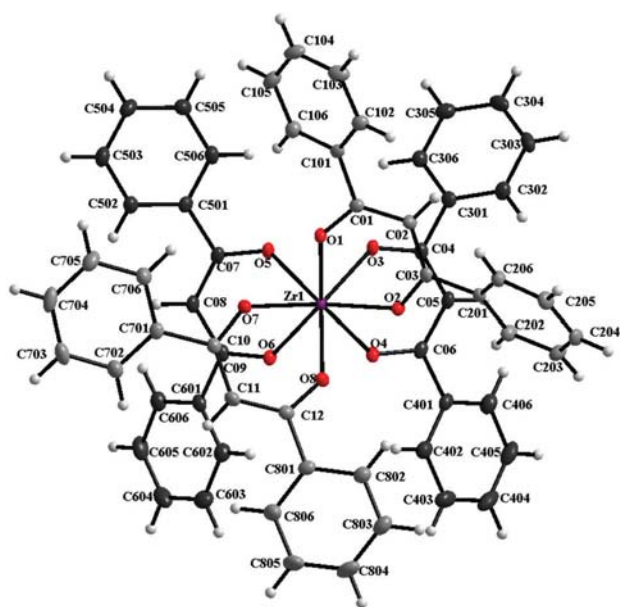


Figure 2—Graphic illustration of $[\text{Zr}(\text{DBM})_4]$ showing general numbering of atoms. Displacement ellipsoids drawn at 50% probability. Numbering of phenyl groups denoted by C_n where n=1-8

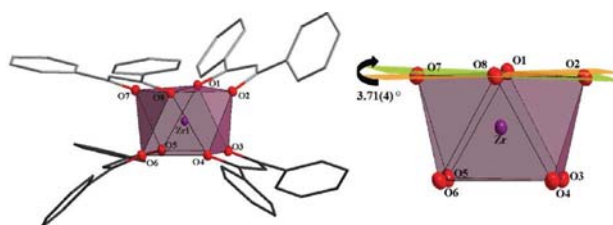


Figure 3—Graphic illustration of the square-antiprismatic coordination polyhedron of $[\text{Zr}(\text{DBM})_4]$. (Left) Side view showing upper and lower four corners represented by the O-coordinating atoms of the ligands; (Right) Illustration of square-antiprismatic coordination polyhedron distortion, showing the outward bend of the topmost atoms

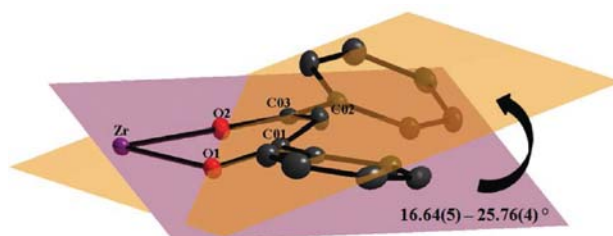


Figure 4—Illustration of ligand bending as found in the title compound. The two planes intersect at the O, O'-coordination site

Synthesis and crystal structure of tetrakis(1,3-diphenyl-1,3-propanedionato)

Table III

Selected dihedral angles for phenyl swivelling on individual DBM ligands as observed in the title compound

Phenyl-to-ligand swivel (Figure 5a)		
Atoms in plane		Dihedral angles (°)
O ₁ —CCC—O ₂	Ph ₁	25.61(4)
O ₁ —CCC—O ₂	Ph ₂	38.12(4)
O ₃ —CCC—O ₄	Ph ₄	22.27(6)
O ₃ —CCC—O ₄	Ph ₃	43.76(4)
O ₅ —CCC—O ₆	Ph ₆	27.05(4)
O ₅ —CCC—O ₆	Ph ₅	30.43(5)
O ₇ —CCC—O ₈	Ph ₇	20.36(5)
O ₇ —CCC—O ₈	Ph ₈	20.73(4)

Phenyl-to-phenyl swivel (Figure 5b)		
Atoms in plane		Dihedral angles (°)
Ph ₁	Ph ₂	21.59(4)
Ph ₃	Ph ₄	60.20(5)
Ph ₅	Ph ₆	57.20(5)
Ph ₇	Ph ₈	25.54(5)

individual Ph ring is swivelled at a distinct angle (see Table III) with respect to its parent β -diketone structural plane (Figure 5a), ranging from 20.36(5) to 43.76(4)°. Furthermore, the angle at which each phenyl pair are swivelled away from each other over the β -diketone structural plane ranges from 21.59(4) to 60.20(5)° (Figure 5b). This planar swivelling found for each individual phenyl ring is directly related to the manner in which the crystal lattice packing is arranged, as described below.

The compound itself packs in two observable ways in the lattice as a whole. Firstly, every organometallic molecule packs on top of another in a head-to-tail fashion along the c -axis, and head-to-head along the a -axis, as illustrated in Figure 6. Secondly, the most significant packing effect observed is a C—H \cdots π interaction network, rigidly threading the entire crystal lattice together as a whole. This elaborate C—H \cdots π interaction system found in the title compound is the cause for the unique swivelling of each individual phenyl ring on each DBM ligand.

The effect of this best described, as illustrated in Figure 7, as a 'cross-stitching' and 'threading' effect in the channelling of the head-to-tail packing along the c -axis in the crystal lattice. On one side of the stacked molecules, with a rigid 'cross-stitching' of the C—H \cdots π interactions of Ph₁, Ph₃, and Ph₅ (listed in Table IV), an intricate lattice assemblage of the symmetrically identical groups interacting and packing on their respective neighbours is observed. On the other side of the head-to-tail packed molecules, Ph₂ and Ph₄ show a looser, but still significant 'threading' in their symmetrically placed neighbours (Figure 7b). This intricate network of C—H \cdots π interactions gives rise to the fact that no solvent molecules are caught inside the crystal lattice.

Although there are no classical hydrogen bonding or π - π stacking interactions, there is a weak intermolecular C—H \cdots O interaction between C₂₀₅—H₂₀₅ of the Ph₂ and an oxygen atom, O₄, on a neighbouring molecule (listed in Table V).

Furthermore, this very stable arrangement of the organometallic molecules as a whole leads to two notable observations with regards to the nature of solid-state behaviour of zirconium and its β -diketone chelated compounds. Firstly, it is a well-known fact that zirconium β -diketone complexes in general always show a square-antiprismatic coordination polyhedron (Hoard and Silverton,

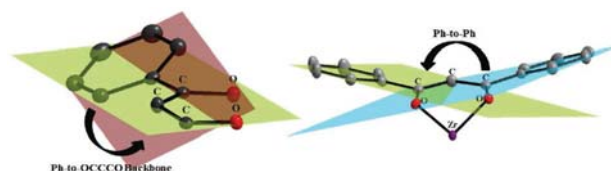


Figure 5—Illustration of ligand phenyl-group swivelling as found in the title compound. (Left) Swivel of the phenyl with regard to the parent backbone; (right) phenyl swivel in the DBM ligand structure - phenyl-to-phenyl plane swivel

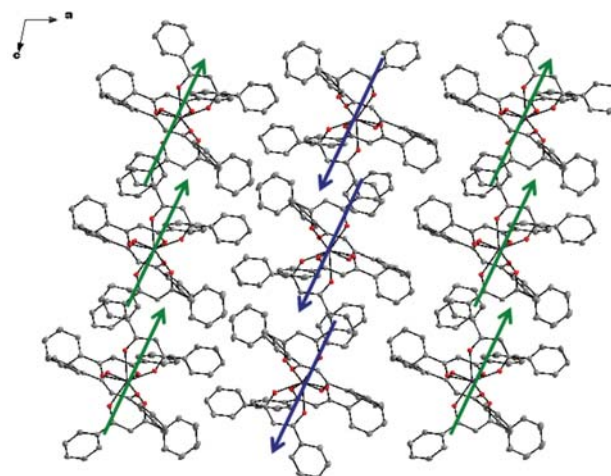


Figure 6—Graphical representation of molecular packing within the unit cell for the title compound, showing head-to-tail packing along the c -axis (arrow direction) and head-to-head packing along the a -axis (alternating green and blue arrows). Hydrogen atoms omitted for clarity, 50% probability displacement ellipsoids

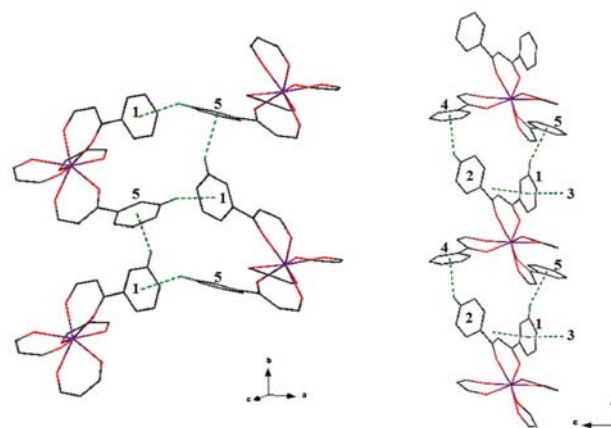


Figure 7—Illustration of C—H \cdots π interactions found in the title compound. (Left) as viewed along the b -axis, depicting the 'cross-stitching' of Ph₁ and Ph₅; (right) showing the 'threading' of Ph₂ and Ph₄, with Ph₁/Ph₃/Ph₅ in the background, showing the entire network of C—H \cdots π interactions found in lattice

Synthesis and crystal structure of tetrakis(1,3-diphenyl-1,3-propanedionato)

Table IV

Selected C-H...Cg (pi-ring) interactions (H...Cg < 3.0 Å, gamma < 30.0°) as observed in the title compound. H-perp represents the perpendicular distance of H to Phring plane; X-H, Pi represents the angle of the X-H bond to Pi-plane (perpendicular=90°, parallel = 0°)

X-H...Cg	H...Cg (Å)	H-perp (Å)	Gamma (°)	X-H...Cg (°)	X...Cg (Å)	X-H, Pi
C ₂₀₅ -H ₂₀₅ ...Ph ₅ ⁱ	2.73	2.708	5.27	149	3.556(2)	60
C ₂₀₄ -H ₂₀₄ ...Ph ₄ ⁱ	2.83	2.821	3.93	141	3.602(2)	55
C ₃₀₄ -H ₃₀₄ ...Ph ₁ ⁱⁱ	2.65	2.639	5.52	154	3.513(2)	62
C ₅₀₅ -H ₅₀₅ ...Ph ₁ ⁱⁱⁱ	2.77	2.699	12.78	145	3.568(2)	58

Symmetry codes: (i) x, -1+y, z; (ii) x, 1/2-y, -1/2+z; (iii) 1-x, 1/2+y, 1/2-z

1963; Clegg, 1987). This suggests that zirconium has a certain preference for the chelation sites of the coordinating atoms, regardless of the steric properties of the ligands as a whole (Steyn, Roodt, and Steyl, 2008; Steyn *et al.*, 2011; Steyn, Visser, and Roodt, 2012, 2013). However, the packing of each individual zirconium bidentate-ligand complex seems to be governed largely by the stabilization of the ligands themselves, and not from any discernable effect from the metal centre. This, in theory, could be due mainly to the fact that zirconium(IV) tends towards a maximum state of coordination, as preference, or as lowest crystallization state. This is in accordance with what is expected in these symbiotic systems (Huheey, Keiter, and Keiter, 1993).

In other words, since the metal centre is entirely surrounded by the specific bidentate ligands coordinated, it

has no influence on the packing of the organometallic molecule in the greater crystal lattice, but only influences the placement of the coordinating atoms around itself, thereby not allowing for dimeric structures or other metal-to-linking-atom interactions.

As far as the physical structural characteristics of this tetrakis(β -diketone) zirconium(IV) complex are concerned, all aspects are in good comparison to other published structures containing β -diketone ligands (Table VI). All coordination bond lengths are in the average range of 2.1–2.2 Å and bite angles average the standard angle of 74–75°. Furthermore, it is interesting to note that all these fully coordinated zirconium(IV) β -diketonates appear to prefer a monoclinic space group across the board. Finally, in comparison to the previously published structure (Chun, Steffen, and Fay, 1979), although the asymmetric unit appears identical and all structural characteristics are comparable (Table V), these two crystals are not completely identical. When comparing the smaller crystallographic cell volume for the title compound to that reported by Chun, Steffen, and Fay, there does appear to be a tighter packing of the crystal lattice here.

Regardless of the final crystallographic findings, however, it is significant to note that Chun, Steffen, and Fay reported a synthetic procedure of phosphite-catalysed reflux

Table V

Hydrogen bond geometry in the title compound

D-H...A	D-H (Å)	H...A (Å)	D...A (Å)	D-H...A (°)
C ₂₀₅ -H ₂₀₅ ...O ₄ ⁱ	0.93	2.6	3.512 (2)	169

Symmetry code: (i) x, y-1, z

Table VI

Selected crystallographic characteristics, bond lengths and angles of zirconium(IV) β -diketonates

	[Zr(DBM) ₄] ^a	[Zr(DBM) ₄] ^b	[Hf(DBM) ₄] ^c	[Zr(tFAcac) ₄] ^d	[Zr(hFAcac) ₄] ^d	[Zr(Acac) ₄] ^e
Empirical formula	C ₆₀ H ₄₄ O ₈ Zr	C ₆₀ H ₄₄ O ₈ Zr	C ₆₀ H ₄₄ O ₈ Hf	C ₂₀ H ₁₆ F ₁₂ O ₈ Zr	C ₂₀ H ₄ F ₂₄ O ₈ Zr	C ₂₀ H ₂₈ O ₈ Zr
Formula weight (g.mol ⁻¹)	984.17	984.22	1071.44	703.55	919.45	487.7
Crystal system, Space group	Monoclinic, P2 ₁ /c	Monoclinic, P2 ₁ /c	Monoclinic, P2 ₁ /c	Monoclinic, C2/c	Monoclinic, P2 ₁ /c	Monoclinic, C2/c
Unit cell dimensions: a, b, c (Å)	24.769(4), 10.216(5), 19.314(4)	25.241(5), 10.324(1), 19.395(4)	24.846(2), 10.224(8), 19.316(1)	21.506(2), 7.951(5), 16.051(1)	15.353(1), 20.261(2), 19.698(2)	21.662(2), 8.360(1), 14.107(1)
β (°)	101.541(5)	101.72(1)	101.618(4)	113.736(4)	95.828(2)	116.708(6)
Volume (Å ³), Z	4788(3), 2.8	4 4948, 7.2	4 4806(6), 3.7	4 628.13(3), 4.7	4 762.0(2), 7.8	4 2282.1, 4 2
Average Zr—O (Å)	2.178(1)	2.171(5)	2.169(2)	2.189(2)	2.177(4)	2.188(1)
Shortest Zr—O (Å)	2.141(1)	2.1395(2)	2.133(2)	2.165(2)	2.141(4)	2.176(1)
Longest Zr—O (Å)	2.213(1)	2.2052(5)	2.200(2)	2.210(2)	2.225(4)	2.201(1)
Average Ox—Zr—Oy (°)	74.53(4)	74.63(2)	74.74(9)	74.37(8)	74.58(2)	74.85(1)

^aThis work ^bChun, Steffen, and Fay, 1979 ^cViljoen, Visser, and Roodt, 2010 ^dZherikova *et al.*, 2005 ^eClegg, 1987

Synthesis and crystal structure of tetrakis(1,3-diphenyl-1,3-propanedionato)

in diethyl ether and crystallization method of benzene/hexane extraction after vigorous purification of the reaction solution, for producing these specific crystals. This methodology in itself was most likely employed merely as a laboratory standard, but we can now report, with a certain amount of confidence, that zirconium as a metal reagent is more reactive than may have been expected in the past 30 years.

These rigorous synthesis methods and laborious crystallization techniques are not always necessary. Organometallic chelation reactions of zirconium are often self-catalysed and crystallization can occur in ambient environments. Furthermore, application of DMF as a general solvent in all processes allows for less strict approaches to the impacts of hydration on the final product, since crystalline water could also be observed in some cases in the asymmetric unit, without any influence on the main metal-molecule as a whole (Steyn, Roodt, and Steyl, 2008).

Conclusions

The improved synthesis of Zr(IV) complexes with β -diketone ligands has been illustrated here with tetrakis(1,3-diphenyl-1,3-propanedionato)zirconium(IV). It is shown that the intimate geometry around the metal atom seems to be governed largely by zirconium itself. A preference for square-antiprismatic coordination polyhedra for many O,O'- and N,O-bidentate ligand complexes across the board seem to indicate this fact (Chun, Steffen, and Fay, 1979; Viljoen, Visser, and Roodt, 2010; Steyn, Roodt, and Steyl, 2008; Steyn *et al.*, 2011; Steyn, Visser, and Roodt, 2012, 2013). The ligand geometries do, however, play a vital role in the stability of the crystal lattice as a whole. In the case of the title compound, which yielded very stable crystals in ambient conditions, the C—H... π interactions of most of the coordinated DBM ligands thread the entire crystal lattice into a very stable three-dimensional network.

Acknowledgement

Financial assistance from the Advanced Metals Initiative (AMI) of the Department of Science and Technology (DST) of South Africa, through the New Metals Development Network (NMDN) coordinated by the South African Nuclear Energy Corporation Limited (Necsa) is gratefully acknowledged.

We also express our gratitude towards SASOL, PETLabs Pharmaceuticals, and the University of the Free State Strategic Academic Initiative (Advanced Biomolecular Systems) for financial support of this research initiative outputs. This work is based on research supported in part by the National Research Foundation of South Africa (SANRF/THRIP; UIDs 71836 & 84913).

[†]Electronic supplementary information (ESI) and complete crystallographic detail in cif format are available on request.

References

- ALTOMARE, A., BURLA, M.C., CAMALLI, M., CASCARANO, G.L., GIACOVAZZO, C., GUAGLIARDI, A., MOLITERNI, A.G.G., POLIDORI, G., and SPAGNA, R. 1999. SIR97: a new tool for crystal structure determination and refinement. *Journal of Applied Crystallography*, vol. 32. pp. 115–119.
- BENEDICT, J.T., SCHUMB, W.C., and COREYLL, C.D. 1954. Distribution of zirconium and hafnium between cation-exchange resin and acid solutions. The column separation with nitric acid-citric acid mixture. *Journal of the American Chemical Society*, vol. 76, no. 8. pp. 2036–2040.
- BRANDENBURG, K. and PUTZ, H. 2006. DIAMOND, Release 3.0e, Crystal Impact GbR, Bonn, Germany.
- BRUKER AXS INC. 1998a. Bruker SMART-NT Version 5.050. Area-Detector Software Package. Madison, WI.
- BRUKER AXS INC. 1998b. Bruker SADABS Version 2004/1. Area Detector Absorption Correction Software. Madison, WI.
- BRUKER AXS INC. 1999. Bruker SAINT-Plus Version 6.02 (including XPREP), Area-Detector Integration Software. Madison, WI.
- CALDERAZZO, F., ENGLERT, U., MAICHLE-MÖSSMER, C., MARCHETTI, F., PAMPALONI, G., PETRONI, D., PINZINO, C., STRÄHLE, J., and TRIPEPI, G. 1998. Eight-coordinate chelate complexes of zirconium(IV) and niobium(IV): X-ray diffractometric and EPR investigations. *Inorganica Chimica Acta*, vol. 270, no. 1–2. pp. 177–188.
- CHUN, H.K., STEFFEN, W.L., and FAY, R.C. 1979. Effects of crystal packing on the coordination geometry of eight-coordinate metal chelates. Crystal and molecular structure of tetrakis(1,3-diphenyl-1,3-propanedionato) zirconium(IV). *Inorganic Chemistry*, vol. 18. pp. 2458–2465.
- CLEGG, W. 1987. Redetermination of the structure of tetrakis(acetylacetonato) zirconium(IV). *Acta Crystallographica C*, vol. 43. pp. 789–791.
- FARRUGIA, L.J. 1999. WinGX suite for small-molecule single-crystal crystallography. *Journal of Applied Crystallography*, vol. 32. pp. 837–838.
- HOARD, J.L. and SILVERTON, J.V. 1963. Stereochemistry of discrete eight-coordination. II. The crystal and molecular structure of zirconium(IV) acetylacetonate. *Inorganic Chemistry*, vol. 2. pp. 243–249.
- HUHEEY, J.E., KEITER, E.A., and KEITER, R.L. 1993. *Inorganic Chemistry - Principles of Structure and Reactivity*. 4th edn. HarperCollins College Publishers, New York.
- LOWE, A.L. and PARRY, G.W. (eds.). 1976. Zirconium in the Nuclear Industry: *Proceedings of the Third International Conference*, Quebec City, Canada, 10–12 August 1976. p.7. ASTM, Philadelphia, PA.
- MACHLAN, L.A. and HAGUE, J.L. 1962. Separation of hafnium from zirconium and their determination: separation by anion-exchange. *Journal of Research of the National Bureau of Standards*, vol. 66A, no. 6. pp. 517–520.
- NIELSEN, R.H., SCHLEWITZ, J.H., and NIELSEN, H. 2000. Zirconium and zirconium compounds. *Kirk-Othmer Encyclopedia of Chemical Technology*, vol. 26. John Wiley & Sons. pp. 630–631.
- QURESHI, M. and HUSAIN, K. 1971. Quantitative cation exchange separation of zirconium and hafnium in formic acid media. *Analytical Chemistry*, vol. 43. pp. 447–449.
- SHELDRIK, G.M. 1997. SHELXL97. Program for crystal structure refinement. University of Göttingen, Germany.
- SMOLIK, M., JAKOBIK-KOLON, A., and PORANSKI, M. 2009. Separation of zirconium and hafnium using Diphonix(R) chelating ion-exchange resin. *Hydrometallurgy*, vol. 95, no. 3–4. pp. 350–353.
- SPEIGHT, J.G. 2010. *The Refinery of the Future*. William Andrew, London. pp. 134–136.
- STEYN, M., ROODT, A., and STEYL, G. 2008. Tetrakis(1,1,1-trifluoroacetylacetonato-k2O,O')zirconium(IV) toluene solvate. *Acta Crystallographica*, vol. E64. p. m827.
- STEYN, M., VISSER, H.G., and ROODT, A. 2012. Tetrakis(5,7-dimethylquinolin-8-olato-2N,O)zirconium(IV) dimethylformamide disolvate. *Acta Crystallographica*, vol. E68. pp. m1344–m1345.
- STEYN, M., VISSER, H.G., and ROODT, A. 2013. Evaluation of oxine-type ligand coordination to zirconium(IV). *Journal of the Southern African Institute of Mining and Metallurgy*, vol. 113, no. 2. pp. 105–108.
- STEYN, M., VISSER, H.G., ROODT, A. and MULLER, T.J. 2011. Tetrakis(picolinato-2N,O)zirconium(IV) dehydrate. *Acta Crystallographica*, vol. E67. pp. m1240–m1241.
- TAGHIZADEH, M., GHANADI, M., and ZOLFONOUN, E. 2011. Separation of zirconium and hafnium by solvent extraction using mixture of TBP and Cyanex 923. *Journal of Nuclear Materials*, vol. 412. pp. 334–337.
- TAGHIZADEH, M., GHASEMZADEH, R., ASHRAFI-ZADEH, S.N., and GHANNADI, M. 2009. Stoichiometric relation for extraction of zirconium and hafnium from acidic nitrate solutions with Cyanex272. *Hydrometallurgy*, vol. 96. pp. 77–80.
- VILJOEN, J.A., VISSER, H.G., and ROODT, A. 2010. Tetrakis(1,3-diphenylpropane-1,3-dionato)hafnium(IV). *Acta Crystallographica*, vol. E66. pp. m1053–m1054.
- VON DREELE, R., STEZOWSKI, J.J., and FAY, R.C. 1971. Crystal and molecular structure of chlorotris(acetylacetonato)zirconium(IV). *Journal of the American Chemical Society*, vol. 93, no. 12. pp. 2887–2892.
- WEAST, R.C. 1982. *CRC Handbook of Chemistry and Physics*. 63rd edn. CRC Press, Boca Raton, FL.
- ZHERIKOVA, K.V., MOROZOVA, N.B., KURAT'eva, N.V., BAIDINA, I.A., STABNIKOV, P.A., and IGUMENOV, I.K. 2005. *Journal of Structural Chemistry*, vol. 46. pp. 513–522. ◆



SAIMM

THE SOUTHERN AFRICAN
INSTITUTE OF MINING AND
METALLURGY

Forthcoming SAIMM events...

For the past 120 years, the Southern African Institute of Mining and Metallurgy, has promoted technical excellence in the minerals industry. We strive to continuously stay at the cutting edge of new developments in the mining and metallurgy industry. The SAIMM acts as the corporate voice for the mining and metallurgy industry in the South African economy. We actively encourage contact and networking between members and the strengthening of ties. The SAIMM offers a variety of conferences that are designed to bring you technical knowledge and information of interest for the good of the industry. Here is a glimpse of the events we have lined up for 2013. Visit our website for more information.

EXHIBITS/SPONSORSHIP

Companies wishing to sponsor and/or exhibit at any of these events should contact the conference co-ordinator as soon as possible

For further information contact:

Conferencing, SAIMM
P O Box 61127, Marshalltown 2107
Tel: (011) 834-1273/7
Fax: (011) 833-8156 or (011) 838-5923
E-mail: raymond@saimm.co.za

Website: <http://www.saimm.co.za>

SAIMM DIARY

2014

- ◆ **SCHOOL**
Grade control and reconciliation
23–24 April 2014, Moba Hotel, Kitwe, Zambia
- ◆ **SYMPOSIUM**
**6th South African Rock Engineering Symposium
SARES 2014—Creating value through innovative rock engineering**
12–14 May 2014, Misty Hills Country Hotel and Conference Centre, Cradle of Humankind
- ◆ **SCHOOL**
Drilling and Blasting
19–20 May 2014, Swakopmund Hotel & Entertainment Centre, Swakopmund, Namibia
- ◆ **CONFERENCE**
Furnace Tapping Conference 2014
27–28 May 2014, Conference
29 May 2014, Technical Visit
Misty Hills Country Hotel and Conference Centre, Cradle of Humankind
- ◆ **SEMINAR**
**Society of Mining Professors—
A Southern African Silver Anniversary**
26–30 June 2014, The Maslow Hotel, Sandton, Gauteng
- ◆ **SCHOOL**
Mine Planning School
15–16 July 2014, Mine Design Lab, Chamber of Mines Building, The University of the Witwatersrand
- ◆ **CONFERENCE**
Pyrometallurgical Modelling Principles and Practices
5–6 August 2014, Misty Hills Country Hotel and Conference Centre, Cradle of Humankind
- ◆ **CONFERENCE**
**MineSafe Conference 2014
Technical Conference and Industry day**
20–21 August 2014, Conference
22 August 2014, Industry day
Emperors Palace, Hotel Casino Convention Resort, Johannesburg
- ◆ **SCHOOL**
3rd Mineral Project Valuation School
9–11 September 2014, Mine Design Lab, Chamber of Mines Building, The University of the Witwatersrand
- ◆ **CONFERENCE**
Surface Mining 2014
16–17 September 2014, The Black Eagle Room, Nasrec Expo Centre

INTERNATIONAL ACTIVITIES

2014

23–24 April 2014 — Grade control and reconciliation

Moba Hotel, Kitwe, Zambia
Contact: Raymond van der Berg
Tel: +27 11 834-1273/7
Fax: +27 11 838-5923/833-8156
E-mail: raymond@saimm.co.za
Website: <http://www.saimm.co.za>

12–14 May 2014 — 6th South African Rock Engineering Symposium SARES 2014

Creating value through innovative rock engineering

Misty Hills Country Hotel and Conference Centre,
Cradle of Humankind
Contact: Raymond van der Berg
Tel: +27 11 834-1273/7
Fax: +27 11 838-5923/833-8156
E-mail: raymond@saimm.co.za
Website: <http://www.saimm.co.za>

19–20 May 2014 — Drilling and Blasting

Swakopmund Hotel & Entertainment Centre,
Swakopmund, Namibia
Contact: Raymond van der Berg
Tel: +27 11 834-1273/7
Fax: +27 11 838-5923/833-8156,
E-mail: raymond@saimm.co.za
Website: <http://www.saimm.co.za>

19–23 May 2014 — Fundamentals of Process Safety Management (PSM)

Johannesburg, South Africa
Contact: RDC Prior,
Tel: +27 (0) 825540010
E-mail: r.prior@mweb.co.za

24–31 May 2014 — ALTA 2014 Nickel-Cobalt-Copper, Uranium-REE and Gold-Precious Metals Conference & Exhibition

Perth, Western Australia
Contact: Allison Taylor
E-Mail: allisontaylor@altamet.com.au
Tel: +61 (0)411 692-442
Website: <http://www.altamet.com.au/conferences/alta-2013/>

27–29 May 2014 — Furnace Tapping Conference 2014

Misty Hills Country Hotel and Conference Centre,
Cradle of Humankind
Contact: Cameron Nagel
Tel: +27 11 834-1273/7
Fax: +27 11 838-5923/833-8156
E-mail: cameron@saimm.co.za
Website: <http://www.saimm.co.za>

11–12, June, 2014 — AIMS 2014: 6th International Symposium 'High Performance Mining'

Aachen, Germany
Tel: +49-(0)241-80 95673
Fax: +49-(0)241-80 92272
E-Mail: aims@bbk1.rwth-aachen.de
Website: <http://www.aims.rwth-aachen.de>

26–30 June 2014 — Society of Mining Professors A Southern African Silver Anniversary

The Maslow Hotel, Sandton, Gauteng, South Africa
Contact: Raymond van der Berg
Tel: +27 11 834-1273/7
Fax: +27 11 838-5923/833-8156
E-mail: raymond@saimm.co.za
Website: <http://www.saimm.co.za>

15–16 July 2014 — Mine Planning School

Mine Design Lab, Chamber of Mines Building,
The University of the Witwatersrand
Contact: Cameron Nagel
Tel: +27 11 834-1273/7
Fax: +27 11 838-5923/833-8156
E-mail: cameron@saimm.co.za
Website: <http://www.saimm.co.za>

5–6 August 2014 — Pyrometallurgical Modelling Principles and Practices

Misty Hills Country Hotel and Conference Centre,
Cradle of Humankind
Contact: Raymond van der Berg,
Tel: +27 11 834-1273/7
Fax: +27 11 838-5923/833-8156
E-mail: raymond@saimm.co.za
Website: <http://www.saimm.co.za>

INTERNATIONAL ACTIVITIES

2014 (continued)

20–22 August 2014 — MineSafe Conference 2014

Technical Conference and Industry day

20–21 August 2014: Conference

22 August 2014: Industry day

Emperors Palace, Hotel Casino Convention Resort,
Johannesburg

Contact: Raymond van der Berg

Tel: +27 11 834-1273/7

Fax: +27 11 838-5923/833-8156

E-mail: raymond@saimm.co.za

Website: <http://www.saimm.co.za>

9–11 September 2014 — 3rd Mineral Project Valuation School

Mine Design Lab, Chamber of Mines Building,
The University of the Witwatersrand

Contact: Camielah Jardine,

Tel: +27 11 834-1273/7

Fax: +27 11 838-5923/833-8156

E-mail: camielah@saimm.co.za,

Website: <http://www.saimm.co.za>

16–17 September 2014 — Surface Mining 2014

The Black Eagle Room, Nasrec Expo Centre

Contact: Cameron Nagel,

Tel: +27 11 834-1273/7

Fax: +27 11 838-5923/833-8156,

E-mail: cameron@saimm.co.za,

Website: <http://www.saimm.co.za>

20–24 October 2014 — 6th International Platinum Conference

Sun City, South Africa

Contact: Cameron Nagel,

Tel: +27 11 834-1273/7

Fax: +27 11 838-5923/833-8156,

E-mail: cameron@saimm.co.za,

Website: <http://www.saimm.co.za>

12 November 2014 — 12th Annual Southern African Student Colloquium

Mintek, Randburg

Contact: Cameron Nagel,

Tel: +27 11 834-1273/7

Fax: +27 11 838-5923/833-8156,

E-mail: cameron@saimm.co.za,

Website: <http://www.saimm.co.za>

27–28 November 2014 — Accessing Africa's Mineral Wealth: Mining Transport Logistics

Johannesburg

Contact: Raymond van der Berg,

Tel: +27 11 834-1273/7

Fax: +27 11 838-5923/833-8156,

E-mail: raymond@saimm.co.za,

Website: <http://www.saimm.co.za>

2015

March 2015 — PACRIM 2015

Hong Kong, China

Tel: +27 11 834-1273/7

Fax: +27 11 838-5923/833-8156,

E-mail: CBenn@ausimm.com.au

Website: <http://www.pacrim2015.ausimm.com.au>

5–9 October 2015 — MPES 2015

Johannesburg, South Africa

Contact: Raj Singhai

E-mail: singhal@shaw.ca or

Raymond van der Berg,

Tel: +27 11 834-1273/7

Fax: +27 11 838-5923/833-8156,

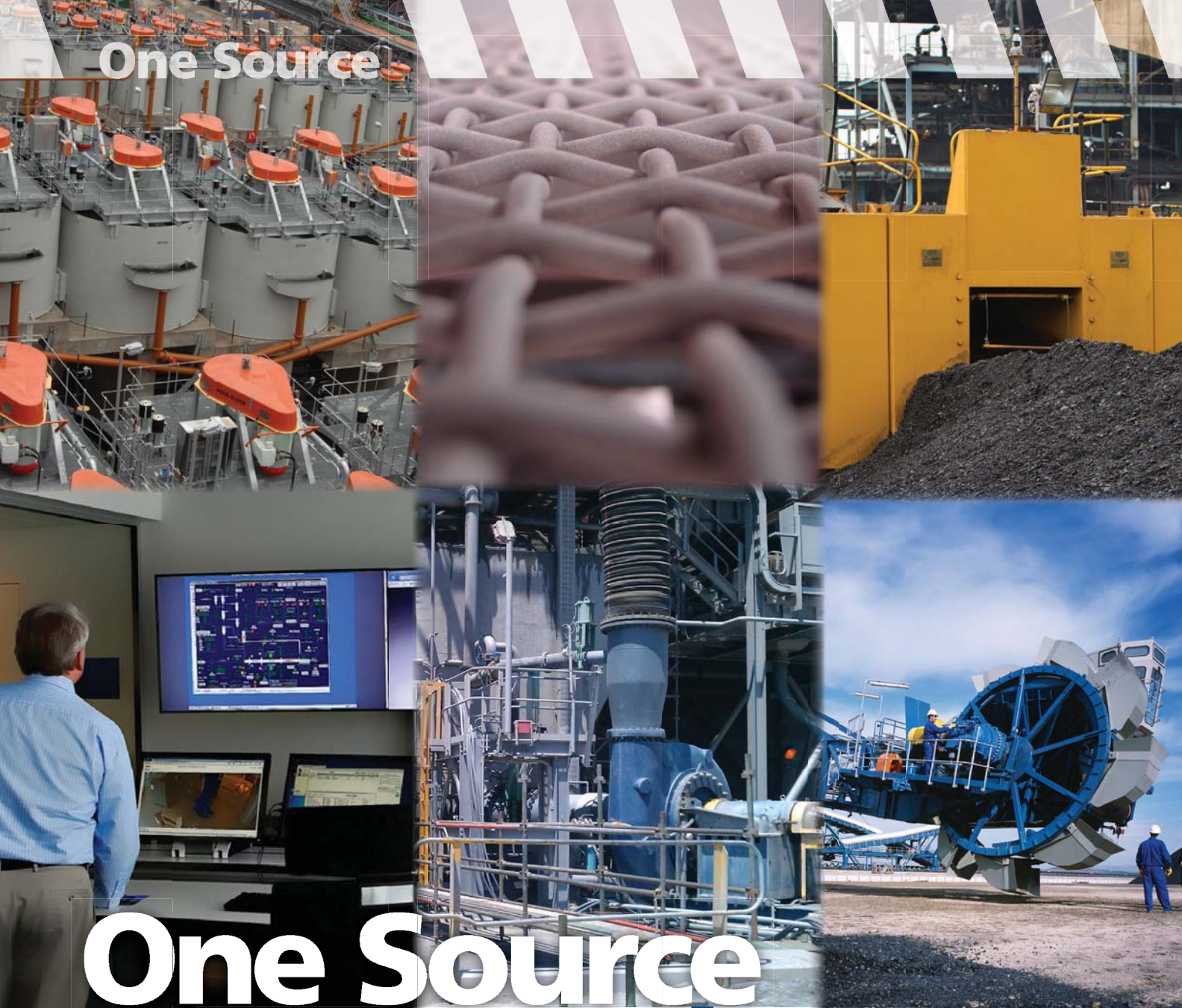
E-mail: raymond@saimm.co.za

Website: <http://www.saimm.co.za>

Company Affiliates

The following organizations have been admitted to the Institute as Company Affiliates

AECOM SA (Pty) Ltd	Duraset	Namakwa Sands (Pty) Ltd
AEL Mining Services Limited	Elbroc Mining Products (Pty) Ltd	New Concept Mining (Pty) Limited
Air Liquide (PTY) Ltd	Engineering and Project Company Ltd	Northam Platinum Ltd - Zondereinde
Air Products SA (Pty) Ltd	eThekweni Municipality	Osborn Engineered Products SA (Pty) Ltd
AMEC Mining & Metals	Evrax Highveld Steel and Vanadium Corp Ltd	Outotec (RSA) (Proprietary) Limited
AMIRA International Africa (Pty) Ltd	Exxaro Coal (Pty) Ltd	PANalytical (Pty) Ltd
ANDRITZ Delkor(Pty) Ltd	Exxaro Resources Limited	Paterson and Cooke Consulting Engineers (Pty) Ltd
Anglo Operations (Pty) Ltd	FLSmith Minerals (Pty) Ltd	Paul Wurth International SA
Anglogold Ashanti Ltd	Fluor Daniel SA (Pty) Ltd	Polysius A Division Of Thyssenkrupp Engineering (Pty) Ltd
Arcus Gibb (Pty) Ltd	Franki Africa (Pty) Ltd Johannesburg	Precious Metals Refiners
Atlas Copco Holdings South Africa (Pty) Limited	Fraser Alexander Group	Rand Refinery Limited
Aurecon South Africa (Pty) Ltd	GFI Mining SA (Pty) Ltd	Redpath Mining (South Africa) (Pty) Ltd
Aveng Mining Shafts and Underground	Goba (Pty) Ltd	Rosond (Pty) Ltd
Aveng Moolmans (Pty) Ltd	Hall Core Drilling (Pty) Ltd	Royal Bafokeng Platinum
Bafokeng Rasimone Platinum Mine	Hatch (Pty) Ltd	Roymec Tecvhnologies (Pty) Ltd
Barloworld Equipment -Mining	HPE Hydro Power Equipment (Pty) Ltd	RSV Misym Engineering Services (Pty) Ltd
BASF Holdings SA (Pty) Ltd	Impala Platinum Limited	Rustenburg Platinum Mines Limited
Bateman Minerals and Metals (Pty) Ltd	IMS Engineering (Pty) Ltd	SAIEG
BCL Limited	Joy Global Inc. (Africa)	Salene Mining (Pty) Ltd
BedRock Mining Support (Pty) Ltd	Leco Africa (Pty) Limited	Sandvik Mining and Construction Delmas (Pty) Ltd
Bell Equipment Company (Pty) Ltd	Longyear South Africa (Pty) Ltd	Sandvik Mining and Construction RSA(Pty) Ltd
Bell, Dewar and Hall Incorporated	Lonmin Plc	SANIRE
BHP Billiton Energy Coal SA Ltd	Ludowici Africa	Sasol Mining(Pty) Ltd
Blue Cube Systems (Pty) Ltd	Lull Storm Trading (Pty)Ltd T/A Wekaba Engineering	SENET
Bluhm Burton Engineering (Pty) Ltd	Magnetech (Pty) Ltd	Senmin International (Pty) Ltd
Blyvooruitzicht Gold Mining Co Ltd	Magotteaux(Pty) LTD	Shaft Sinkers (Pty) Limited
BSC Resources	MBE Minerals SA Pty Ltd	Smec SA
CAE Mining (Pty) Limited	MCC Contracts (Pty) Ltd	SMS Siemag South Africa (Pty) Ltd
Caledonia Mining Corporation	MDM Technical Africa (Pty) Ltd	SNC Lavalin (Pty) Ltd
CDM Group	Metalock Industrial Services Africa (Pty)Ltd	Sound Mining Solutions (Pty) Ltd
CGG Services SA	Metorex Limited	SRK Consulting SA (Pty) Ltd
Chamber of Mines	Metso Minerals (South Africa) (Pty) Ltd	Time Mining and Processing (Pty) Ltd
Concor Mining	Minerals Operations Executive (Pty) Ltd	Tomra Sorting Solutions Mining (Pty) Ltd
Concor Technicrete	MineRP	TWP Projects (Pty) Ltd
Council for Geoscience	Mintek	Ukwazi Mining Solutions (Pty) Ltd
CSIR-Natural Resources and the Environment	Modular Mining Systems Africa (Pty) Ltd	Umgeni Water
Department of Water Affairs and Forestry	MRM Mining Services	VBKOM Consulting Engineers
Deutsche Securities Pty Ltd	MSA Group (Pty) Ltd	Webber Wentzel
Digby Wells and Associates	Multotec (Pty) Ltd	Xstrata Coal South Africa (Pty) Ltd
Downer EDI Mining	Murray and Roberts Cementation	
DRA Mineral Projects (Pty) Ltd	Nalco Africa (Pty) Ltd	



One Source

One Source Many Solutions

FLSmidth is your One Source for crushing, grinding, classifying, thickening, clarifying, slurry handling, flotation, mine shaft systems, pyroprocessing, material handling, automation, screens, centrifuges and complementary products, engineering, metallurgical testing and modernisation services. FLSmidth offers you a complete line of equipment and services with proven reliability and enhancing performance from the leading brand names of ABON, Buffalo, CEntry, Conveyor Engineering, Dawson Metallurgical Laboratories, Decanter Machine, Dorr-Oliver, EIMCO, ESSA, FFE, Fuller-Traylor, KOCH, Knelson, Krebs, Ludowici, Maag Gear, Mayer, Meshcape, MIE, Möller, MVT, PERI, Phillips Kiln Services, Pneumapress, RAHCO, Raptor, Roymec, Shriver, Summit Valley, Technequip and WEMCO.

Enjoy increased recoveries while saving time and money on your next project! Let us help you tackle your specific requirements.

For more information contact us
Tel no. +27 (0)10 210 4000 • fsm-za@flsmidth.com • www.flsmidth.com

Visit us at
Mining Indaba
2014
Hall 2
Stand no.
302

FLSMIDTH



LONMIN

Shared Value

SHARED FUTURE



Platinum in
catalysis,
a key ingredient for **clean air.**



www.lonmin.com